THESIS FOR THE DEGREE OF DOCTOR OF PHILOSOPHY

Catalyst Design for the Valorisation of 2,5-Dimethylfuran into Aromatics

Guido J.L. de Reijer

Department of Chemistry and Chemical Engineering
CHALMERS UNIVERSITY OF TECHNOLOGY
Gothenburg, Sweden 2025

Catalyst Design for the Valorisation of 2,5-Dimethylfuran into Aromatics

Guido J.L. de Reijer

ISBN 978-91-8103-286-4

Acknowledgements, dedications, and similar personal statements in this thesis, reflect the author's own views.

Doktorsavhandlingar vid Chalmers tekniska högskola

Ny serie Nr. 5744

ISSN 0346-718X

Department of Chemistry and Chemical Engineering
Chalmers University of Technology
SE-412 96 Göteborg
Telephone +46 31 772 1000

Cover:
Artistic interpretation of the conversion of biomass-derived 2,5-dimethylfuran into aromatics, employing gallium-based catalysts. Thank you Karlijn for your help with the design.

Printed by Chalmers Digitaltryck
Göteborg, Sweden 2025

Catalyst Design for the Valorisation of 2,5-Dimethylfuran into Aromatics
Guido J.L. de Reijer
Department of Chemistry and Chemical Engineering
Chalmers University of Technology

Abstract

In 2025, the urgency for global action against climate change is greater than ever. The transition of the chemical industry from fossil- to biomass-based feedstocks plays a central role. In this work, the catalytic conversion of biomass-derived 2,5-dimethylfuran into aromatics, essential chemical building blocks, is investigated.

The relationship between the properties of the catalyst—i.e., its framework, acidity, and porosity—and its catalytic performance—i.e., its activity, selectivity, and stability—was evaluated in a flow reactor for a series of zeolites, zeotypes, and metal oxides. Medium- and large-pore frameworks such as MFI, BEA, and FAU, display the highest activity and selectivity due to favourable steric effects. Isomorphous substitution with gallium (Ga) instead of aluminium (Al) increases the production of aromatics and the lifetime of the catalyst, ascribed to a higher fraction of strong Brønsted and Lewis acid sites. Increasing the Al or Ga content leads to a higher acid site density and improved catalytic performance, until a framework- and element-specific threshold is reached, beyond which excessive coking causes catalyst deactivation. Introducing a secondary pore network of meso- and macropores enhances the transport of reagents and products, increasing both the accessibility and activity of each acid site.

This thesis identifies key design principles and proposes that the optimal catalyst combines a microporous framework to steer selectivity towards BTX, a high but controlled metal content and acid site density to maximise activity, and a hierarchical porosity to improve mass transport.

Keywords: 2,5-dimethylfuran, aluminium, aromatics, biomass conversion, BTX, catalysis, gallium, micropores, mesopores, zeolites, zeotypes

Aan opa

List of Publications

This thesis is based on the following appended publications:

I. Isomorphous Substitution of Gallium into MFI-Framework Zeolite Increases 2,5-Dimethylfuran to Aromatics Selectivity and Suppresses Catalyst Deactivation

Christopher Sauer, Guido J.L. de Reijer , Andreas Schaefer, Per-Anders Carlsson

Topics in Catalysis, 66 **(2023)**, 1329-1340, *doi:10.1007/s11244-022-01776-2*

II. Catalytic Conversion of Furans to Aromatics over Ga-MFI Zeotypes with Varying Gallium Content

Guido J.L. de Reijer , Andreas Schaefer, Anders Hellman, Per-Anders Carlsson

Industrial & Engineering Chemistry Research, 64 **(2025)**, 2025-2035, *doi:10.1021/acs.iecr.4c03465*

III. Elucidating the Effect of Mesopores on the Catalytic Conversion of Furans to Aromatics over Hierarchical Ga-MFI, Ga-MFI/MCM-41 Composites, and Ga-SPP

Guido J.L. de Reijer , Andreas Schaefer, Anders Hellman, Per-Anders Carlsson

In manuscript

IV. Continuous isomerisation of 2,5-dimethylfuran to 2,4-dimethylfuran over Ga-silicate

Christopher Sauer, Guido J.L. de Reijer , Barbara Wilfinger, Anders Hellman, Per-Anders Carlsson

Chemistry - A European Journal, 30, **(2024)**, *doi:10.1002/chem.202303810*

My Contributions to the Publications

Paper I

I was partially responsible for the conceptualisation, I planned and carried out the synthesis and experimental work with Christopher Sauer, I interpreted the results together with my co-authors, I wrote sections of the experimental, results and discussion, and conclusion. Shared first-authorship.

Paper II

I was responsible for conceptualisation, planned and carried out all experimental work and interpreted the results together with my co-authors. I wrote the first draft and was responsible for review and submission.

Paper III

I was responsible for conceptualisation, planned and carried out all experimental work and interpreted the results together with my co-authors. I wrote the first draft and was responsible for review and submission.

Paper IV

I planned and carried out the experimental work and interpreted the results together with my co-authors. Responsible for review and submission.

Conference contributions

Catalytic Conversion of Furans to Aromatics over Modified Zeolites
Guido J.L. de Reijer, and Per-Anders Carlsson
Poster presentation at the 19^{th} *Nordic Symposium on Catalysis (NSC19)*
06-08 June 2022, Espoo, Finland

Modified Zeolites for the Catalytic Valorisation of Furans to Aromatics
Guido J.L. de Reijer and Per-Anders Carlsson
Poster presentation at the 9^{th} *Tokyo Conference on Advanced Catalytic Science and Technology (TOCAT9) - won poster award*
24-29 July 2022, Hybrid/Tokyo, Japan

Valorisation of Biomass: Furans to Aromatics over modified zeolites
Guido J.L. de Reijer and Per-Anders Carlsson
Oral presentation at the Catalysis workshop - New Materials theme
02-03 May 2023, Lund, Sweden

Catalytic Valorisation of Furans to Aromatics over Modified Zeolites
Guido J.L. de Reijer, Andreas Schaefer, Anders Hellman, and Per-Anders Carlsson
Poster presentation at the 15^{th} *European Congress on Catalysis (EuropaCat2023)*
27 August - 1 September 2023, Prague, Czech Republic

Modified Zeolites for Catalytic Valorisation of Furans to Aromatics
Guido J.L. de Reijer, Andreas Schaefer, and Per-Anders Carlsson
Poster presentation at the 20^{th} *Nordic Symposium on Catalysis (NSC20)*
03-05 June 2024, Stavanger, Norway

Catalytic Valorisation of Furans to Aromatics over Modified Zeolites
Guido J.L. de Reijer, Andreas Schaefer, Anders Hellman, and Per-Anders Carlsson
Poster presentation at the 32^{nd} *European Biomass Conference and Exhibition (EUBCE2024*
24-27 June 2024, Marseille, France

Contents

List of Figures

List of Tables

List of Abbreviations

2,4-dmf	2,4-dimethylfuran
2-mcpo	2-methyl-2-cyclopentenone
2-mf	2-methylfuran
3-mcpo	3-methyl-2-cyclopentenone
BAS	Brønsted acid site(s)
BET	Brunauer-Emmett-Teller
BJH	Barrett-Joyner-Halenda
BTX	Benzene, toluene, and xylenes
CMR	Carcinogenic, mutagenic, and reptrotoxic
dmf	2,5-dimethylfuran
DRIFTS	Diffuse reflectance infrared Fourier transform spectroscopy
DSC	Differential scanning calorimetry
EDX	Energy-dispersive X-ray spectroscopy
FCC	Fluid catalytic cracking
FTIR	Fourier-Transform infrared spectroscopy
GC	Gas chromatography
HAADF-STEM	High-angle annular dark-field scanning transmission electron microscopy
hmf	Hydroxymethylfurfural
IMR-MS	Ion-molecule-reaction mass spectrometry
IR	Infrared
LAS	Lewis acid site(s)
MS	Mass spectrometry
NLDFT	Non-local density functional theory
PAH	Polycyclic aromatic hydrocarbons
PET	Polyethylene terephthalate
PS	Polystyrene
SAXS	Small-angle X-ray scattering
scXRD	Single-crystal X-ray diffraction
SEM	Scanning electron microscopy
SNR	Signal-to-noise ratio
SA	Surface area
ssNMR	Solid-state nuclear magnetic resonance
TEM	Transmission electron microscopy
TEOS	Tetraethyl orthosilicate
TGA	Thermogravimetric analysis
TOS	Time-on-stream
TPA	Tetrapropylammonium
XRD	X-Ray diffraction
XRF	X-Ray fluorescence

1 Introduction

In the year 2025, amidst an uncertain geopolitical landscape with ongoing wars, trade disputes, and rising tensions, one thing is certain: universal action is required to tackle climate change now more than ever. As the global population is expected to grow from 8.2 to over 10 billion people within the next 50 years, mankind's demand for energy, materials, and food will increase accordingly. The current and future human consumption of natural resources puts an excessive stress on the Earth's ecosystem. The use of fossil fuels for energy and materials, which have long powered human development, is a major driver of climate change, pollution, and environmental degradation. Their extraction and combustion releases harmful pollutants such as particulate matter and greenhouse gases, including sulphur-, nitrogen-, and carbon-based oxides [1–3]. Global warming results in a higher frequency of extreme weather events, including floods, droughts, and wildfires, leading to the mass extinction of flora and fauna [4–6].

Despite indisputable evidence of these detrimental consequences, the world is still deeply reliant on the use of fossil fuels, as they have been supplying roughly 80% of the world's energy during the past years (figure 1.1) [7]. Rapid action is required and people need to take responsibility, both on a personal and global scale. For example, one can reduce one's own footprint by consuming less and adopting a plant-based diet, while economic, political, and technological interests should focus on recycling resources and developing renewable energy sources, including solar, wind, marine, hydro, geothermal, biomass, and waste [8–10]. Additionally, major improvements can be made in the chemical industry, responsible for 13% of the total fossil fuel consumption, by utilizing alternative feedstocks [7].

In contrast to the heating and transport sector, electrification of the production of chemicals is difficult. Fossil carbon molecules are used both for energy and as the physical feedstock for many high-volume commodity chemicals, such as the aromatic compounds benzene, toluene, and xylenes (BTX, figure 1.2). BTX are three of the seven basic commodity petrochemicals that serve as building blocks for 90 % of all downstream organics, used in virtually all of our everyday items such as plastics, clothing, electronics, paints, and pharmaceuticals [11–13]. This carbon lock-in phenomenon is cemented by additional investments in the petrochemical industry, as part of a diversification strategy, culminating in both an institutional and behavioural lock-in [14–20]. Due to the difficulty to defossilise this sector, it often escapes scrutiny

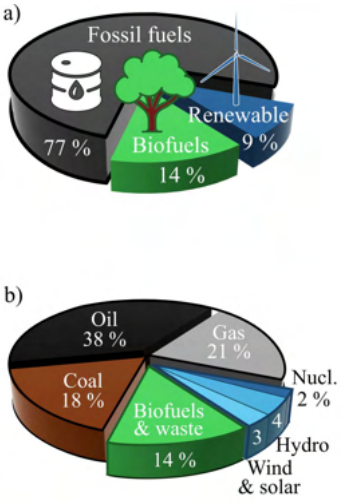

Figure 1.1: Gross world energy consumption (2020) per fuel including fossil fuels (coal, oil, and gas), biofuels and waste, and renewable sources (nuclear, hydro, wind, and solar) [7].

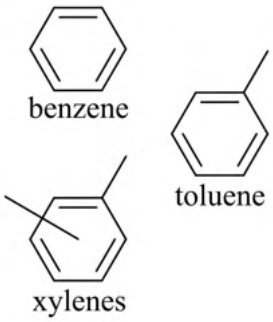

Figure 1.2: Aromatic commodity chemicals benzene, toluene, and xylenes (BTX).

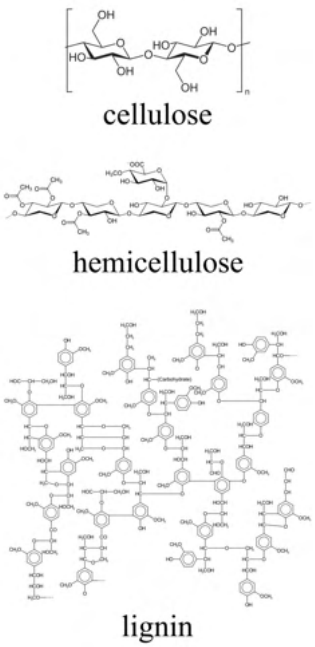

Figure 1.3: Complex molecules present in biomass including cellulose, hemicellulose, and lignin.

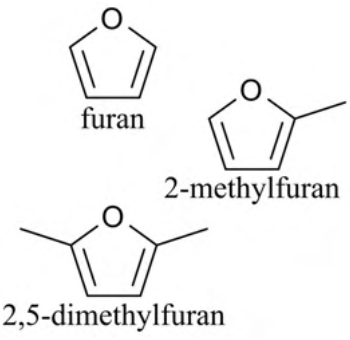

Figure 1.4: Furan-based model compounds including furan, 2-methylfuran (mf), and 2,5-dimethylfuran (dmf).

and remains unaddressed, even at the highest climate conventions (COP28, 2023) [21].

We are presented with both a challenge and an opportunity. What if the production of commodity chemicals is decoupled from fossil fuels and they can be synthesized from renewable feedstocks instead, such as biomass? Exactly this question is addressed in this thesis.

Biomass consists of all biological matter on earth, like plants, trees, and waste. During their lifetime, they have captured CO_2 from the air and stored it as part of complex molecules, such as cellulose, hemicellulose, and lignin (figure 1.3). These can be broken down into smaller molecules or their inherent chemical functionalities may be utilized by converting them into larger, valuable chemicals like BTX. This reaction requires high temperatures and energy costs, resulting in the formation of many undesired side-products. To accelerate the reaction, lower the needed temperature and costs, and tune the selectivity towards BTX, a catalyst is necessary.

A catalyst is an external material or chemical that enhances the reaction rate and selectivity by lowering the activation energy through enabling a different reaction pathway. To effectively investigate the role of the catalyst, pure model compounds may be used as reactants instead of raw biomass. This circumvents the issues related to the heterogeneous and complex composition of biomass, allowing one to connect the observed conversion and selectivity to the properties of the catalyst.

One class of model compounds that can be derived from biomass, comprises furans: aromatic five-membered rings containing an oxygen molecule (figure 1.4). To summarise, this thesis investigates the effect of the catalyst's characteristics on the conversion of 2,5-dimethylfuran (dmf) into aromatics. It aims to increase our understanding of the catalysts, to identify the catalyst design principles to aid future catalyst design, and to ultimately contribute to the transition towards a circular, fossil-free chemical industry.

1.1 How to navigate this thesis

- **Structure of the thesis**
  This thesis is divided into chapters and subchapters, as indicated at the top of each page, start of each chapter, and in the table of contents (page *xi* and *xii*). After the main text (Kappa), four detailed publications and their supporting informations are presented for more in-depth information.
- **Side column and sidenotes**
  Besides the main text column, smaller tables, figures, and annotations can be found in the side column, numbered in the text as a sidenote.[1] Citations are numbered like [1], and a complete bibliography is provided on pages 81–88.
- **Lists of publications, figures, tables, and abbreviations**
  An overview of the list of publications, figures, tables, and abbrevations, can be found in the preface, pages *vii* and *xiii*–*xvii*.
- **Overview materials**
  An overview of all catalysts can be found in the methodology section (section 3.1, tables 3.1 and 3.2).
- **Take-home messages**
  The most important findings of each results section are summarised in take-home messages, denoted by the blue boxes.

1: Example of a sidenote

Take-home message
This is an example of a take-home message: This thesis will guide you through my journey to find a suitable catalyst for the conversion of 2,5-dimethylfuran into aromatics. Enjoy!

Background 2

This section elaborates on the current state-of-the-art of biomass-to-BTX production, the basic concepts of catalysis, the porous metal oxides used as catalysts, including zeolites and mesoporous silica. Finally, the research objective and aiding questions of this thesis are stated.

2.1 Biomass-to-BTX

As mentioned briefly before, BTX is used as building blocks to manufacture numerous chemicals and materials, including fuels, solvents, resins, paints, dyes, clothing, electronics, pharmaceuticals, and plastics. For example, benzene is used to synthesize aspirin (acetylsalicylic acid) and plastics such as polystyrene (PS, figure 2.1), toluene is used in paints and to produce trinitrotoluene (TNT), and *para*-xylene is used to produce plastics like polyethylene terephthalate (PET, figure 2.2).[1]

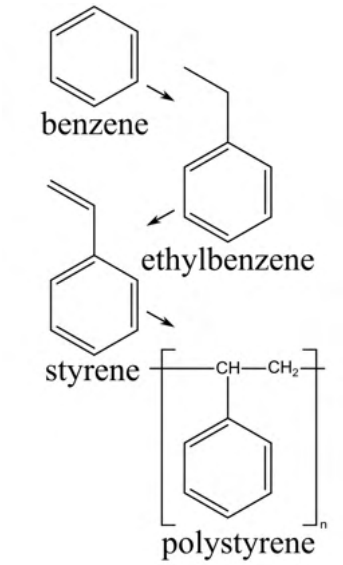

Figure 2.1: Step-wise conversion of benzene to polystyrene.

Currently, over 95 % of BTX is produced through steam cracking and catalytic reforming of naphtha, a liquid hydrocarbon mixture derived from crude oil [22–24]. This process is often catalysed by zeolites, which are microporous solid acids described further in section 2.3. Similarly, the conversion of biomass can be catalysed by zeolites, and numerous studies have been performed focusing on raw biomass [25–27], on biomass and petrochemical blends [28–30], or on model compounds: so-called biomass-derived platform chemicals including sugars, polyols, acids, and furanics [28, 30–35].

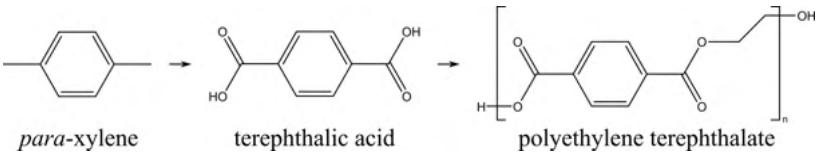

Figure 2.2: Step-wise conversion of *para*-xylene to polyethylene terephthalate.

To elaborate, lignocellulosic biomass comprises three main components: the biopolymers cellulose, hemicellulose, and lignin, each present at levels of 35 to 55 %, 20 to 55 %, and 10 to 30 %, respectively, dependent on the type of biomass [36]. They can be valorised[2] biologically through fermentation processes [37, 38], thermally through gasification [39, 40],[3] and catalytically through pyrolysis [12, 40–45].[4]

Producing the platform model compounds is not easy, since the components should first be separated and pretreated. When

1: The two methyl groups in xylene can be bonded to different carbon atoms of the ring, resulting in *meta*-, *ortho*-, and *para*-xylene.

2: increased in value

3: gasification is high-temperature conversion under controlled atmosphere, such as oxygen or steam, producing syngas

4: catalytic fast pyrolysis (CFP) is the decomposition with a catalyst in the absence of air, often still at elevated temperatures.

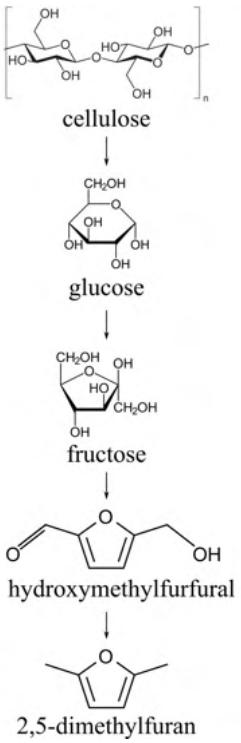

Figure 2.3: Stepwise conversion of cellulose into 2,5-dimethylfuran.

cellulose or hemicellulose is pretreated with acid, they rapidly hydrolyse to glucose and xylose, respectively. Glucose can further isomerise to fructose, which can be converted by an acidic catalyst into a platform molecule named hydroxymethylfurfural (hmf). Finally, hmf can be converted into 2,5-dimethylfuran and other furan derivatives (figure 2.3).

Other biomass-derived furans, like furan and 2-methylfuran (2-mf), have also been studied for their conversion into aromatics [27, 42, 46]. However, as dmf has been shown to produce *para*-xylene, one of the more valuable aromatics, this furan was used as reactant. Additionally, dmf is the safest furanic to handle as 2-mf is fatal when inhaled and furan is classified as carcinogenic, mutagenic, or reprotoxic (CMR).

In a broader context, the chemical refinery of the future would primarily be based on biomass, plastic waste, and CO_2 captured from the air [47], requiring significant investments of 1 to 3.3 trillion USD by 2050 [48]. Yet, initial studies are promising and biomass holds much unlocked potential, especially in the Nordic countries, with 17 % of all European forest area being located in Sweden and 13 % in Finland. Not only as a feedstock for chemicals but also as a fertilizer or fuel, provided that the process occurs sustainably [49, 50].[5] The benefit of using biomass as a feedstock for chemicals is that the carbon atoms are captured and reused instead of emitted as pollutants.

5: conditions for sustainable use of biomass:

- New biomass must be replenished at an equal or higher rate than consumed.
- Biodiversity must be maintained.
- Biomass may not compete with food supply.

2.2 Catalysis

As mentioned in the introduction, a catalyst is a tertiary material or molecule that increases the reaction rate. It takes part in the reaction and may even undergo structural changes, although it may not undergo a net chemical change and must be regenerated to its initial state at the end of the reaction [51]. To elaborate, the overall change in Gibbs free energy (ΔG) of the reaction remains unchanged (figure 2.4) [52]. In an uncatalysed reaction, reactants must overcome a substantial energy barrier before being transformed into products, while a different pathway with a lower activation energy (E_a) is enabled when adding a catalyst.

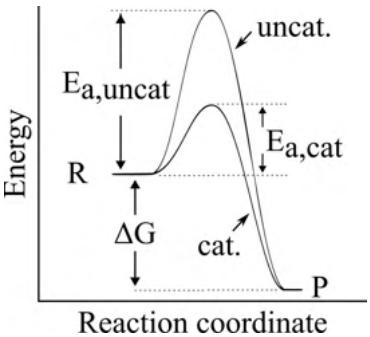

Figure 2.4: Schematic potential energy diagram of an uncatalysed and catalysed reaction.

There are two main types of catalysis: homo- and heterogeneous catalysis [52]. Homogeneous catalysis refers to a system in which the catalyst and the reactants are in the same phase, while in heterogeneous catalysis, they are in different faces and the reaction takes place at or near the interface between them [52–54]. Generally, this interface is between a solid catalyst and liquid or gaseous reactants. As opposed to homogeneous catalysts, not every molecule or catalytic entity can act as an active site, making heterogeneous

catalysts intrinsically less active and selective [55]. Instead, the active sites are distributed on a porous support, which plays an important role in both stabilising the active catalytic phase and offering a high surface area to increase activity. Additionally, the microporous framework affects product selectivity, allowing the production and diffusion of certain molecules while hindering others. Careful design of the porous structure is important to drive selectivity, enhance catalytic activity, and preserve sufficient mass transport [56].

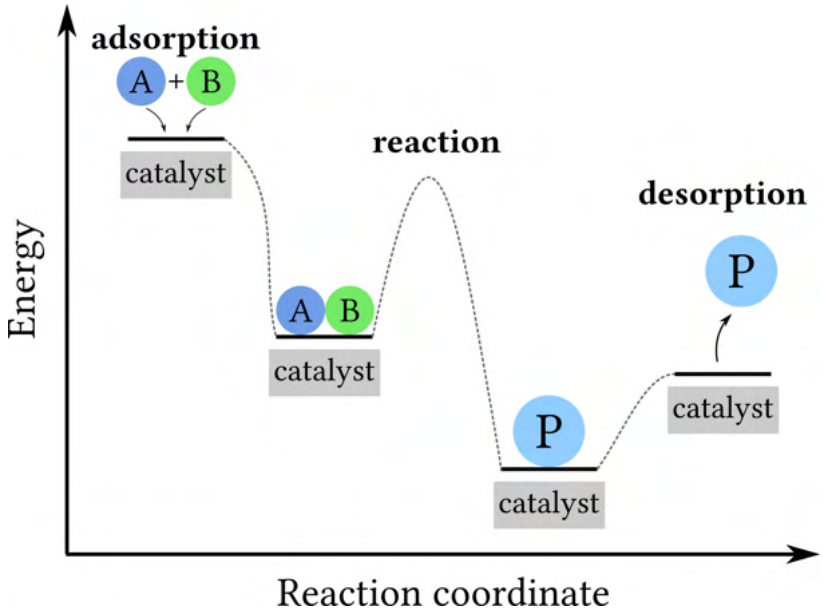

Figure 2.5: Simple schematic conversion of molecule A and B to product P over a heterogeneous catalyst via elementary steps.

Heterogeneous catalysis can be simplified into several elementary steps (figure 2.5): First, reactants *A* and *B* diffuse to the surface of the catalyst, followed by adsorption, after which they react and are converted into product *P*. Product *P* subsequently desorbs and diffuses away. In reality, reactions may occur via multiple competing pathways, potentially through several transition states, resulting in complex mechanisms and product mixtures.

Solid catalysts used in heterogeneous catalysis are typically robust, thermally stable, and possess tuneable properties [57]. Separation between the catalyst and the products is straightforward and the catalyst can often be regenerated and reused. In general, around 80 % of all catalysts used in industry are heterogeneous catalysts, while around 90 % of all chemical manufacturing processes involve the use of catalysts [58, 59].

2.3 Zeolites

Among all different catalytic materials, zeolites stand out as one of the most pivotal and widely studied class of catalysts. These microporous,[6] crystalline, solid acids are primarily used in the petrochemical industry, e.g., in the fluid catalytic cracking (FCC) of crude oil, the conversion of methanol-to-hydrocarbons, and the conversion of methane-to-methanol, as well as in the conversion of biomass into aromatics [41, 62–64]. Zeolites consist of silicon (Si), aluminium (Al), and oxygen (O), forming tetrahedra ($TO_{4/2}$ with T=Si or Al) in which each Si or Al binds to four oxygen atoms that are in turn each shared with another Si or Al (figure 2.6). These tetrahedra combine into secondary building units (SBU) comprising different rings and shapes, which combine further into complex, three-dimensional frameworks. Over 260 unique framework structures have been discovered or developed, denoted by 3-letter codes such as MFI, FAU, and MOR [65].

6: micropores are < 2 nm, mesopores are between 2 and 50 nm, and macropores are > 50 nm [60, 61]

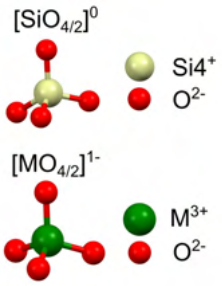

Figure 2.6: Zeolite tetrahedra with neutral $[SiO_2]$ and negatively charged $[MO_2]^{-1}$, with M=trivalent metal such as Al^{3+} and Ga^{3+}

Other classes of microporous catalysts that have been considered as potential catalysts are covalent organic frameworks (COF), metal-organic framework (MOF), and the latter's subclass zeolitic imidazolate frameworks (ZIF). However, these materials generally possess a lower thermal stability and would degrade or decompose under the required operating conditions, as was observed experimentally for Basolite C300.[7]

7: exceptions are COF-5 and UL-MOF-1, stable up to 600 °C in N_2 [66, 67]

2.3.1 Framework

The neutral $[SiO_2]$ and charged $[AlO_2]^-$ tetrahedra are the primary building units (PBU) and connect through an oxygen atom to form SBU, single or double 4- and 6-membered rings or more complex shapes such as the pentasil unit (figure 2.7, b). SBU connect with each other to form chains, sheets, and eventually, three-dimensional zeolite framework. These contain micropores of different dimensions, with cages at the intersections, and zeolites are classified into small-pore 8-membered rings, medium-pore 10-membered rings, and large-pore 12-membered rings. An example of the stepwise formation of the medium-pore MFI framework is shown in figure 2.7, commonly known as ZSM-5 when aluminium is in the framework.

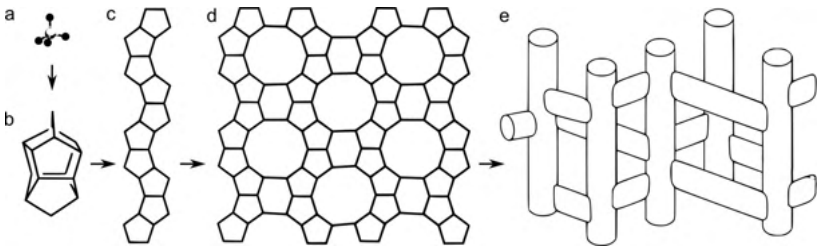

Figure 2.7: Schematic formation of MFI framework from tetrahedra (a), combining to form pentasil units (b), chains (c), sheets with 10-membered rings (d), and finally a three-dimensional structure containing straight and sinusoidal pores or channels (e). Adapted from [68].

To investigate the influence of the framework on the catalytic conversion of dmf into aromatics, a range of different frameworks has been explored, shown in figure 2.8 and table 2.1. One small-pore framework LTA, commonly known as molecular sieve 4A, two small-pore frameworks FER and MFI, and three large-pore frameworks BEA, MOR, and FAU. The dimensions of the micropores are shown (in Å = 10^{-10} m=0.1 nm), as well as the maximum size of the intersections of the pores (cages). Zeolite BEA, or Beta (β), is a special framework as it does not comprise a well-ordered structure but is rather a disordered intergrowth consisting of different polymorphs. To elaborate, its framework is built by stacking layers of SBU units on top of each other. Each layer can translate and bind to another layer in different arrangements, resulting in a final framework with a stacking disorder (pores are not blocked). For clarity, the code BEA will be used throughout this thesis even though the disordered intergrowth is referred to and not a theoretical polymorph of the BEA framework.

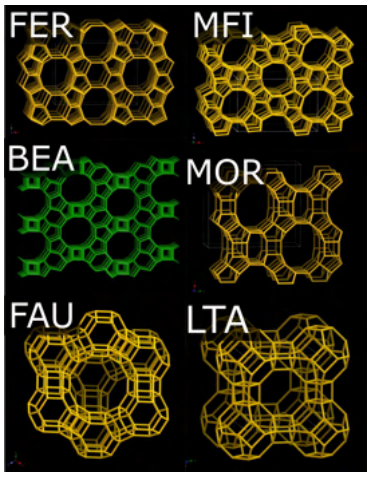

Figure 2.8: Visualisation of the different zeolite frameworks in which the vertices are silicon, aluminium, and oxygen, and the lines their bonds. Zeolite BEA is visualised as polymorph Beta A [65].

Table 2.1: Overview of the different microporous zeolite frameworks and their pore sizes.

Structure	Pore size Å	Max. size Å
LTA[a]	4.0 × 4.0	11.2 [69]
FER	4.2 × 5.4, 3.5 × 4.8 [70]	6.3[65]
MFI	5.6 × 5.4, 5.5 × 5.1 [70]	6.4[65]
BEA	7.6× 6.4, 5.6 × 5.6 [70]	6.5 [65]
MOR	6.5× 7.0, 2.6 × 5.7 [70, 71]	6.7 [65]
FAU	7.4 × 7.4 [70]	11.2 [65]

[a] Pore size can be tuned to 3 × 3 Å or 5 × 5 Å

The selection of the zeolitic framework for a particular catalytic reaction is very important as the size of its pores determines which molecules are able to enter the porous structure and reach the active sites. Additionally, their size determines which products can be formed or are more likely to be formed, directing the selectivity towards the desired products. An overview of the kinetic diameters of several furanics and monocyclic aromatics is shown in table 2.2. The reagent 2,5-dimethylfuran has similar dimensions as benzene, toluene, en para-xylene, while the other xylenes are larger due to the configuration of their side groups. Comparing their diameters to the pore sizes of the zeolites, it appears as though they are too large to enter LTA, FER, and MFI. However, these pore dimensions are determined with atomic radii instead of ionic radii, underestimating the pore size [72], and do not account for the elevated reaction temperatures of 500 °C. At high temperatures, pore dilation and flexibility have been observed, and thus a more accurate pore size approximation are the Norman radii, e.g., pore diameters of 6.2 and 6.3 Å for MFI [73–76].

Table 2.2: Kinetic diameters of furans and BTX, demonstrating their narrow fit in the MFI framework zeolite [73, 77, 78].

Molecule	Kinetic diameter/ Å
Furan	5.10
2-mf	5.30
dmf	5.70
Benzene	5.85
Toluene	5.85
Para-xylene	5.85
Meta-xylene	6.80
Ortho-xylene	6.80

2.3.2 Acidity

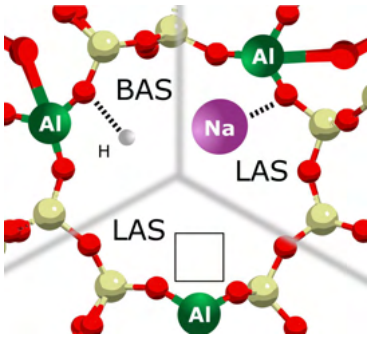

Figure 2.9: Overview of the different types of acid sites in zeolites.

Zeolite acidity is introduced through the isomorphous substitution of a tetravalent silicon atom by a trivalent aluminium atom. Consequently, a negatively charged aluminium tetrahedron, $[AlO_4]^-$, is formed. In order to compensate for this negative charge, a positively charged counterion coordinates to the framework to maintain total framework electroneutrality. Examples include metal cations such as Na^+ and Cu^+, extra-framework aluminium species such as $[AlO]^+$ and $[Al(OH)_2]^+$, or protons, H^+ [79]. This proton creates a Brønsted acid site (BAS) and extra-framework metal species create Lewis acid sites (LAS), shown in figure 2.9. Additionally, when framework defects are present or dehydration occurs, framework silicon or aluminium is not fully saturated and possesses an empty orbital [80]. These coordinatively unsaturated sites are able to accept electron pairs and thus function as a LAS.

The acidity of a zeolite plays an important role in its catalytic performance, and it is relatively easy to substitute framework silicon atoms with metals such as aluminium, or to induce acidity by adding promotors inside the pores of the zeolite through ion exchange or impregnation.

Increasing the number of acid sites can be done by increasing the content of substituting metal, while the strength of each acid site remains largely unaffected.[8] Fortunately, zeolites can also be synthesised by substituting silicon with different trivalent and tetravalent metals, besides aluminium, such as gallium, boron, iron, and titanium.[9] The degree of substitution and the success of the synthesis depends on factors such as the valency of the metal, its electronegativity, and its size (table 2.3).

Both LAS and BAS play an important role in catalysis, promoting reactions like cracking, decarbonylation and dehydration; all involved in the conversion of furans to aromatics. When there are too many acid sites, or when the acid sites are too strong, unwanted reactions may take place. In biomass conversion, the formation of carbonaceous, polycyclic aromatic hydrocarbons (PAH), or graphite-like species can occur, named coke (figure 2.10). These species can block acid sites, block micropores, or completely cover particles, leading to the deactivation of the catalyst. The transport of reactants, products, and coke precursor is facilitated by larger pores, regarding either the micropores or a secondary pore network consisting of meso- and macropores, connecting microporous regions and shortening diffusion pathways. Besides the framework and porosity of the catalyst, the acidity must also be controlled and tuned to promote the formation of monocyclic aromatics while preventing the formation of polycyclic aromatics.

8: at high Al contents, acid sites may be close enough to interact and affect each other's strengths.

9: the term zeolite is officially reserved for materials containing silicon and aluminium and the term zeotype is used when no aluminium is present. These terms may be used interchangeably throughout this thesis.

Table 2.3: Ionic radii of metal cations with a specific oxidation state in tetrahedral coordination [81].

Metal	Ionic radius / pm
Si(IV)	40
Al(III)	53
Ga(III)	61
B(III)	25
Fe(III)	63
Ti(IV)	56

Briefly, zeolites and zeotypes are excellent catalysts for the reaction of dmf into aromatics as they possess the following desired characteristics:

1. Acid sites
   that act as the active sites needed for cracking, decarbonylation, dehydration, and aromatisation reactions involved in the conversion of dmf
2. Micropores
   offering shape- and size selectivity that increases the production of the desired BTX monocyclic aromatics
3. High surface area
   to allow for a high dispersion and number of acid sites, stabilising the catalysts and enhancing the reaction rate
4. High thermal stability
   to withstand a reaction temperature of 500 °C and regeneration temperatures of 600 °C in oxygen.
5. Secondary pore network (potential)
   consisting of meso- and macropores to facilitate mass transport and diffusion of reactants and products, preventing deactivation due to coking

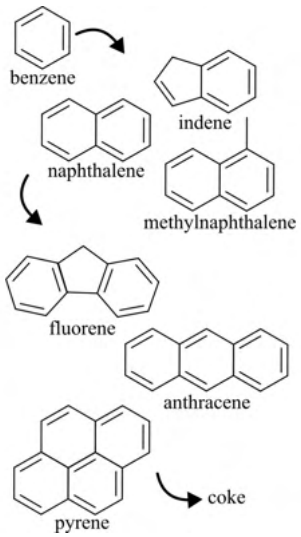

Figure 2.10: Schematic stepwise conversion of benzene into polycyclic aromatic hydrocarbons (PAH), considered coke (precursors).

2.4 Objectives of this thesis

Now that the topic has been introduced and the background has been provided, the aim of this thesis is defined as the following:

To understand the relationship between the properties of the catalyst—that is framework, acidity, and porosity—and its catalytic performance, with regard to activity, selectivity, and stability in the conversion of 2,5-dimethylfuran into aromatics.

This objective will be explored by means of the following research questions:

1. What is the influence of the microporous framework?
2. What is the influence of heteroatom substitution, concerning aluminium and gallium?
3. What is the influence of changing the content of the active element, i.e., aluminium and gallium?
4. What is the influence of a secondary pore network consisting of meso- and macropores?
5. What is the influence of the reaction conditions?

Methodology 3

This section describes the synthesis of the studied catalysts, followed by a description of the utilised characterisation methods and the performed catalytic experiments, described in more detail elsewhere [82].

3.1 Synthesis of the catalyst

Several sets of catalysts have been synthesised and studied, as shown in tables 3.1 and 3.2.

In general, catalysts are named according to the notation *X-Y(Z)*, in which *X* is the cation in the cationic position,[1] *Y* is the three-letter zeolite framework code,[2] and *Z* is the silicon-to-metal ratio,[3] e.g. Al-BEA(12). For the series of Ga-MFI catalysts, the gallium content is denoted in wt.% (section 4.3.3 [83]), e.g, G1.2 for Ga-MFI(1.2 wt.%).

Despite the variety in the studied catalysts, most materials share a similar synthesis protocol based on the hydrothermal sol-gel method (figure 3.1), as described below for metal-substituted MFI framework catalysts [84].

1. Mixing of the precursors.[4] Through a sol-gel process, the precursors form a three-dimensional matrix (Si−M−template, with M=metal like Al or Ga), which is the basis of the zeolite.
2. Crystallisation is followed by filtration, washing, and drying. The dried as-synthesised catalyst (structure A) contains template molecules in its pores (e.g., TPA).
3. Calcination in air removes the organic template via oxidation, after which negative framework charges are compensated by cations like Na^+ (structure B, e.g., Na-Ga-MFI).
4. Ion exchange replaces the Na^+ cations by $NH_4{}^+$ cations, as shown in structure C, e.g., NH_4-Ga-MFI. This is followed by freeze-drying overnight.
5. Calcination converts the ammonium cation into a proton at the cationic position, forming a Brønsted acid site and the final active zeolite (structure D).

1: e.g., TPA^+ for as-synthesised catalysts, Na^+ after calcination, $NH_4{}^+$ after ion exchange, and H^+ after second calcination for the final zeotype

2: e.g., MFI, BEA, FAU

3: a high metal content corresponds to a low Si/Me value.

4: silicon source (tetraethyl orthosilicate, TEOS), aluminium or gallium source, template (TPA and CTAB), a mineraliser or pH control agent (NaOH), and a solvent (H_2O)

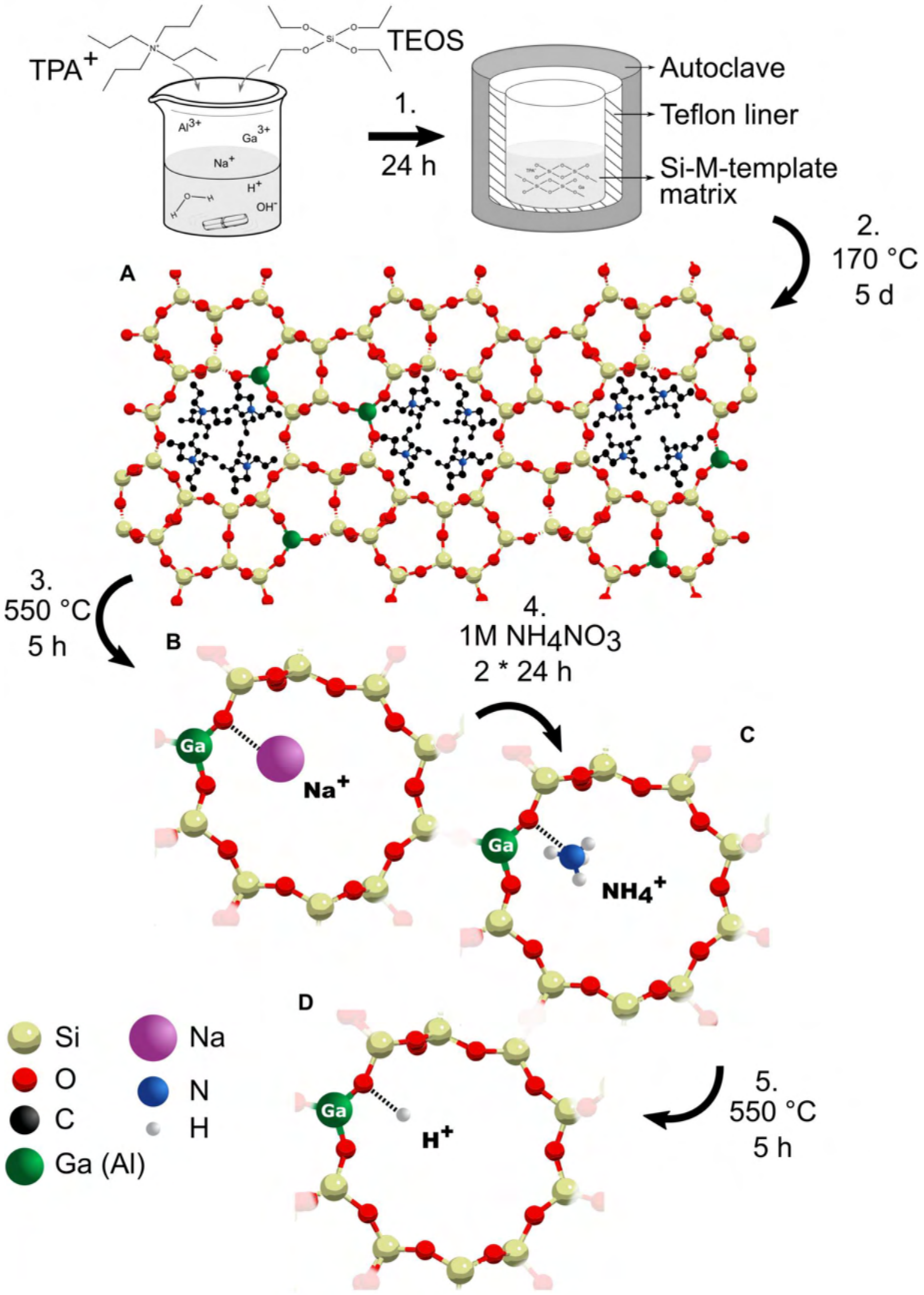

Figure 3.1: Schematic overview of the bottom-up synthesis of metal-substituted MFI framework zeolite.

A complete overview of the catalysts studied in this thesis is shown in tables 3.1 and 3.2, organised in the order of appearance, as indicated by the subchapters (#). The tables include the names of the catalysts, the substituting or impregnating metal or heteroatom (M), the micro- or mesoporous frameworks (Fw), the silicon-to-metal atomic ratios (Si/M) as determined with XRF or provided by the manufacturer, the synthesis conditions, and the commercial supplier or the parent material. Materials are obtained commercially (com.) or synthesised, either hydrothermally or through post-synthesis treatment of parent material such as impregnation, desilication, and dealumination.

Table 3.1: Part I: Overview of the catalysts studied in this thesis, appearing in sections 4.1, 4.2, and 4.3. Blank cells are either not available or not applicable.

#	Sample	M	Fw	Si/M	Synthesis	Origin/Parent
4.1	FER	Al	FER	10		com. NH_4, AA[a]
	MFI	Al	MFI	11		com. H, AN[a] [85]
	MOR	Al	MOR	12		com. NH_4, AA[a]
	BEA	Al	BEA	10		com. NH_4, AA[a]
	FAU	Al	FAU	15		com. H, AA[a]
	LTA3	Al	LTA	1		com. K, SA[a]
	LTA4	Al	LTA	1		com. Na, SA[a]
	LTA5	Al	LTA	1		com. Ca, SA[a]
4.2	Si-MFI/G0	Si	MFI	∞	5d, 170 °C [85, 86]	
	Al-MFI(41)	Al	MFI	41	5d, 170 °C [85, 86]	
	Ga-MFI(33)	Ga	MFI	33	5d, 170 °C [85, 87]	
	La-MFI(120)	La	MFI	120	5d, 170 °C	
	In-MFI(70)	In	MFI	70	5d, 170 °C	
	deAl-BEA	Al	BEA	1309	Dealumination[b] [88]	NH_4-AlBEA(12)
	Ga(10)-deAlBEA	Ga	BEA	10	Ga impregnation[c]	deAl-BEA
	Ga-BEA(13)	Ga	BEA	13	10 d, 135 °C [89, 90]	
	P-BEA	P	BEA	27	P impregnation[d][88]	deAl-BEA
4.3	Al-BEA(19)	Al	BEA	19		com. NH_4, TS[a]
	Al-FAU(2.6)	Al	FAU	2.6		com. NH_4, AA[a]
	Al-FAU(6.1)	Al	FAU	6.1		com. NH_4, AA[a]
	Al-FAU(15)	Al	FAU	15		com. H, AA[a]
	Al-FAU(30)	Al	FAU	30		com. H, AA[a]
	deAl-FAU(39)	Al	FAU	39	Dealumination[e] [91]	NH_4-Al-FAU(6.1)

[a] Commercial samples are obtained in their ammonium (NH_4), proton (H), potassium (K), sodium (Na), or calcium (Ca) form, from Alfa Aesar (AA), AkzoNobel (AN), Sigma-Aldrich (SA), or Thermofisher Scientific (TS).
[b] 1 d at 80 °C in 15 M HNO_3 in an autoclave. Wash with H_2O. Freeze-dry for 16 h. Calcine 3 h at 550 °C (2 °C/min).
[c] 1 g zeolite, 10ml 0.1 M $Ga(NO_3)_3 \cdot 8\,H_2O$, 5 h at 90 °C. Freeze-dry for 16 h. Calcine 3 h at 550 °C (2 °C/min).
[d] 1 g zeolite, 8 ml 0.0004 M H_3PO_4, 3 h at 80 °C. Dry at 100 °C. Calcine 3 h at 600 °C (6 °C/min).
[e] 2 h at 60 °C in 7 M HNO_3 in an autoclave. Wash with H_2O. Freeze-dry for 16 h. Calcine 3 h at 550 °C (2 °C/min).

Table 3.2: Part II: Overview of the catalysts studied in this thesis, appearing in sections 4.3, 4.4 and 4.5. Parent materials are in the protic form, unless otherwise noted.

#	Sample	M	Fw	Si/M	Synthesis	Parent
4.3	Ga(10)/Al-BEA(12)	Ga/Al	BEA	10/12	Ga imp.[a]	Al-BEA(12)
	Ga(11)/Al-BEA(19)	Ga/Al	BEA	11/19	Ga imp.[a]	Al-BEA(19)
	Ga(24)/Al-FAU(2.6)	Ga/Al	FAU	24/2.6	Ga imp.[b]	Al-FAU(2.6)
	Ga(28)/Al-FAU(6.1)	Ga/Al	FAU	28/6.1	Ga imp.[b]	Al-FAU(6.1)
	Ga(46)/Al-MOR(10)	Ga/Al	MOR	46/10	Ga imp.[b]	Al-MOR(10)
4.3	G0.5	Ga	MFI	238	5d, 170 °C [83]	
	G1.2	Ga	MFI	95	5d, 170 °C [83]	
	G3.1	Ga	MFI	34	5d, 170 °C [83]	
	G6.0	Ga	MFI	17	10 d, 170 °C [83]	
	G6.7	Ga	MFI	15	5d, 170 °C [83]	
	G8.6	Ga	MFI	11	5d, 170 °C [83]	
	G11	Ga	MFI	8	5d, 170 °C [83]	
4.4	$G1.2_{meso}$	Ga	MFI	81	Des.[c] [92, 93]	G1.2
	$G3.1_{meso}$	Ga	MFI	27	Des.[c] [92, 93]	G3.1
	$G6.0_{meso}$	Ga	MFI	19	Des.[c] [92, 93]	G6.0
	$G6.7_{meso}$	Ga	MFI	19	Des.[c] [92, 93]	G6.7
	$G8.6_{meso}$	Ga	MFI	15	Des.[c] [92, 93]	G8.6
	$G11_{meso}$	Ga	MFI	11	Des.[c] [92, 93]	G11
4.4	MCM0	Ga	MCM-41	∞[c]	3 d, 100 °C [92, 94]	
	MCM3.1	Ga	MCM-41	36[c]	3 d, 100 °C [92, 94]	
	MCM8.6	Ga	MCM-41	12[c]	3 d, 100 °C [92, 94]	
	MCM8.6-b	Ga	MCM-41	12[c]	3 d, 100 °C [92, 94]	
	MCM11	Ga	MCM-41	9[c]	3 d, 100 °C [92, 94]	
	MFI/MCM0	Ga	MFI/MCM-41	∞[c]	2-step syn.[d] [92, 94]	MCM0[e]
	MFI/MCM3.1	Ga	MFI/MCM-41	36[c]	2-step syn.[d][92, 94]	MCM3.1[e]
	MFI/MCM8.6	Ga	MFI/MCM-41	12[c]	2-step syn.[d] [92, 94]	MCM8.6[e]
	MFI/MCM8.6-b	Ga	MFI/MCM-41	12[c]	2-step syn.[d] [92, 94]	MCM8.6-b[e]
	MFI/MCM11	Ga	MFI/MCM-41	9[c]	2-step syn.[d] [92, 94]	MCM11[e]
	SPP1.2	Ga	MFI	93	5d, 120 °C [92, 95]	
	SPP2.4	Ga	MFI	45	5d, 120 °C [92, 95]	
	SPP3.6	Ga	MFI	29	5d, 120 °C [92, 95]	
4.5	G8.6-b	Ga	MFI	11	5d, 170 °C, static	
	G8.6-c-SO	Ga	MFI	11	5d, 170 °C, static	
	G8.6-c-RO	Ga	MFI	11	5d, 170 °C, rot.	

[a] 1 g zeolite, 10ml 0.1 M $Ga(NO_3)_3 \cdot 8\,H_2O$, 5 h at 90 °C. Freeze-dry for 16 h. Calcine 3 h at 550 °C (2 °C/min).
[b] 1 g zeolite, 12.5 ml 0.02 M $Ga(NO_3)_3 \cdot 8\,H_2O$, 24 h at 60°C. Freeze-dry for 16 h.
[c] Desilication: 1 d 170 °C in 0.2 M TPAOH in an autoclave. Wash with H_2O. Freeze-dry for 16 h. Calcine 3 h at 550 °C (2 °C/min).
[c] Theoretical Si/Ga based on the composition of the synthesis gel. No XRF was performed on the synthesised catalysts.
[d] 3 d at 100 °C followed by 6 d at 160 °C [92, 95].
[e] Ga-MFI/MCM-41 series uses same gel compositions as Ga-MCM-41 but its own one-pot 2-step hydrothermal synthesis, so Ga-MCM-41 is not the parent material but related.

3.2 Reactor set-up

The heterogeneous catalytic conversion of dmf into aromatics was performed in a flow reactor (figure 3.2) operating at atmospheric pressure, described in detail elsewhere [82].

In short, catalyst powder is pressed into a pellet, crushed, and sieved to a particle size of between 355 to 450 µm.[5] Roughly 75 mg of powder was loaded in a quartz tube, held in place with silanised quartz wool (figure S1, paper I [84]), and the temperature was regulated via resistive heating and thermocouples. Stainless-steel tubing was heated to 190 °C to prevent condensation in the lines and the feed gases were introduced via mass flow controllers (MFC). The liquid reagent dmf was introduced using argon as carrier gas through a glass bubbler at room temperature. The stream was further diluted with argon to dmf concentrations of approximately 300 to 1100 ppm, while operating at a constant total flow of 300 mL_N/min.[6] Occasionally, the dmf signal was calibrated to account for minor differences in room temperature. Before the reaction, the catalyst was heated to 500 °C (10 °C min^{-1}) in 20 % O_2 to remove species adsorbed from air such as CO_2 and water. The reaction was generally performed at 500 °C, unless otherwise stated, for reaction times ranging from 1 to 48 h. After reaction, formed coke was removed in 20 % O_2 (600 °C) and quantified via detection of CO and CO_2.

The product gas stream was analysed and quantified using online ion-molecule-reaction mass spectrometry (IMR-MS) and Fourier transform infrared (FTIR) spectroscopy, as described in the next section (3.2.1).

5: to prevent the built-up of pressure (pressure drop) caused by feed gas that cannot pass through a fine-particle powder bed.

6: a typical dmf concentration of 720 ppm corresponds to a weight hourly space velocity (WHSV) of 0.66±0.04 $g_{dmf}\ g_{cat}^{-1}\ h^{-1}$.

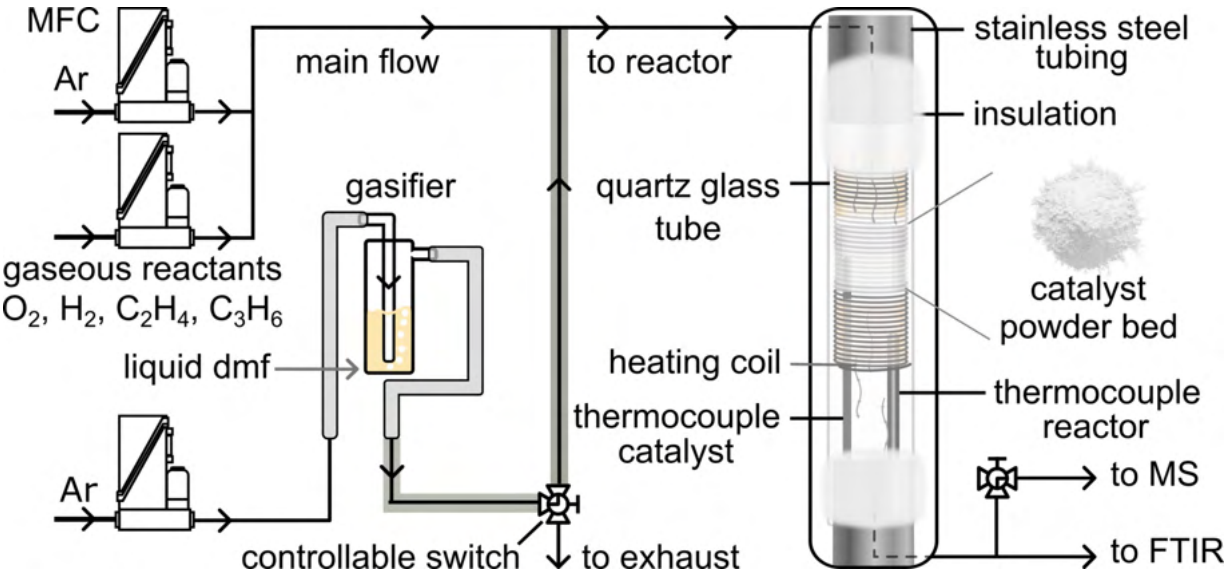

Figure 3.2: Schematic overview of the flow reactor set-up used in the catalytic study of dmf into aromatics at high temperatures. Adapted from [96].

$$M + e \longrightarrow M^{\bullet+} + 2e \quad (3.1)$$

$$M^{\bullet+} \longrightarrow A^{+} + B^{\bullet} \quad (3.2)$$

$$M^{\bullet+} \longrightarrow C^{\bullet+} + D \quad (3.3)$$

$$M + G^{+} \longrightarrow M^{+} + G \quad (3.4)$$

Table 3.3: Ionisation potentials in IMR-MS [96].

Ioniser	Potential/eV
EI	70
Kr	14.00
Xe	12.12
Hg	10.44

7: Quantification may be challenging as not all analytes are ionised to the same extent, demanding the use of internal standards with known concentrations.

8: IR-active molecules experience a change in their dipole moment upon vibration.

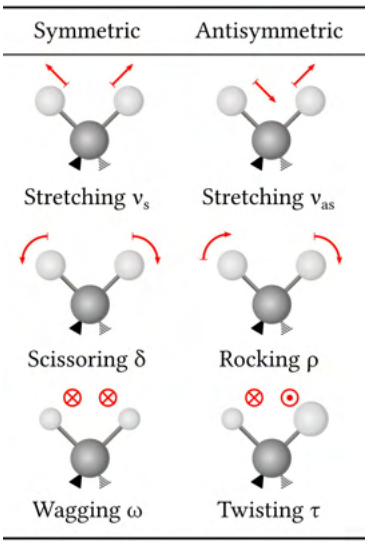

Figure 3.3: Vibrational modes of $-CH_2$ as part of a CH_2R_2 molecule. Adapted from [96].

$$A = \epsilon l c \quad (3.5)$$

with A=absorbance, ϵ=molar attenuation coefficient, l=optical path length, c=concentration

9: for quantification, frequency regions were selected in which no overlap of IR bands was observed, shown in paper I (table S1).

3.2.1 Product identification

Mass spectrometry (MS) can be used to analyse complex gas mixtures. After ionisation of the analytes by electron impact (EI), the formed radical cations (eq. 3.1) fragment further by elimination of a neutral radical (eq. 3.2) or a molecule (eq. 3.3).

This results in complex fragmentation patterns that may be hard to deconvolute, especially when studying hydrocarbons that are built up from the same components. One solution involves the use of a softer ionisation source, for example, ionised primary atomic gas like xenon and mercury, which are first ionised by EI and subsequently collide and ionise the analytes with a lower energy (table 3.3). As a result, the intact analyte molecule is ionised and does not fragment further (eq. 3.4), allowing for the distinction between e.g., benzene and toluene, as EI would fragment toluene into benzene$^+$.

Here, a quadrupole ion-molecule-reaction (IMR) MS has been used (Airsense Compact, V&F) with EI, Hg, and Xe as ionisation sources. MS was primarily used qualitatively to validate the use of FTIR, detect non-IR active species, detect products in low concentrations (<1 ppm), or compare catalysts.[7] An overview of the used mass-to-charge (m/z) ratios is shown in paper I (table S1), as developed by Sauer et al. [97].

Besides IMR-MS, the product gas stream was analysed with Fourier-Transform Infrared (FTIR) spectroscopy. Upon irradiation by infrared (IR) photons, IR-active molecules[8] can absorb discreet amounts of energy and start vibrating, stretching, bending, and more (figure 3.3). The energy or frequency of the absorbed IR radiation is characteristic of each bond or functional group, allowing the speciation of the gas mixture by analysing the transmitted IR spectrum [45, 98, 99].

Here, the product gas stream was analysed and quantified using an FTIR gas analyser (MKS MultiGas 2030), recording IR spectra each second between 4000 cm^{-1} to 600 cm^{-1}, with a resolution of 0.5 cm^{-1}. According to the Beer-Lambert law (eq. 3.5), IR absorption is linearly correlated to the concentration of the molecule, allowing for its quantification by comparing the spectra to a library of pure compounds and known concentrations, limiting the number of detected products [97].[9] Despite the disadvantage of a limited product library, its high time resolution (s^{-1}) is a valuable advantage, allowing for monitoring the performance of the catalysts closely. This is an advantage compared to other techniques such as gas chromatography (GC) coupled MS [42, 100].

Subsequently, the concentrations are used to calculate the carbon balance, conversion, and selectivity. The carbon mass balance is determined by summing all carbon detected as products or coke, and dividing this by the carbon of the dmf feed. Typically,

the carbon mass balance is around 90 %, indicating that 10 % of the products were not identified.[10] The conversion (X) was determined with eq. 3.6, in which the product concentrations (C) are normalised to the number of carbon atoms (n) in that specific molecule (i) to account for reaction stoichiometry.[11]

$$X = 1 - \frac{C_{\mathrm{dmf}}}{\sum \frac{n}{6} \cdot C_{\mathrm{product,i}} + C_{\mathrm{dmf}}} \tag{3.6}$$

In a similar manner, the selectivity S of each product has been calculated with eq. 3.7. Neither in the calculation of the conversion nor in that of the selectivity, has the carbon mass balance been taken into account, indicating that the true values are slightly lower. Likewise, the selectivity to coke has not been included in the selectivities of the other products. As it can only be quantified after the reaction, no time-resolved data is available.

$$S = \frac{n \cdot C_{\mathrm{product,i}}}{6 \sum \frac{n}{6} \cdot C_{\mathrm{product,i}}} \tag{3.7}$$

10: undetected species are not part of the FTIR library of reference compounds or they remain as coke on the catalyst due to incomplete regeneration.

11: e.g., 1 dmf molecule (6 carbons) can be converted into 2 propene molecules (3 carbons), disregarding oxygen. Therefore, the propene concentrations must be divided by 6 / 3 = 2.

3.3 Characterisation of the catalyst

To establish catalyst design principles, the structures and properties of the catalysts must be studied extensively. An overview of the employed characterisation techniques is provided below.

3.3.1 Elemental composition

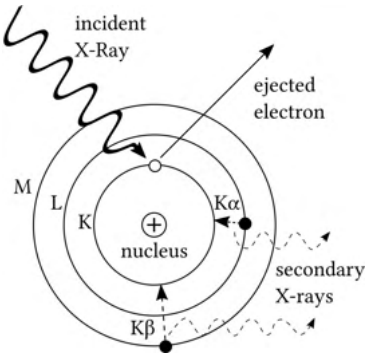

Figure 3.4: Primary mechanism of XRF.

The elemental composition of the catalyst was determined with X-ray fluorescence (XRF) spectroscopy, energy-dispersive X-ray spectroscopy (EDX), and thermogravimetric analysis (TGA) coupled with differential scanning calorimetry (DSC).

In XRF, the catalyst material is irradiated with X-rays, exciting the atoms through inelastic scattering by expelling an electron out of the inner shells. When an electron from the inner shell (K-shell) is expelled, this vacancy may be filled by a higher-energy electron from the second or third shell (L- and M-shell), as shown in figure 3.4. The excess energy is released as a characteristic X-ray photon, which can be detected, compared to a calibrated standard material, and subsequently quantified to obtain the elemental composition of the catalyst. Elements with an atomic number $Z > 9$ were detected on a PANalytical AXIOS XRF spectrometer, equipped with a Rh anode X-ray source, while the oxygen content is derived by assuming its presence as part of the oxides SiO_2 and Ga_2O_3.

The principle of EDX is similar to XRF, with the main difference being the use of a high-energy electron beam as excitation source, typically from an electron microscope (3.5).[12] While XRF determines the bulk composition, EDX has a lower penetration depth and may detect compositional differences in the surface layers of the material. EDX analysis was performed under vacuum at 20 kV with an Oxford Inca EDX after recording electron images on a FEI Quanta 200 FEG ESEM, as well as at 300 kV on a FEI Titan 80-300 TEM.[13] For EDX/SEM, powder catalysts were deposited on a carbon-taped Al holders after which they were coated with 1.67 to 4 nm gold (Au) to prevent charging effects. For EDX/TEM, catalysts were dispersed on Holey Carbon Film supported Cu grids. EDX maps were typically collected to display elemental dispersion, although point or line spectra have also been recorded.

TGA/DSC is primarily used to study the thermal stability of the final catalysts, but can also be used to obtain information about the composition of the materials. TGA monitors the mass of the material while heating it in a controlled atmosphere,[14] while DSC monitors the heat flow allowing for identification of e.g., exo- and

12: EDX is often coupled to scanning or transmission electron microscopy, obtaining a spatial elemental distribution.

13: pixel size of 3 nm

14: e.g., nitrogen or air

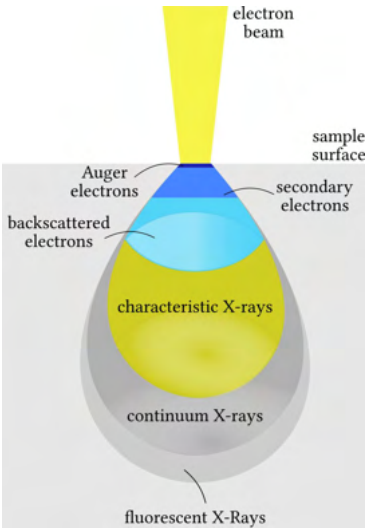

Figure 3.5: Schematic overview of the interaction volume of SEM.

endothermic processes. In this work, TGA/DSC is performed on as-synthesised catalyst to study the content and decomposition of the template molecules, revealing the minimum temperature required for calcination of as-synthesised or NH_4-catalysts. Additionally, the water content of the final protic catalyst has been determined with TGA, as hydrogen and oxygen are too light to detect with XRF.

3.3.2 Structure and porosity

The structure and porosity of the catalysts were determined with X-ray diffraction (XRD), scanning electron microscopy (SEM), transmission electron microscopy (TEM), high-angle annular dark-field scanning transmission electron microscopy (HAADF-STEM), and nitrogen physisorption.

Besides inelastic scattering of X-rays, relevant in XRF, elastic scattering also takes place, which can be observed with XRD. Because X-rays have wavelengths of the order of interatomic distances (Å), scattered waves can either combine in phase, producing constructive interference and resulting in signal peaks, or out of phase, leading to destructive interference (figure 3.6). Using Bragg's law (eq. 3.8 [101]), the spacing between the crystal lattice planes can be determined from angles at which peaks are observed, which is compared to a reference database for phase identification. The intensity of the peak is mainly influenced by the type and arrangement of the atoms within the crystalline structure, while its shape is affected by the presence of lattice distortions originating from defects [102]. However, experimental factors introduced during sample preparation can also influence the position, intensity, and shape of the peaks [103].

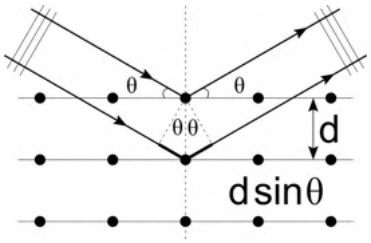

Figure 3.6: Schematic representation of Bragg's law [101], equation 3.8.

$$2dsin\theta = n\lambda \tag{3.8}$$

with d=interplanar spacing, θ=incident angle, n=diffraction order, and λ=wavelength

In this work, powder XRD was measured on a Bruker AXS D8 Discover diffractometer with monochromatic Cu-Kα radiation (1.5406 Å) from 5 to 50 °. Measurements were typically performed with a fixed sample illumination to maximise the signal-to-noise ratio (SNR), at the cost of intensity of low angle peaks.[15] Further commonly used settings are 1 to 5 mm distance of the air scatter knife, no rotation, increments of 0.01 to 0.02 °, and acquisition times of 1 to 2 s.

15: relative peak intensities were influenced and could not be used for structural determination.

The morphology of the catalysts was studied with SEM, TEM, and HAADF-STEM, based on the detection of scattered or transmitted electrons after illuminating the material with an electron beam. SEM images were recorded on a Zeiss Ultra 55 FEG SEM (1.5 kV), detecting secondary electrons (figure 3.5) to obtain information on the size and shape of the crystals. TEM and HAADF-STEM were recorded on a FEI Titan 80-300 TEM (300 kV), obtaining

high-resolution information on the dispersion of heavy elements throughout the frameworks, as well as the presence of macro- and mesopores or voids.

The porosity of the catalyst was studied with nitrogen physisorption, allowing for the determination of the surface area (SA), pore volume, and pore size distribution (PSD). At 77 K (-196 °C), nitrogen is incrementally dosed and adsorbs to the surface of the material through Van der Waals attractions. After an equilibrium between adsorption and desorption has been reached, the relative pressure[16] is registered and additional nitrogen is dosed, gradually filling the pores. Likewise, after adsorption, nitrogen desorbs when reducing the pressure, together forming the adsorption and desorption isotherms whose shapes convey information on the size, type, and abundance of the pores [104]. Due to pore confinement, the equilibrium pressure p inside the pores is lower than the bulk saturation pressure p_0, resulting in capillary condensation. As adsorption layers build up on the surface, the pore spontaneously fills with liquid nitrogen at a critical pressure, accompanied by a sharp increase in adsorbed nitrogen, while simultaneously forming a curved vapour-liquid interface to minimise the surface energy, named the meniscus. Layer-by-layer pore filling dominates in micropores because they are only a few nitrogen molecules wide and capillary condensation dominates in mesopores, which can be described by the Kelvin equation that is based on the Laplace pressure. Desorption of nitrogen does not always follow the same path as the adsorption, giving rise to delayed desorption called hysteresis. While the formation of the meniscus was spontaneous and governed by a negative Gibbs free energy change, desorption requires breaking the attractive interactions between liquid nitrogen molecules and each other and the solid surface, costing energy and requiring a lower relative pressure p/p_0. The size and shape of the hysteresis loops convey information about the size, shape, and connectivity of meso- and macropores.

16: by normalising the isotherm through division with the saturation vapour pressure (p_0), isotherms can be compared across different instruments, temperatures, and adsorbates.

$$\frac{p/p_0}{v(1-(p/p_0))} = \frac{c-1}{v_m c}\left(\frac{p}{p_0}\right) + \frac{1}{v_m c} \tag{3.9}$$

with p = equilibrium pressure, p_0 = saturation pressure, v = quantity of adsorbed gas, v_m = quantity of monolayer adsorbed gas, c = BET constant

Analysis of the isotherms is described by adsorption models, evolving from Langmuir (1916 [105]) to Brunauer, Emmett, and Teller (BET, 1938 [106]), Barrett, Joyner, and Halenda (BJH, 1951 [107]), Dubinin and Astakhov (1971, DA [108]), and to non-local density functional theory (NLDFT, 1989 [109]). Although the consensus is that adsorption in microporous materials is most accurately described with NLDFT, its need for computational resources and high-quality adsorption data limits its application. Consequently, simpler models like the BET model (eq. 3.9) are used, wrongfully assuming adsorption to occur layer-by-layer on individual sites without interaction between N_2 molecules [106, 110]. This model produces a specific surface area (in $m^2\,g^{-1}$) which is rather regarded in this thesis as an apparent surface area (SA), useful for qualitative comparisons within classes of frameworks

[83, 104, 111–115]. To minimise the additional errors introduced by the manual selection of the adsorption points, several criteria[17] [112] have been followed, which were confirmed by a computational approach (BETSI [114]).

The microporous volume (V_{mic}) and external (mesoporous) volume (S_{ext}) of the catalyst have been determined with the t-plot method, in which the thickness of the adsorbed layer is either derived from a similar non-porous reference or calculated using the Harkins-Jura equation (3.10 [116]). As the t-plot method uses the BET-derived surface area, its use for microporous materials is also flawed [117, 118]. The selected points should start after micropore filling has completed and end before mesopore filling or capillary condensation begins, e.g., from 5.0 to 8.0 Å [118].

The pore size distribution can be divided into the micropore region (<2 nm)[18] and the meso- and macropore region (>2 nm). Micropore size distributions are determined with a semi-empirical model like Horvath-Kawazoe [119], which is adapted for cylindrical and spherical micropores [120, 121]. Mesopore size distributions are determined with the BJH model and the Harkins-Jura equation. The adsorption curve has been selected because the desorption curve may display artifacts related to the mechanical stability of nitrogen instead of to the porosity (tensile strength effect, TSE [122, 123]).

Although nitrogen is the most commonly used adsorbate in physisorption studies, its inherent quadrupole moment[19] results in adsorbate-adsorbate interactions and oriented adsorption to surfaces, introducing an uncertainty of up to 20 % in its molecular cross-sectional area [124]. Argon is a superior alternative as it possesses no quadrupole moment, thus being less reactive and sensitive [125]. Argon physisorption should be performed at its boiling point of 87 K (−186 °C), although physisorption at 77 K has appeared insightful for some meso- and macroporous materials [126–129].

In this thesis, nitrogen physisorption was performed on a Micromeritics Tristar 3000 instrument with supplementary low-pressure physisorption for micropore size distribution performed on Micromeritics ASAP 2020 plus. Pretreatment was performed at 90 °C for 1 h followed by 250 °C for 16 h (10 °C/min), under nitrogen flow. On the ASAP 2020 plus, pretreatment was performed with a similar temperature profile but up to 350 °C, directly on the analysis port under vacuum.

17: Rouquerol critera:

- $v(1-(p/p_0))$ must increase continuously with p/p_0.
- The constant c must be positive.
- The p/p_0 value corresponding to v_m should be within the selected linear range.

$$log\frac{p}{p_0} = B - \frac{A}{v^2} \tag{3.10}$$

with constants B and A

18: requiring adsorption points at very low pressures of $p/p_0 \geq 10^{-5}$ for MFI zeolites

19: non-spherical charge distribution due to its linear shape

3.3.3 Acidity

The acidity of a catalyst has been investigated by using basic probe molecules, like ammonia in NH_3-temperature programmed desorption (TPD) and pyridine in diffuse reflectance infrared Fourier-transform spectroscopy (DRIFTS). These probe molecules are both basic molecules that bind to Lewis acid sites (LAS) and Brønsted acid sites (BAS) in the catalyst.

Ammonia coordinates to BAS through hydrogen bonding[20] or proton transfer,[21] while the coordination to LAS is more complex due to the different types of LAS ([130]). The NH_4^+ vibration can be detected with DRIFTS [131] or solid-state nuclear magnetic resonance (ssNMR) [132], while ammonia can also be desorbed and detected with FTIR [133–135]. Advantages of using NH_3 as a probe molecule are its low cost, its small kinetic diameter that allows it to access micropores, and its ability to indiscriminatingly bind to all acid sites. This last point is a double-edged sword, as the different types of acid sites can not be distinguished by ammonia [136].

20: $NH_3 \cdots HOZ$ with Z=zeolite

21: $NH_4^+ - O^- Z$

Here, NH_3-TPD was performed in the flow reactor set-up before catalytic testing, directly after, and after regeneration in O_2 to obtain the acid site density (number of acid sites per gram catalyst) of the catalyst in its fresh, coked, and regenerated state, respectively. Generally, the catalyst was saturated by 400 ppm NH_3 in Ar for 90 min at 100 °C, which was followed by purging with Ar for 90 min to desorb weakly bound physisorbed ammonia. Afterwards, the temperature was increased to 600 °C (10 °C/min), leading to the release of ammonia and its detection with FTIR when the bonds are broken: the stronger the acid site, the higher the temperature of desorption.[22] The resulting NH_3-TPD profiles (figure 3.7) were decomposed into different peaks, each belonging to a specific type of acid type with a specific strength. The profiles were integrated, converted to acid site density (in mmol g^{-1}), and plotted against temperature.

22: the catalyst remained at 600 °C for 10 min to ensure complete desorption.

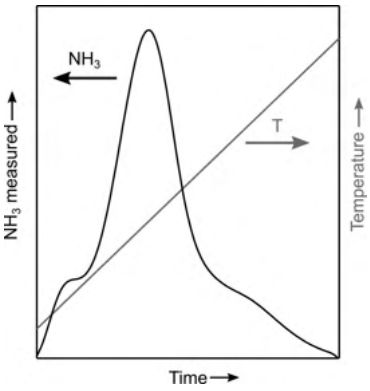

Figure 3.7: Example of an NH_3-TPD profile in which a linear ramp in temperature (grey, right axis) results in desorption and detection of NH_3 (black, left axis) over time.

To be able to distinguish between BAS and LAS, pyridine has been used as another basic probe molecule. Pyridine coordinates to a BAS to produce the pyridinium ion (figure 3.8), which can be detected by FTIR and DRIFTS, as it absorbs IR of a different wavelength (energy) than pyridine coordinated to a LAS. After saturation of the catalyst, a purging step in vacuum (transmission FTIR) or argon (DRIFTS) removes physisorbed and gas phase pyridine, after which the absorption bands are detected and quantified using the Beer-Lambert law (equation 3.5). Although DRIFTS offers a lower spectral resolution due to scattering and undefined path lengths, it has been used in this thesis due to instrumental availability. Here, DRIFTS was measured on a KBr supported powder bed of

catalyst in a reaction chamber with CaF_2 windows, using a Bruker VERTEX 70 (section S2, figure S1 paper II [83]). Before adsorption of pyridine, the catalyst was pretreated in 15 % O_2 at 300 °C (maximum temperature achievable) and background FTIR spectra were recorded in Ar at 150 and 300 °C. Then, the catalyst was saturated with pyridine at 300 °C, purged in Ar, and background-subtracted spectra were recorded to probe the strong acid sites (desorbing at temperature >300 °C). Afterwards, this process was repeated at 150 °C to probe both the weak and the strong acid sites. For BAS, the peak around 1545 cm^{-1} was integrated (± 25 cm^{-1}) and for LAS, the peak around 1455 cm^{-1}(± 15 cm^{-1}), assuring no overlap with neighbouring peaks (figure S9, paper II [83]). The integrated areas were corrected for the difference in molar attenuation coefficients ϵ (ϵ_{BAS}=1.67 cm µmol^{-1}, ϵ_{LAS}=2.22 cm µmol^{-1} [137]). As a result of the effects of the scattering, particle size, and bed packing, it is challenging to relate peak intensity obtained with pyridine DRIFTS to an absolute number of acid sites. Therefore, it has been used qualitatively to obtain the distribution between the weak and strong LAS and BAS, while the total acid site density was determined with NH_3-TPD.

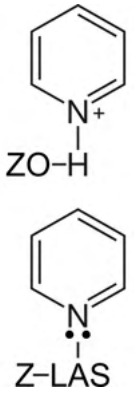

Figure 3.8: Schematic representation of pyridine bonded to a BAS (top) or LAS (bottom), with Z=zeolite.

Results and discussion 4

This chapter presents the main findings of this work, divided into subchapters that each address one of the research questions, as summarised below:

1. The first subchapter deals with the selection of the microporous framework.
2. The second subchapter investigates the choice of the substituting metal or heteroatom.
3. The third subchapter explores the influence of varying the aluminium or gallium content.
4. The fourth subchapter examines the effect of introducing a secondary network of meso- and macropores in the catalyst.
5. The fifth subchapter evaluates the impact of the reaction conditions on the catalyst and its catalytic performance.
6. The sixth and final subchapter reveals the mechanistic insights established in this work.

4.1 The selection of the microporous framework

This section describes an initial screening study of different Al-based microporous frameworks, shown in tables 3.1 and 4.2, including small-pore (LTA), medium-pore (FER, MFI), and large-pore (BEA, MOR, FAU) zeolites. Their dmf conversion (X, eq. 3.6) and selectivity to benzene, toluene, and xylenes (S_{BTX}, eq. 3.7) were studied, as shown in figures 4.1 and 4.2 .

Initially, most frameworks catalyse the complete conversion of dmf, which then rapidly drops, already after five or ten minutes for FER and MOR, respectively. Catalyst deactivation for BTX production is typically caused by the formation of coke (section 2.3, figure 2.10), which block particles, micropores, and acid sites, rendering them unable to further convert any reactants. Deactivation of FAU and BEA is more gradual, decreasing to 30 and 44 % conversion after 1 hour (h) of time-on-stream (TOS). The MFI framework maintains a high conversion for the highest duration, dropping from 84 % at 30 minutes (min) to 18 % after 1 h TOS.

While a high conversion is sought after, a high selectivity towards the desired BTX products is at least as important. S_{BTX} at the start of the reaction is roughly 60 % for MFI, 50 % for BEA and MOR, and 35 % for FER and FAU.[1] Like the conversion, S_{BTX} also decreases over the course of the reaction, with the highest selectivity of 30 % after 1 h, displayed by MFI. The LTA catalysts,

1: Side-products include CO, CO_2, H_2O, methylfuran, olefins like ethene and propene, isomerisation products like 2,4-dimethylfuran (2,4-dmf), 2-methyl-2-cyclopentenone (2-mcpo), and 3-methyl-2-cyclopentenone (3-mcpo), and polyaromatic rings like indene and naphthalene (figures 2.10 and 4.6).

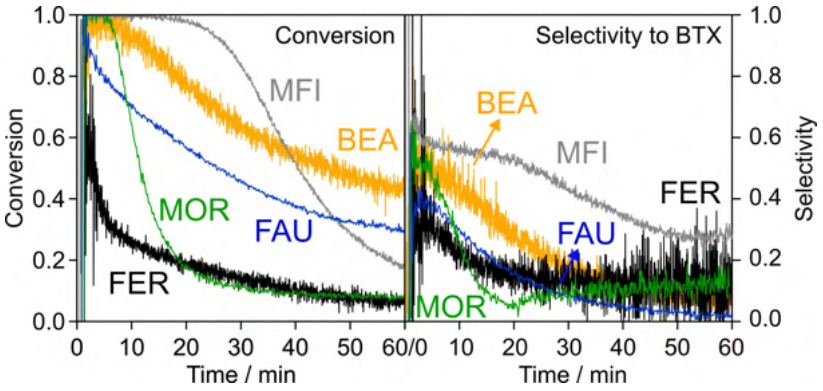

Figure 4.1: Conversion of dmf (left panel) and selectivity towards BTX (right panel) over zeolites with different frameworks, including FER (black), MFI (grey), BEA (orange), MOR (green), and FAU (blue). Concentrations are measured every 2, 4, 64, 7, and 7 s, respectively.

in which their number denotes their pore size in Å, display an initial high selectivity that drops after a few minutes to 15 % for LTA4 or 3 % for LTA3 and LTA5. Selectivity to BTX is the highest over LTA5, peaking at 58 % after 1 min and then dropping to 22 % after 1 TOS. Although the actual pore diameters have expanded at a temperature of 500 °C, dmf with a kinetic diameter of 5.7 Å [73] will likely not be able to enter the micropores of at least LTA3, allowing only the acid sites on the external surface to participate in the reaction.

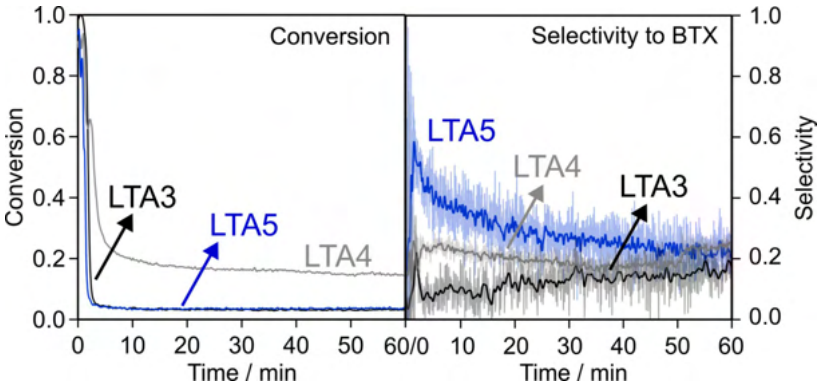

Figure 4.2: Conversion of dmf (left panel) and selectivity towards BTX (right panel) over LTA zeolites with different pore sizes, including 3 Å (black), 4 Å (grey), and 5 Å (blue). Concentrations are measured every 4 s and the selectivity is smoothed for clarity (binomial, bounce, factor 20), while displaying the raw signal in the shaded area.

Elaborating on the product distribution, benzene and toluene are detected with FTIR while xylenes are produced in lower quantities (<1 ppm) and only detected by MS. Therefore, conversion experiments shown in this thesis focus on benzene and toluene, quantified with FTIR. Several of the studied frameworks favour the production of benzene while others favour the production of toluene, as shown in table 4.1 (arbitrary units). Medium-pore catalysts FER and MFI, and large-pore BEA, favour the formation of benzene, while toluene is formed in equal or higher amounts over large-pore FAU and MOR, suggesting that the additional space in large-pore catalysts facilitates the production of the larger toluene molecule.[2] Remarkably, LTA zeolites with micropores that are too small for dmf to enter, produce exclusively toluene. This hints that pore confinement inside zeolites promotes the formation of benzene, while unconfined conversion on the external acid sites results in the formation of toluene. Based on these initial

2: disregarding more complex effects of the shapes and connectivities of the pores

findings, the framework MFI appears to be the best candidate for the conversion of dmf into aromatics, followed by BEA and FAU.

Table 4.1: Ratios between the amount of formed benzene and toluene over different zeolite frameworks, normalised to the lowest ratio and rounded off.

	FER	MFI	BEA	MOR	FAU	LTA3	LTA4	LTA5
Benz.	1	3	4	1	1	0	0	0
Tol.	0	1	1	2	1	1	1	1

As mentioned in section 2.3.2, the acidity of the catalyst also plays a crucial role besides the microporous framework, which is related to the aluminium content (more Al = more acid sites). Ideally, to isolate the effect of the framework, zeolites are selected with identical silicon-to-aluminium ratios and thus comparable acidities. However, some frameworks are only stable or synthetically possible within a certain range of ratios, which has, next to commercial availability, determined the selection of the studied materials.

The acidity was investigated with NH_3-TPD, resulting in the desorption profiles as shown in figure 4.3. All frameworks contain a desorption peak around 200 °C, belonging to weak acid sites. A second desorption peak is observed in MFI, BEA, and FAU around 310 °C, as well as in FER and MOR at ≥ 420 °C, indicating the presence of a strong and extra-strong acid site, respectively. Although much research has linked these sites to specific Brønsted (BAS) or Lewis acid sites (LAS) for framework and extra-framework[3] aluminium, respectively, one must refrain from hastily assigning NH_3-TPD peaks to specific species without further evidence [138].

The acid site densities were quantified (table 4.2) and vary from 0.364 mmol g^{-1} in FAU to 0.826 mmol g^{-1} in MOR, even though the Si/Al ratios of most zeolites range from 10 to 15. The LTA catalysts possess a high Al content (Si/Al=1) but display relatively low acid site densities of 0.010, 0.352, and 0.504, for LTA3, LTA5, and LTA4, respectively. Possible explanations may be the presence of the cations K^+, Na^+, and Ca^{2+}, replacing the proton of the BAS,[4] or the size-exclusion effect as NH_3, with a kinetic diamter of 3.26 Å [139, 140], is too large to enter pores of 3 Å wide during NH_3 adsorption at 100 °C, underestimating the acid site density of LTA3. Surprisingly, the catalysts with the highest acid site density, FER and MOR, do not exhibit the highest BTX production, even though more acid sites should allow for more reactions to occur per unit time. This could be related to the size of their micropores or by the deactivation of the catalyst, illustrated by the rapid decrease in conversion and S_{BTX} in figure 4.1.

For reference, non-porous metal oxides like silica (SiO_2), alumina (Al_2O_3), and gallium oxide (Ga_2O_3) have been tested (not shown). Alumina and gallium oxide both possess acid sites

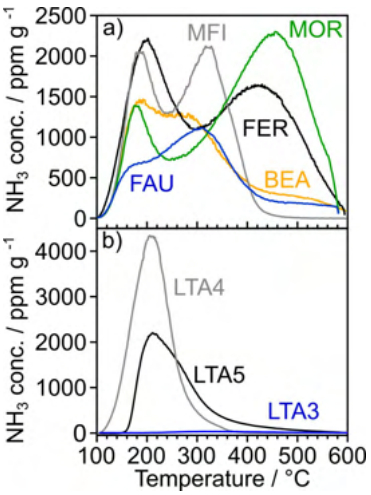

Figure 4.3: NH_3-TPD profiles of different zeolite framework, including FER (black), MFI (grey), BEA (orange), MOR (green), and FAU (blue) in panel a, and LTA3 (blue), LTA4 (grey), and LTA5 (black) in panel b.

Framework	Si/Al	Acidity[a] mmol g^{-1}
FER	10[b]	0.826
MFI	11[c]	0.538
BEA	12[c]	0.444
MOR	10[b]	0.862
FAU	15[b]	0.364
LTA3	1[b]	0.010[d]
LTA4	1[b]	0.504
LTA5	1[b]	0.352

[a] acid site density (number of sites in mmol per gram)
[b] provided by manufacturer
[c] determined with XRF

Table 4.2: Microporous zeolite frameworks, full details in table 3.1.

3: extra-framework = out-of-the framework

4: even though cations can also act as LAS and coordinate to the lone electron pair of NH_3, affecting the size and shape of the NH_3-TPD profile.

but display a low conversion of dmf into CO, CO_2, H_2O, coke, and only a few ppm of toluene, illustrating the necessity of a microporous framework to both steer the selectivity towards BTX and increase the activity of the catalyst. Linking the catalytic performance of the catalysts to their pore sizes, it appears that a tight fit of the pores around the reactant dmf, whose kinetic diameter is 5.7 Å [73], is beneficial for the production of BTX.[5] The microporous MFI structure results in a high quantity of favourable interactions between dmf and active sites, and partially prevents the formation of larger molecules like polycyclic aromatics. Further improvements in the catalytic performance may be obtained by extending the lifetime of the catalysts, potentially by changing the acid site strength to direct the selectivity towards BTX instead of coke.

5: reminder: the porous structure becomes flexible and the pore size expands at high reaction temperatures. They are better described with the Norman radii, e.g., 6.2 and 6.3 Å for MFI [73, 141].

Take-home message
Acidic zeolites with different microporous frameworks can convert dmf into BTX, in which the presence of micropores increases both the activity and selectivity of the catalyst. Medium-pore MFI framework displays the highest catalytic performance, owing to the size compatibility between reactants, products, and the micropores.

4.2 The choice of the substituting metal

This subchapter investigates the influence of the acid site strength, which is dependent on the heteroatom or metal that substitutes silicon in the framework. The rapid deactivation caused by coking may be delayed or prevented if the strength of the acid sites is lowered, steering the selectivity towards monocyclic aromatics.

Aluminium-containing Al-MFI and Al-BEA are compared with gallium-containing Ga-MFI and Ga-BEA. Part of this work regarding the MFI framework is discussed in further detail in paper I [84].

4.2.1 MFI

This section compares purely siliceous Si-MFI (later referred to as G0, known as silicalite-1), Al-MFI(Si/Al=41), and Ga-MFI(Si/Al=33), synthesised hydrothermally [77, 86, 87, 142].

The crystalline structure of the materials was evaluated with XRD and all materials were shown to comprise only the MFI framework (figure S2, paper I) [84, 143, 144]. The elemental compositions were measured with XRF and up to 0.1 and 0.01 wt.% of impurities of potassium and calcium were found in Si-MFI and Ga-MFI, respectively (table S2, paper I). The morphology was studied using SEM and both Si-MFI and Al-MFI comprise well-defined coffin-shaped crystallites, whereas Ga-MFI comprises aggregates of intergrown cubic crystallites (figure S3, paper I).

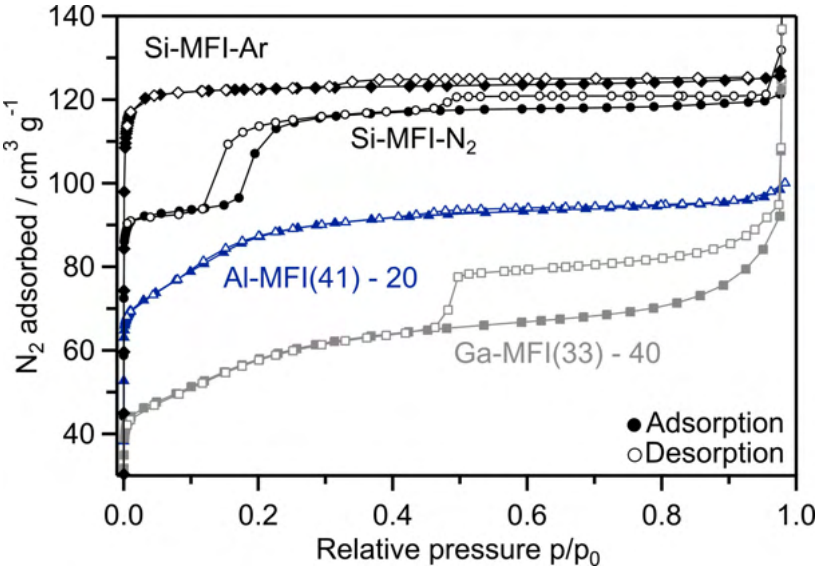

Figure 4.4: Nitrogen physisorption isotherms at 77 K of Si-MFI (black, dots), Al-MFI (blue, squares) and Ga-MFI (grey, triangles). Al-MFI and Ga-MFI are translated vertically for clarity (−20 and −40 $cm^3\,g^{-1}$). Argon physisorption at 77 K has been performed on Si-MFI (black, diamond).

The textural properties of the catalysts were investigated with nitrogen physisorption at 77 K (−196 °C, figure 4.4). The isotherms of Al-MFI (blue, triangles) and Ga-MFI (grey, squares) are translated vertically (−20 and −40 $cm^3\,g^{-1}$), and all isotherms display a

steep increase in nitrogen adsorption at low pressures (not shown), corresponding to the filling of micropores. In addition, Si-MFI (black, dots) and Ga-MFI (grey, squares) display delayed desorption between $p/p_0 = 0.42$–0.98, creating a hysteresis loop caused by capillary condensation in mesopores. These mesopores are considered to be located between particles and crystals or within larger crystal aggregates.[6]

6: SEM confirms this postulation as Ga-MFI(33) possesses the largest intergrown crystal aggregates and the biggest hysteresis loop.

Several artifacts of the use of nitrogen as adsorbate are observed, such as the closure of the hysteresis loops at $p/p_0 = 0.42$, caused by mechanical stability of nitrogen (TSE, [122, 123]), and the additional adsorption step at $p/p_0 = 0.2$ in Si-MFI, caused by the reorganisation of adsorbed nitrogen [83, 124, 145–147]. Therefore, argon physisorption at 77 K was measured (Si-MFI-Ar, black diamonds), in which these phenomena were not observed, confirming that they originate from the use of nitrogen rather than from the structure of the catalyst.[7]

7: Argon physisorption has also been performed on other catalysts such as Ga-MFI (section 4.3), as shown in other work [82], and will not be discussed further in this thesis as it should be performed at 87 K.

Quantification of the apparent surface area (SA) and microporous volume (V_{mic}) (table 1, paper I [84]), shows that incorporation of aluminium results in a slight decrease in SA from 395 to 390 m^2/g and in V_{mic} from 0.175 to 0.164 $cm^3\ g^{-1}$ for Si-MFI and Al-MFI(41), respectively. Substituting with gallium Ga-MFI(33) results in a further loss of SA and V_{mic} to 365 m^2/g and 0.145 $cm^3\ g^{-1}$, respectively.

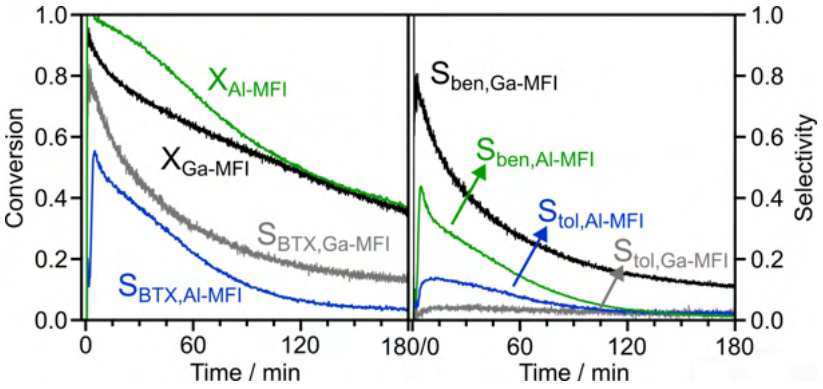

Figure 4.5: Conversion of dmf (X) and selectivity towards BTX (S) over Al-MFI(41) and Ga-MFI(33). Selectivity towards BTX is separated into selectivities towards benzene and toluene (b). Concentrations are measured every 4 (Ga-MFI) or 15 s (Al-MFI).

Initial conversion of dmf (figure 4.5) is 100 % for Al-MFI and 92 % for Ga-MFI, gradually decreasing over time due to the deactivation of the catalyst (figure 4, paper I [84]). Ga-MFI catalyses nearly exclusively the conversion to benzene (benz/tol = 10.1) while Al-MFI produces more toluene (benz/tol = 2.3), likely caused by beneficial steric effects originating from the larger gallium atoms.[8] Even though the gallium-substituted catalyst still suffers from deactivation, its initial and long-term activity show an improvement in catalytic performance with respect to the Al-MFI catalyst.

8: Both framework and extra-framework Ga lower the effective pore diameter.

The reaction of Ga-MFI(33) is analysed further in figure 4.6 (a), displaying the selectivities towards the main products (b). The formation of indene, a precursor to coke, hints at the continued aromatisation of BTX into polycyclic aromatics that are too large to

exit the microporous structure. After 70 min, the selectivity shifts towards isomerisation products, such as 2,4-dimethylfuran (dmf, blue), 2-methyl-2-cyclopentenone (2-mcpo, green), and 3-methyl-2-cyclopentenone (3-mcpo, teal).[9]

9: The catalyst was stable for 4 more cycles of 2 h at 500 °C, displaying a minor loss in X_{dmf} and $S_{benzene}$ due to a loss of acid sites (figure S10, paper I [84]).

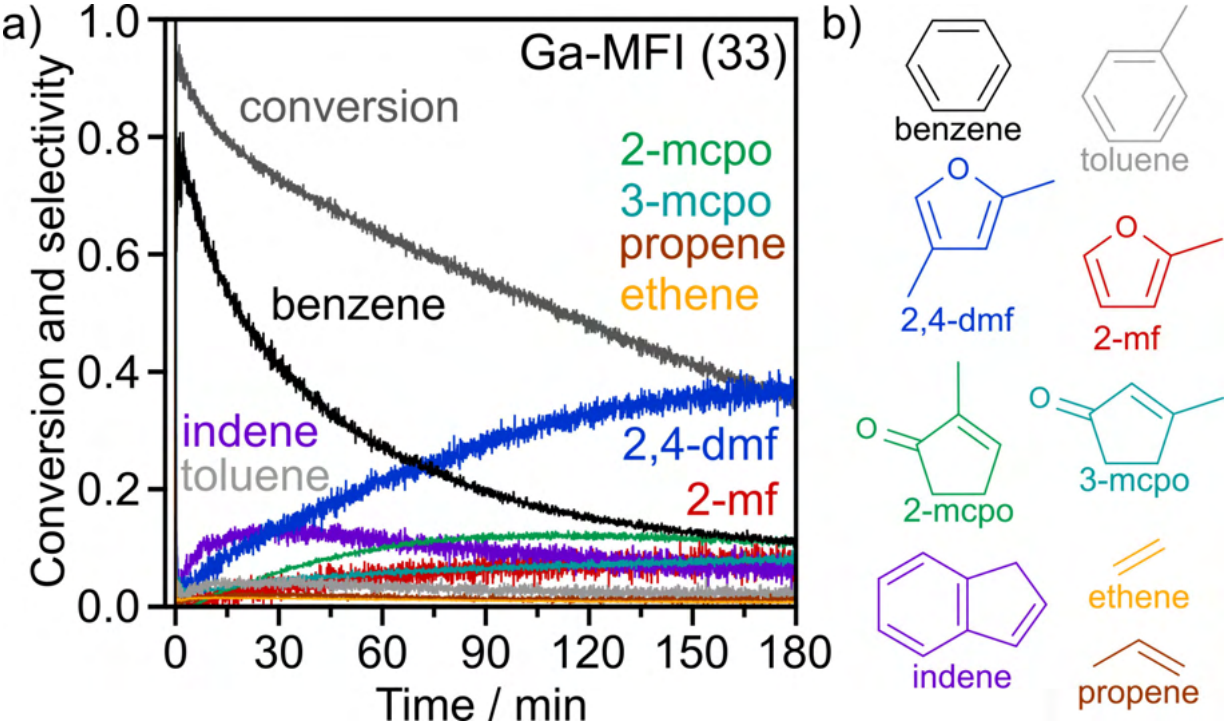

Figure 4.6: Conversion of dmf and selectivity (a) of the main products (b) over Ga-MFI(33) during the first 3 h of a 10 h reaction at 500 °C.

To investigate the origin of the observed change in selectivity, the availability of the acid sites was studied by measuring NH_3-TPD before the reaction, on the fresh catalyst, and directly afterwards, on the coked catalyst (figure 4.7).

Si-MFI possesses almost no acid sites, while Al-MFI(41) and Ga-MFI(33) both possess a weak site, of which ammonia desorbs at 175 °C, and a strong site around 315 °C. Additionally, a medium acid site at 215 °C and a broad shoulder of extra-strong sites is observed at 450 °C, both more prominent in Ga-MFI(33). In another work, DRIFTS was used to determine that the Al-OH BAS is stronger than the Ga-OH BAS [86, 87]. As the desorption temperature of the strong site is higher for Al-MFI (330 °C) than that of Ga-MFI (300 °C), connecting these observations leads to the hypothesis that this strong site is of Brønsted acid character.

After the catalytic reaction (black and blue, dots), many acid sites have become unavailable due to the formation of coke, blocking access to sites.[10] Primarily, the strong and extra strong sites were affected, losing 90 % and 100% of the initial sites, while only 50% of the weak and medium acid sites were lost. Linking this to the catalytic activity, it follows that the production of BTX, which was nearly non-existent at the end of the reaction, happens

10: Over 90 % of the acid sites can be regenerated in 20 % O_2 at T≥ 600 °C, confirming the blockage by coke.

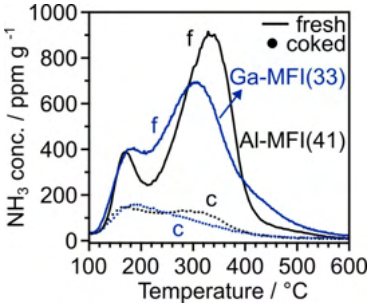

Figure 4.7: NH_3-TPD profiles of Al-MFI(41) (black) and Ga-MFI(33) (blue) in their fresh states and coked states (dots).

on strong and extra-strong sites. Similarly, isomerisation reactions like the formation of 2,4-dmf, still take place after 10 h TOS with 30 % selectivity at 10 % conversion (figure 4, paper I), signalling that they occur on weak acid sites [84].

Identifying the nature and location of the gallium sites is pertinent to understand the reaction mechanism. In another work, the extra-strong acid site was ascribed to extra-framework gallium that is located in the ion-exchange position [148]. This site, also referred to as framework-associated Ga, synergistically interacts with framework gallium,[11] resulting in its high strength.[12] In this work, the sites will be discussed in more detail in section 4.3.

Isomorphous substitution of Si^{4+} by bigger cations, La^{3+} (117 pm[13]) and In^{3+}(76 pm), was mostly unsuccessful, yielding a low surface area of 203 m^2/g for La-MFI(120), a low acid site density of 0.023 mmol g^{-1} for In-MFI(70), and consequently resulting in a low conversion and selectivity to BTX over either catalysts .

11: this means that it interacts in a way that the combined effect, either in acid site strength, function, or activity, is greater than the sum of the individual effects:they display synergy

12: the site was determined to be a LAS and framework Ga was required for its formation.

13: octahedral coordination, La^{3+} is too large to assume a tetrahedral position

Take-home message
Aromatisation of dmf to BTX and coke occurs on strong and extra-strong acid sites. Gallium introduces promoting steric effects in Ga-MFI, due to its size and its presence as extra-framework species, forming extra-strong acid sites that promote aromatisation. After deactivation to aromatics, isomerisation products such as 2,4-dmf become the main product, formed on weak acid sites.

4.2.2 BEA

The effect of substituting Al by Ga has also been explored in BEA framework catalysts with commercial Al-BEA(12), hydrothermally synthesised Ga-BEA(13), and Ga-deAlBEA(12) and P-BEA obtained through impregnation of dealuminated Al-BEA(12).[14]

The crystallinity is preserved after dealumination, as shown by XRD in figure 4.8 (a, purple). For reference, a simulated XRD pattern of BEA intergrowth nr. 73 (red sticks) is shown, which comprises of 30 % polymorph BEA A, 30 % polymorph BEA B, and 40 % polymorph BEA CH [65].[15] After gallium (grey) or phosphor (green) impregnation, no peak shift is observed at this resolution, indicating that framework substitution did not affect the unit cell dimensions or that they are present as extra-framework species instead.[16]

Their textural properties have been investigated with nitrogen physisorption (figure 4.8, b) and all isotherms closely overlap, as shown in the inset. They are composites of type I and IV, corresponding to micro- and mesoporous materials, respectively [104]. The small hysteresis loop at high pressures (type H4) was observed

14: Dealumination nearly removed all aluminium, from Si/Al=12 to Si/Al=1309.

15: reminder: the zeolite family Beta/BEA has a 1-dimensional stacking disorder and always exists as intergrowth of two or three polymorphs, which have never been observed individually as pure materials.

16: Differences in relative peak intensities are caused by the use of slightly different experimental settings [82].

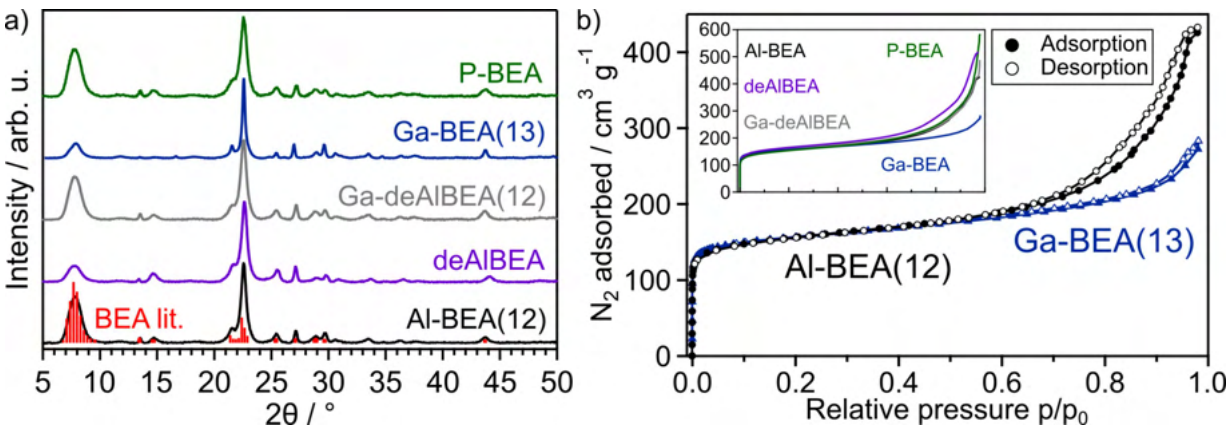

Figure 4.8: XRD (a) of Al-BEA(12), Ga-deAlBEA(12), Ga-BEA(13), P-BEA, and reference BEA (red sticks). Nitrogen physisorption isotherms (b) of Al-BEA(12) (black dots) and Ga-BEA(13) (blue triangles), with adsorption isotherms of deAl-BEA(1309) (purple), Ga-deAlBEA(12) (grey), and P-BEA (green) in the inset.

for all catalysts and is caused by capillary condensation, indicating the presence of mesopores between aggregated crystals of zeolite. Quantification of the SA, S_{ext}, and V_{mic} (table 4.3) reveals that all catalysts have a large SA of around 600 m^2/g and a mesoporous area of 200 m^2/g, likely caused by the stacking disorder.

Sample	M wt.%	SA $m^2\,g^{-1}$	S_{ext} $m^2\,g^{-1}$	V_{mic} $cm^3\,g^{-1}$
AlBEA(12)	12	586	191	0.158
deAlBEA(1308)	0.03	617	213	0.162
Ga-deAlBEA(12)	7.7	602	197	0.162
GaBEA(13)	7.8	603	153	0.189

Table 4.3: Physicochemical properties of Ga-BEA and and Al-BEA.

The catalytic performance has been evaluated (figure 4.9) and the conversion decreases in the order Al-BEA(12) > Ga-BEA(13) > Ga-deAlBEA(12), while the initial selectivity towards benzene increases by substituting gallium. Quantification of the total production (table 4.4) shows that gallium impregnation (Ga-deAlBEA(12)) resulted in a slight decrease in the production of benzene and an increase in the production of toluene, compared to Al-BEA(12). Ga-BEA(13) displays a nearly twofold increase in the production of both benzene and toluene, demonstrating that the positive effect of gallium is not only valid in MFI framework catalysts.[17]

The acid sites have been evaluated with NH_3-TPD (figure 4.10) and quantified (table 4.4), revealing that the acid site densities of Al-BEA(12) (black, 0.444 mmol g^{-1}) and Ga-BEA(13) (blue, 0.404 mmol g^{-1}) are relatively similar. This confirms that the enhanced performance of Ga-BEA(13) is caused by gallium and the type of acid sites it provides, instead of the abundance of sites. Ga-BEA(13) possesses an additional extra-strong acid site (peak at 425 °C), similar to what was seen in Ga-MFI(33), which may originate from framework-associated gallium and be responsible for the

17: Initial evaluation of P-BEA(Si/P≈27) displays a significantly lower production of BTX, with 0.022 mmol g^{-1} toluene produced in 1 h. Further acid site analysis to confirm the extent of phosphor impregnation is necessary.

increased production of aromatics. Even though Ga-deAlBEA(12) produces roughly the same amount of aromatics as Al-BEA(12), the fact that is possesses roughly half of the acid site density of Al-BEA(12), with 0.253 mmol g^{-1}, indicates that each of its acid sites is significantly more active. As it has a similar metal content as the other catalysts, its low acid site density confirms the presence of non-acidic extra-framework gallium species.

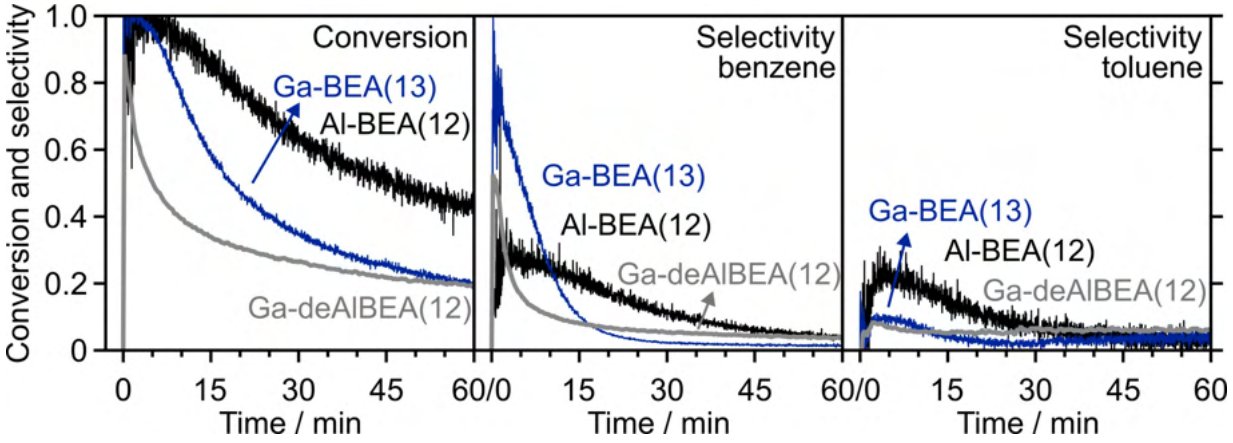

Figure 4.9: Conversion and product selectivities over Al-BEA(12) (black), Ga-BEA(13) (blue), and Ga-deAlBEA(12) (grey). Concentrations are measured every 2 s for Al-BEA(12 and Ga-BEA(13)) or 15 s for Ga-deAlBEA(12).

18: Coke is quantified based on CO and CO_2 detected during a regeneration step after the reaction in 20% O_2 at 600 °C.

19: The low initial acid site density of Ga-deAlBEA(13) also decreases its lifetime.

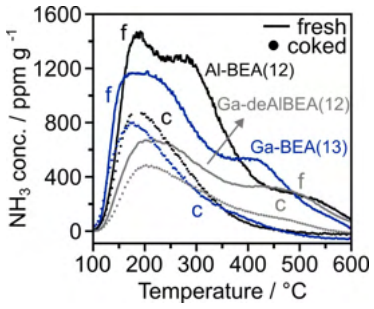

Figure 4.10: NH_3-TPD profiles of Al-BEA(12) (black), Ga-BEA(13) (blue), and Ga-deAlBEA(12) (grey) in their fresh states and coked states (dots). For clarity, every 2nd point is shown for coked Ga-deAlBEA(12) and every 10th point for coked Al-BEA(12) and coked Ga-BEA(13).

Quantification of the produced coke[18] shows that Al-BEA(12) exhibits the highest selectivity to coke (34.9 %), hinting that gallium may reduce the formation of coke. However, this does not directly correlate to a longer lifetime, as both Ga-BEA catalysts deactivate more rapidly in terms of conversion and $S_{benzene}$. Extra-framework gallium likely accelerates the initial formation of coke inside the pores, by restricting the diffusion and mass transport of products, coke precursors, and coke species.[19] The introduction of gallium appears to be a double-edged sword, both increasing the production of BTX and decreasing the lifetime of the catalyst.

Evaluation of the acid sites of the coked catalysts (figure 4.10, dots) reveals that the strong and extra-strong acid sites have primarily been coked, parallel to what was observed for MFI catalysts. Ga-deAlBEA(12) still possesses some strong and extra-strong acid sites after the reaction of 3 h, which explains why benzene and toluene are still produced after 1 h TOS. Gallium impregnation likely results in a high fraction of gallium on the external surface of the zeotype or in the pores close to the outer surface of crystals, instead of deeper inside the micropores. Consequently, diffusion of coke precursors may be facilitated at these sites, as opposed to less-accessible sites inside the micropores, leading to a constant production of toluene on external sites after initial deactivation of the other sites. The nature of these sites may be elucidated with pyridine DRIFTS (BAS vs. LAS) or with larger molecules like 2,4,6-trimethylpyridine and 2,6-di-*tert*-butylpyridine, which

cannot enter the micropores and only bind to the external acid sites [149–151]. This demonstrates the influence of the synthesis methods on the location of gallium, the acid sites, and the catalytic performance.

Sample	Acidity mmol g^{-1}	Benz.3 h mmol g^{-1}	Tol.3 h mmol g^{-1}	S_{coke} %
AlBEA(12)	0.444	0.180	0.108	35
Ga-deAlBEA(12)	0.253	0.166	0.164	29
GaBEA(13)	0.404	0.334	0.254	31

Table 4.4: Acid site densities and catalytic performance of Ga-BEA and Al-BEA.

Comparison of the microporous frameworks MFI with BEA shows that the production of benzene is significantly favoured over the smaller pores of MFI, while BEA does not discriminate to the same extent between benzene and toluene. Additionally, after deactivation towards benzene and toluene, the selectivity shifts towards 2- and 3-mcpo in BEA instead of to 2,4-dmf. This reveals the mechanistic insight that the MFI framework promotes the isomerisation of dmf into 2,4-dmf. Furthermore, Al-BEA(12) favours the production of 3-mcpo while Ga-BEA(13) that of the larger 2-mcpo molecule, even though Ga-BEA(13) favours the smaller benzene molecule. This hints at the complex relationship between catalytic descriptors and the mechanism of the reaction, suggesting that the pathway to the isomerisation products is different than the pathway to aromatics.

Now that the choice of the substituted metal and its effect on the acid sites and the reaction has been explored, the next step is to vary the metal content and acid sites to optimise its activity and selectivity.

Take-home message

The production of aromatics can be enhanced by introducing gallium in both the MFI and BEA framework. While the MFI framework significantly favours the production of benzene, toluene is roughly produced in equal parts over BEA catalysts, likely caused by BEA's larger micropores and the presence of mesopores.

4.3 The influence of the metal content

This chapter elaborates on the effect of the acidity by investigating the influence of varying the metal content. First, the effect of varying the aluminium content in Al-MFI, Al-BEA, and Al-FAU will be discussed. Then, a series of gallium-impregnated Al-BEA, Al-FAU, and Al-MOR is described, after which a series of Ga-MFI with varying gallium content is discussed (paper II [83]).

4.3.1 Al-MFI, Al-BEA, and Al-FAU

The catalytic performance of Al-MFI(11) (section 4.1) and Al-MFI(41) (section 4.2) is compared in figure 4.11. While Al-MFI(11) displays a slightly higher selectivity to toluene and benzene than Al-MFI(41), the latter deactivates more slowly and still produces 2,4-dmf after 3 h TOS (not shown). Quantification of the produced aromatics (table 4.5) shows that 0.497 mmol g^{-1} benzene and 0.219 mmol g^{-1} toluene are produced over Al-MFI(41), while Al-MFI(11) produces roughly double with 0.889 mmol g^{-1} benzene and 0.339 mmol g^{-1} toluene. This can be ascribed to the higher acid site density of Al-MFI(11) of 0.538 mmol g^{-1}, over three times that of Al-MFI(41) with 0.175 mmol g^{-1}.[20] This demonstrates that the catalytic performance can be improved by increasing the metal content, and consequently, the acid site density of the catalyst. As a result of the high acid site density of Al-MFI(11), it has deactivated more rapidly than Al-MFI(41), resulting in a total production of aromatics which is twice as high, even though it possesses three times as many acid sites.

20: which follows from the difference in Al content, 3.5 and 1.0 wt.% for Al-MFI(11) and Al-MFI(41), respectively

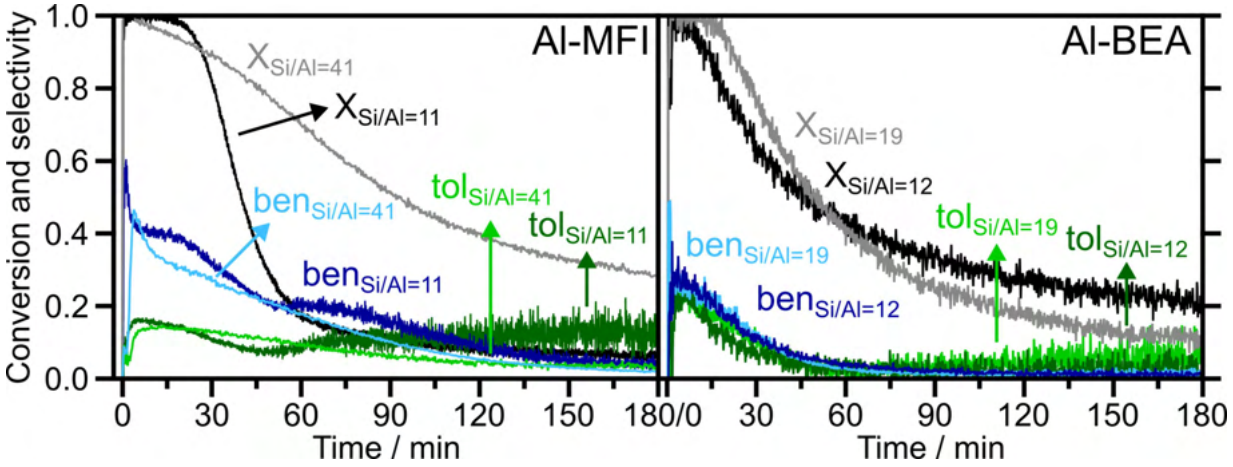

Figure 4.11: Conversion and product selectivities over Al-MFI(11), Al-MFI(41), Al-BEA(12), and Al-BEA(19).

Evaluating the NH_3-TPD of the coked catalyst (figure 4.12, blue dots), shows that Al-MFI(11) has only lost a small fraction of its acid sites (33 %, table 3, paper I) and still possesses strong acid sites, even though it has become nearly completely inactive. By contrast, Al-MFI(41), which has also become inactive for the production of aromatics, has lost 89 % of its total acid site density and nearly all of its strong sites (figure 4.7). This suggests that the coke species formed on Al-MFI(11) have completely enveloped particles and crystals, restricting the access to the micropores by dmf while allowing the smaller ammonia molecules to probe the acid sites during NH_3-TPD. As a consequence of the rapid coking of Al-MFI(11), each of its acid sites has produced 2.28 BTX molecules in 3 h TOS on average, while each acid site of Al-MFI(41) has produced 4.14 BTX molecules. Besides normalising to the number of acid sites, the production can also be normalised to the number of substituted metal atoms, which will be discussed for Ga-MFI catalysts.[21]

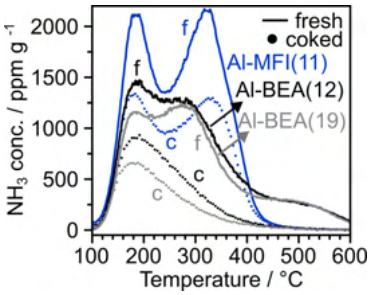

Figure 4.12: NH_3-TPD of Al-MFI and Al-BEA in the fresh (f, full) or coked state (c, dots). For the coked state, every 7th (Al-MFI(11)) or 15th point (Al-BEA(12) and Al-BEA(19)) is shown for clarity.

Next to studying MFI, the aluminium content has also been varied in BEA framework catalysts, comparing Al-BEA(12) (sections 4.1 and 4.2) to Al-BEA(19); a zeolite with a lower aluminium content (3.2 vs. 2.3 wt.%). The conversion of dmf (figure 4.11) and the selectivity to benzene and toluene displays a similar behaviour, although quantification shows that Al-BEA(19) produces more benzene, 0.231 vs.0.180 mmol g^{-1}, and more toluene, 0.202 vs. 0.108 mmol g^{-1}, than Al-BEA(12). The distribution of their acid sites is similar, both containing weak, strong, and extra-strong sites (figure 4.12), amounting to an acid site density of 0.388 and 0.444 mmol g^{-1} for Al-BEA(19) and Al-BEA(12), respectively. Remarkably, these results demonstrate that an increase in metal content and acidity does not always lead to an increase in the catalytic performance. Possible explanations may be the accelerated coking in Al-BEA(12) caused by its higher acid site density, although the difference is much smaller than in Al-MFI. Instead, it may be caused by non-acidic extra-framework aluminium, e.g., as clusters or nanoparticles, that inhibitsthe transport of molecules while not promoting S_{BTX}. This is supported by the fact that Al-BEA(12) contains 1.6 as much aluminium as Al-BEA(19) and only 1.1 as many acid sites.[22]

A series of Al-FAU with varying Al-content has been tested (figure 4.13) and similar trends can be observed as in MFI: an increase in aluminium content results in an increase in acid site density and BTX production, with the exception of Al-FAU(2.6). Remarkably, Al-FAU(2.6) contains fewer acid sites than catalysts with less aluminium, like Al-FAU(6.1), and possesses less than half of the surface area and microporous volume (NH_3-TPD profiles not shown). This introduces and demonstrates the importance of the

21: a high atom utilisation is an important property to optimise, adhering to the green chemistry principles, especially when designing catalysts with scarce noble metals.

22: besides non-acidic metallic or metal oxide clusters, the relatively low acid site density can also be derived from Lewis acids in which multiple Al atoms or ions contribute to only one acid site.

Table 4.5: Physicochemical properties and catalytic performance of Al-MFI, Al-BEA, and Al-FAU.

Sample	SA[a] $m^2\,g^{-1}$	S_{ext}[b] $m^2\,g^{-1}$	V_{mic}[b] $cm^3\,g^{-1}$	Acidity[c] $mmol\,g^{-1}$	Benz.3 h $mmol\,g^{-1}$	Tol.3 h $mmol\,g^{-1}$	BTX/ acid	S_{coke} %
Al-MFI(11)	412	26	0.158	0.538	0.889	0.339	2.28	15
Al-BEA(19)	N.A.[d]	N.A.	N.A.	0.388	0.231	0.202	1.11	32
Al-FAU(2.6)	306	27	0.105	0.297	0.012	0.038	0.17	22
Al-FAU(6.1)	703	123	0.222	0.471	0.093	0.169	0.56	33
Al-FAU(15)[e]	896	207	0.268	0.364	0.086	0.090	0.48	31
Al-FAU (30)	816	75	0.306	0.189	0.043	0.092	0.72	19
deAl-FAU(39)[e]	887	210	0.263	0.030	0.006	0.015	0.69	10

[a] Apparent surface areas by BET method, p/p_0 = 0.002–0.03 following consistency criteria [112]
[b] By t-plot method[116] (Harkins and Jura equation, t= 5.0–8.0 Å)
[c] Acid site density from NH_3-TPD
[d] N.A.=Not available
[e] Reaction was stopped after 70 and 135 min for Al-FAU(15) and deAl-FAU(39), respectively.

23: adsorbed in the micropores from the air or formed in the reaction

stability of the catalyst, another catalytic descriptor. Due to its high aluminium content, it is less hydrothermally stable, especially when water is present.[23] The low surface area suggests that the catalyst possesses a higher fraction of amorphous material, which was supported by a low signal-to-noise ratio in XRD (not shown) For FAU zeolites in particular, common strategies to improve its stability is through dealumination by exposure to steam at high temperatures, producing ultrastable zeolite Y [152]. Another strategy involves dealumination with acids, like diluted HNO_3, which was employed here to dealuminate Al-FAU(6.1) into deAl-FAU(Si/Al=39). Even though this zeolite has a comparable Al content to that of Al-FAU(30), its acid site density of 0.030 $mmol\,g^{-1}$ is much lower than 0.189 $mmol\,g^{-1}$. An explanation is the acid-induced migration of framework Al to extra-framework positions, which subsequently agglomerate and form non-acidic species. Even though each of the remaining acid sites are relatively active, the total production of BTX is significantly reduced.

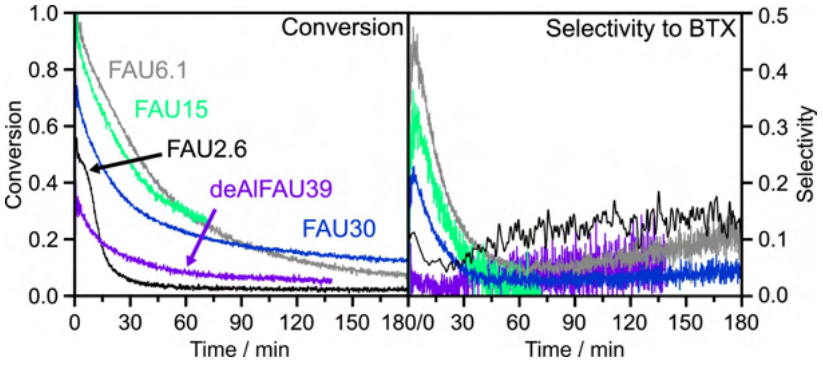

Figure 4.13: Conversion and selectivity to BTX over Al-FAU zeolites. The reaction was stopped after 70 and 135 min TOS for Al-FAU(15) and deAl-FAU(39), respectively, due to an unstable dmf feed.

Take-home message
An increase in Al content corresponds to an increase in acid site density and catalytic performance for MFI and FAU framework zeolites. However, once a framework-specific threshold is reached, a further increase in Al content and acid site density results in excessive coking and deactivation (MFI and BEA) or destabilisation (FAU) of the catalyst.

4.3.2 Ga/Al-BEA, Ga/Al-FAU, and Ga/Al-MOR

Besides impregnation with gallium of deAl-BEA, other zeolites were also impregnated without being dealuminated first, resulting in catalysts with both aluminium and gallium (table 3.2). The effect and degree of impregnation depends on the impregnation procedure, and the metal content, surface area, and framework of the parent material. To illustrate, Ga/Al-FAU(6.1) and Ga/Al-MOR(10) were prepared according to an identical procedure and yet, they possess different silicon-to-gallium ratios of 26 and 46, respectively. The catalysts with both Al and Ga are relevant for two research questions at the same time: the choice of the metal and its content. Moreover, the potential synergistic interaction between gallium and aluminium introduces a new factor. With the presence of two different metals, interpretation of structural and catalytic data becomes more challenging and requires further investigation.[24] However, the following general trends were observed for gallium-impregnated Al-zeolites:

- Gallium impregnation reduces the surface area and microporous volume due to extra-framework species, although framework incorporation has also likely taken place [153].
- Gallium impregnation may result in an increase in the acidity site density, expressed as an increase in weak acid sites, observed in FAU and MOR. However, the acid site density of Ga/Al-BEA was similar or lower than Al-BEA, suggesting that existing acid sites may be obstructed or altered, gallium substitutes framework aluminium, or that gallium is present as non-acidic extra-framework species.
- Initial production of aromatics is reduced by gallium impregnation but long term activity and selectivity is enhanced, displaying a positive effect of gallium on the lifetime of the catalyst. [25]

To briefly illustrate the effect of gallium impregnation of Al-MOR(10), the conversion, product selectivities, and NH_3-TPD profiles of Ga/Al-MOR(10) are shown in figure 4.14. Besides displaying an improved initial conversion and selectivity to benzene,

24: conversion and selecitvity data has thus been omitted from this thesis

25: The acid site density and production of aromatics may be underestimated for Ga/Al-zeolites, as these are normalised to mass instead of atoms or unit cells. After gallium impregnation, the weight of each unit cell is slightly increased, artificially lowering the determined values.

the selectivity to toluene of Ga/Al-MOR(10) increases with increasing TOS. In fact, the selectivity remains stable at 19 % with a conversion of 12 % during 8 h TOS (not shown). The coked catalysts still possess most of their acid sites, suggesting that the rapid deactivation has obstructed the access of dmf to the acid sites in the micropores, on par with what was observed for Al-MFI(11). Therefore, the conversion of dmf into toluene appears to be catalysed by acid sites located on the external surface or inside the micropores but close to the surface of the particles. Future investigation of gallium impregnation on MOR zeolites with lower acid site densities is promising, potentially enabling long-term production of BTX both in- and outside of the pores.

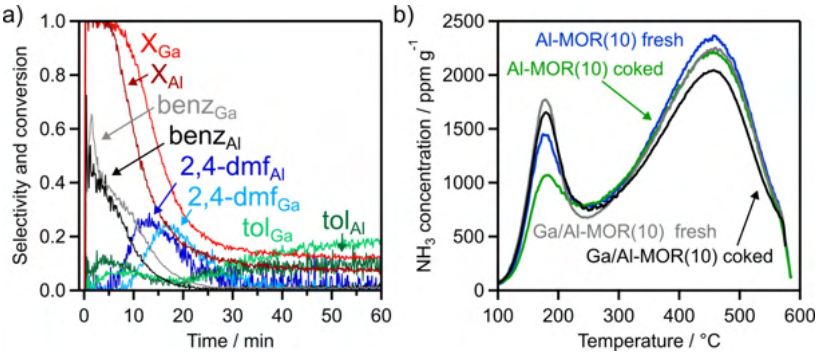

Figure 4.14: Conversion and product selectivities (a) of Al-MOR(10) and Ga(46)/Al-MOR(10). NH_3-TPD profiles (b) for the fresh and coked catalysts.

Take-home message
Gallium impregnation of Al-zeolites improves the catalytic performance, although the synergistic role between Ga and Al is not yet fully grasped. While benzene is principally formed inside the micropores, toluene can also be formed on the external surface.

4.3.3 Ga-MFI

To further investigate the enhanced catalytic performance of gallium-substituted catalysts, a series of Ga-MFI zeotypes with a varying gallium content has been synthesised and evaluated, as described in detail in paper II [83]. For clarity, the nomenclature of this class follows that of paper II, with the gallium content expressed in weight percent.[26]

To successfully synthesise phase-pure zeotypes with a high gallium content (>3.1 wt.%), the synthesis protocol has been refined over time, either through extending the crystallisation step from 5 to 10 days (G6.0) or by replacing the template from TPABr to TPAOH (G6.7, G8.6, and G11).[27] Up to 0.7 wt.% potassium impurity was detected with XRF, likely originating from a KOH bath used to clean the Teflon liners used in hydrothermal synthesis,

26: e.g., G3.1 is Ga-MFI(Si/Ga=34) with 3.1 wt.% Ga

27: 5 days with TPABr and Ga>3.1 wt.% resulted in a partially amorphous zeotype, while 10 days with Ga>6.0 wt.% resulted in the formation of other phases besides MFI, including gallium albite and α-quartz [83, 154, 155].

The presence of the MFI framework is confirmed by using XRD (figure 4.15, a) and increasing the Ga content results in peak broadening and overlap, caused by lattice distortions that originate from structural defects [102].[28]

The textural properties have been investigated with nitrogen physisorption (figure 4.15, b) and all isotherms are composites of type I and IV, associated with micro- and mesoporous materials, respectively. The amount of nitrogen adsorbed in the micropores decreases upon increasing the gallium content, corresponding to a decrease in SA and V_{mic} (table 4.7).The hysteresis loop from p/p_0=0.42–0.98 of type H4 is caused by capillary condensation in mesopores, located between crystallites or in larger aggregates of zeotype crystals. Both G0 (Si-MFI) and G0.5 contain a second adsorption and hysteresis at p/p_0=0.1–0.25, caused by the reorganisation of adsorbed nitrogen rather than a feature of the porous structure [83, 124, 145–147].

The PSD of the micro- and mesoporous regions is shown in figure 4.16, unveiling the presence of micropores with different pore widths. Although approaching instrumental limits, several diffferent pore sizes are observed in G6.7 at 5.22 and 5.33 Å, likely corresponding to the sinusoidal and straight channels of the MFI framework, respectively.[29] Although speculative, G1.2, G3.1, and G6.7 appear to possess more than two pores, suggesting either expansion of some pores due to the incorporation of gallium in the framework, or an effective pore width reduction due to the presence of extra-framework gallium.[30] The mesopore size distribution reveals that most zeotypes possess a broad range of different sizes of mesopores, confirming their nature as intercrystalline mesopores. No apparent effect of the gallium content can be discerned and the PSD of G0 and G0.5 are flawed due to the additional adsorption step p/p_0=0.1–0.25, falsely resulting in a sharp derivative of the pore volume.[31]

28: Peaks at 23.2°and 23.4°(G0 and G0.5) merge into one at 23.3°, as well as peaks at 24.4°and 24.6°(G0, G0.5, and G1.2) into one at 24.5°.

29: widths < 5.2 Å describe individual and layer-by-layer adsorption of N_2, appearing as a peak in the derivative but not associated with a certain pore.

30: The equilibrium pressure in G1.2 may not have been reached due to the high data collection rate, resulting in erroneous peak generation.

31: which is corrected for manually

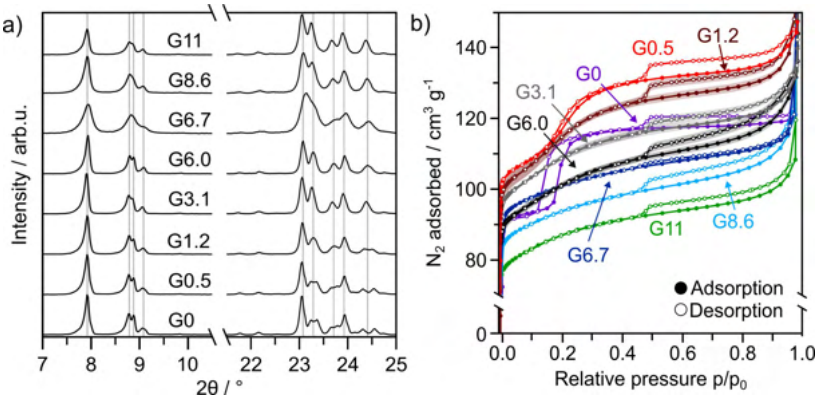

Figure 4.15: Close-up of the XRD diffractograms (a) of Ga-MFI showing the regions of interest, in which the vertical gray lines indicate the most intense peaks of the MFI-structure [143]. Nitrogen physisorption (b) in which micropore filling at low pressures is omitted. G1.2, G3.1, G6.0, and G6.7, were measured twice and the average value is shown, as well as the variance indicated by the shaded area.

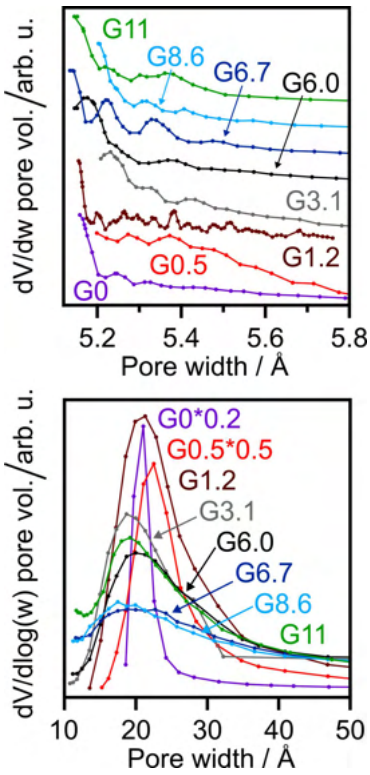

Figure 4.16: PSD of Ga-MFI determined with nitrogen physisorption, using the Horvath-Kawazoe model (cylindrical pores, Cheng-Yang correction) for micropores (top panel) and the BJH-model (adsorption curve, Harkins and Jura thickness curve) for mesopores (bottom panel). The derivative of the pore volume of G0 is multiplied by a factor of 0.2 and that of G0.5 by a factor of 0.5.

The morphological features of Ga-MFI catalysts have been explored with SEM, as shown in figure 4.17 and in paper II, figures 1 and S5. G0 crystals possess the well-know coffin-shape of two parallelepipeds embedded in one another, often observed for MFI zeolites. After the introduction of gallium, smaller cubic-shaped crystals are formed for zeotypes G0.5, G1.2, and G3.1, which combine and form larger crystal aggregates. This explains the presence of the hysteresis observed with nitrogen physisorption, originating from mesopores in these crystal aggregates. The high gallium content catalysts, G6.7, G8.6, and G11, comprise intergrowths of well-defined crystallites of different sizes and shapes, while G6.7 comprises large intergrowths of smaller spherical crystallites, typically ranging from 500 nm to 1 µm, explaining the broad peaks observed in XRD.

The broad variety in the size and shapes of crystals, even within the same catalyst, may be an indication that gallium is not homogeneously dispersed throughout the material. Therefore, the elemental distributions of G3.1 [82], G8.6 [83], and G11 (figure 4.18) have been determined with SEM-EDX. The main components, silicon (blue), oxygen (green), and gallium (red), are detected and gallium appears to be well-dispersed throughout the large crystal aggregate. Point spectra were recorded at different positions of the crystal, denoted by the yellow numbered dots, and their compositions were determined (table 4.6). The gallium content spans a broad range across the different points, averaging around 7 wt.%, while the bulk gallium content determined with XRF of G11 was 10.7 wt.%. As EDX is more surface sensitive than XRF, this indicates that gallium is primarily situated inside the crystals as opposed to on its surface. Another possible explanation would be that gallium is grouped or agglomerated in certain locations, which are not probed by the SEM image of this particular particle. To further investigate and homogenise the composition of the catalyst, another Ga-MFI(Ga≈8.6 wt.%) zeotype was prepared in which the reaction mixture was agitated during crystallisation via the use of a rotating oven (RO) instead of a static oven (SO), which will be discussed in detail in section 4.5.4.

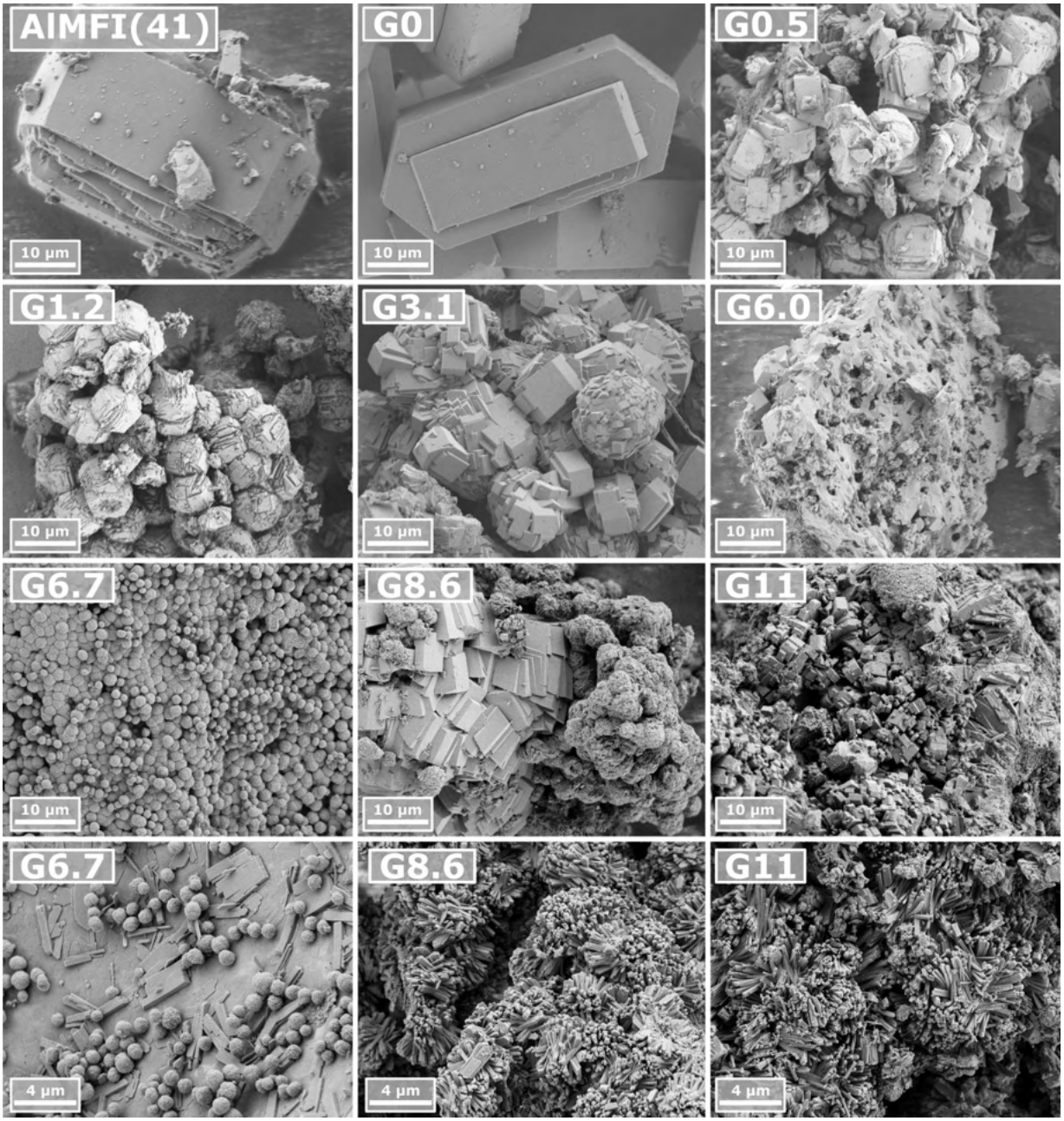

Figure 4.17: SEM images of Ga-MFI, recorded at an accelerating voltage of 1 kV (G0.5, G1.2, and G3.1) or 1.5 kV. Al-MFI(Si/Al=41) is shown as reference and a close-up of G6.7, G8.6, and G11 is shown in the bottom row. Catalysts were measured uncoated, coated with 2.7 nm gold (G6.7, G8.6, G11), or coated with 4 nm gold (G0.5, G1.2, G3.1) to reduce charging effects.

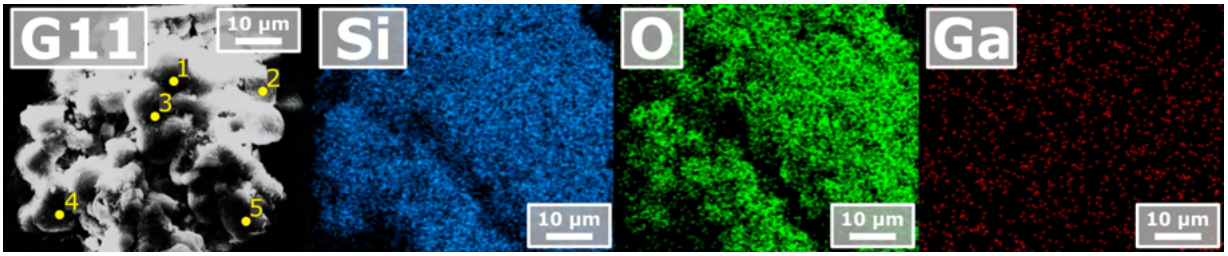

Figure 4.18: SEM image of H-G11 (left panel) recorded at 20 kV and EDX maps displaying the dispersion of silicon (blue), oxygen (green), and gallium (red). Brightness is altered (+40 %) for all elements for clarity.

Spec.	Ga	Si/Ga
1	5.1	20
2	4.9	19
3	5.8	10
4	11.6	10
5	6.8	16
bulk[a]	10.7	8.2

Table 4.6: Elemental compositions of point spectra on H-G11 (figure 4.18), derived from EDX.

To elucidate the position and identity of the gallium species, TEM and HAADF-STEM were performed on Ga-MFI zeotypes with a high gallium content of ≥6.0 wt.% (figure 4.19). This technique reveals the presence of gallium-based nanoparticles, possibly gallium oxides, ranging from 1 to 5 nm in diameter. These are visualised as bright spots since heavy elements like gallium scatter electrons more strongly than silicon or oxygen. There presence confirms the existence of extra-framework gallium, explaining the heterogeneity in elemental composition observed by EDX. The nature of these nanoparticles is further explored by HAADF-STEM/EDX for Ga-MFI$_{meso}$ catalysts, described in section 4.4.1.

Table 4.7: Physicochemical properties of Ga-MFI, derived from nitrogen physisorption, NH_3-TPD (acid site densities), and pyridine DRIFTS. Experiments were repeated once and the average values are shown as well as the variance.

Sample	Si/Ga	SA[a] $m^2\,g^{-1}$	S_{ext}[b] $m^2\,g^{-1}$	V_{mic}[b] $cm^3\,g^{-1}$	Acidity $mmol\,g^{-1}$	BAS/LAS[c]
G0	∞	395	9	0.175	0.002	∞
G0.5	238	445	27	0.185	0.039	∞
G1.2	95	435 ± 1	31 ± 1	0.175 ± 0.001	0.119	3.3
G3.1	34	420 ± 1	28 ± 2	0.162 ± 0.003	0.268	3.0
G6.0	17	390 ± 4	43±11	0.142 ± 0.005	0.256	1.3
G6.7	15	401 ± 1	27 ± 1	0.148 ± 0.001	0.423	2.1
G8.6	11	368	30	0.135	0.433	1.8
G11	8	336	25	0.127	0.612	3.8

[a] Apparent surface areas by BET method, p/p_0 = 0.002–0.03 following consistency criteria [112]
[b] By t-plot method[116] (Harkins and Jura equation, t= 5.0–8.0 Å)
[c] Ratio of Brønsted to Lewis acid sites from pyridine-DRIFTS

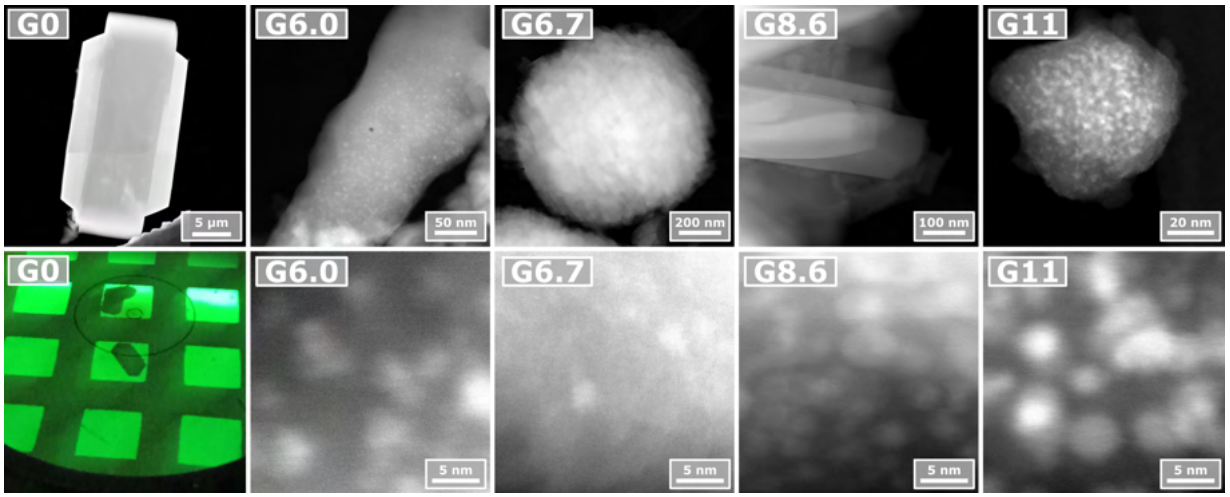

Figure 4.19: HAADF-STEM images of Ga-MFI zeotypes, recorded at an accelerating voltage of 300 kV, as well as an optical image of G0 to highlight its size. Bright spots indicate an increased thickness (multiple layers, G6.7 and G8.6 top row) or increased elemental density (Ga-based nanoparticles). Black dot in the centre of G6.0 is beam damage.

The acidity of Ga-MFI catalysts was thoroughly explored with NH_3-TPD (figure 4.20) and pyridine DRIFTS (figure S9, paper II). While G0 possesses a weak acid site ascribed to terminal silanol (from defects), incorporation of gallium introduces weak, strong, and extra-strong acid sites. Increasing the gallium content results in an increase in acid site density (table 4.7), parallel to what was observed for Al-MFI and Al-BEA. Additionally, the strength of the strong acid site increases, illustrated by a shift in the desorption peak towards higher temperatures. The different types of acid sites (figure 4.21) are classified into Brønsted acid sites (BAS, H^+), formed by framework gallium, and Lewis acid sites (LAS), formed by extra-framework gallium species. When performing pyridine DRIFTS at a specific temperatures, e.g., 300 °C, pyridine only binds to sites that require a higher temperature to desorb pyridine. Ideally, the acid sites are probed up to temperatures of 450 °C, isolating the extra-strong acid sites, but due to instrumental limitations, 300 °C was selected to examine strong sites and 150 °C to examine all sites.[32] Upon introduction of gallium, in G0.5, strong BAS (sBAS) are formed and a further increase to G1.2 also introduces weak LAS (wLAS). The relative distribution is denoted by the filled bars, with the numbers representing the percentage, while the absolute acid site densities[33] are denoted by the patterned bars. The long crystallisation step of G6.0 has resulted in a relatively high fraction of strong LAS (sLAS) and wLAS, while G6.7, G8.6, and G11 possess primarily strong BAS (sBAS) and wBAS. The gallium-based nanoparticles observed with HAADF-STEM do not correlate to a particular acid site, like extra-framework LAS, as the particles were most prevalent in G11 even though this catalyst only possesses a small fraction of LAS.

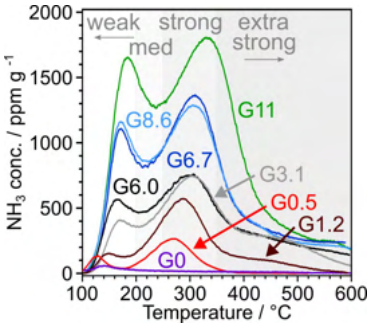

Figure 4.20: NH_3-TPD profiles of fresh Ga-MFI catalysts.

32: The weak sites are subsequently calculated by subtracting the number of strong sites from the total number of sites.

33: calculated by multiplying the acid site density from NH3-TPD with the fractions of the different sites

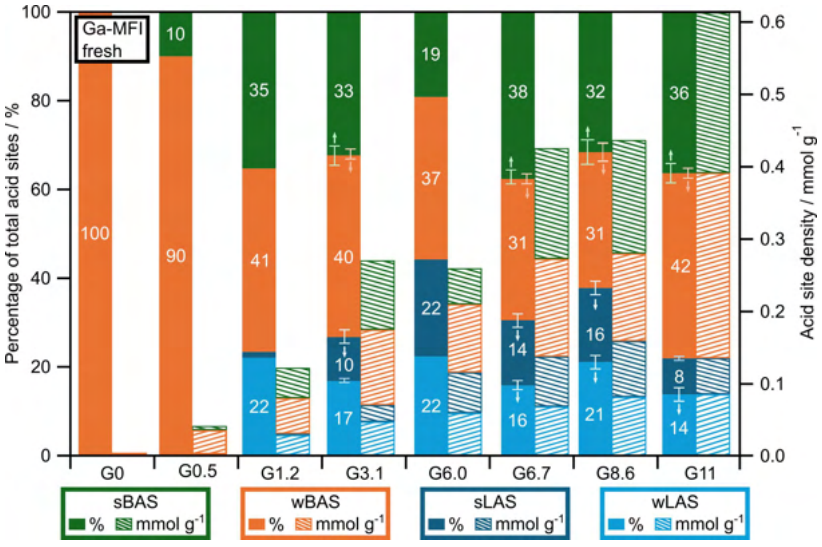

Figure 4.21: Distribution of the acid sites on fresh Ga-MFI given as a percentage (left axis) or as an acid site density based on NH_3-TPD (right axis). Sites are classified into strong and weak Brønsted acid sites (sBAS and wBAS), and strong and weak Lewis acid sites (sLAS and wLAS). G3.1, G6.7, G8.6 and G11 were measured twice and the error bars indicate the deviation from the average value.

Care must be taken before directly comparing the desorption temperatures from NH_3-TPD with those from pyridine DRIFTS, as the inherent differences between the bases, their interactions with the catalyst, and the experimental conditions, result in different desorption temperatures for the same sites. Another strategy to probe and isolate a specific site is by studying reactions that only occur on specific sites, such as the conversion of isopropylamine into propene and ammonia, occurring on strong BAS [156]. However, a more straightforward method involves the investigation of Na-Ga-MFI catalysts, intermediate states of the zeotype produced by calcination of the as-synthesised TPA-Ga-MFI. The acid site density of Na-G8.6 (figure 4.22) is compared with the protic H-G8.6 that has been described before. Na-G8.6 displayss a large weak acid site peak corresponding to ammonia that coordinates to the sodium cations, amounting to 0.344 mmol g^{-1} [157]. Sodium cations coordinate to the framework to compensate its negative charge,[34] $[GaO_2]^-$ (section 2.3.2), but protons (BAS) may still be present originating from the thermal decomposition of the TPA template molecules [158]. This explains the broad peak observed around 300 °C. Additionally, Na-G8.6 contains extra-strong peaks, which may be ascribed to framework-associated sodium, synergistically coordinating to framework BAS. After ion exchange into NH_4-G8.6 and subsequent calcination to form H-G8.6, the peak at 310 °C has increased substantially, evidencing that this strong acid site corresponds to a BAS. Na-G8.6 was tested for dmf conversion (not shown) and produced 0.64 mmol g^{-1} benzene, roughly a third of the production of H-G8.6 (table 4.8), demonstrating the importance of the BAS. During the reaction, the strong and extra-strong acid sites are deactivated (black, dots), implying that the reaction follows a similar mechanism as with H-G8.6.

34: likely not all of the sodium coordinates to negatively charged framework ($[GaO_2]^-$), thus potentially overestimating the actual acid site density.

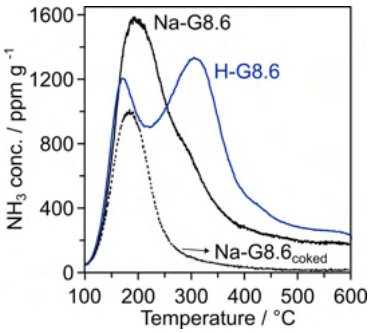

Figure 4.22: NH_3-TPD profiles of fresh Na-G8.6 and H-G8.6.

The catalytic performance of the Ga-MFI catalysts has been evaluated (figure 4.23 and table 4.8). The connection between the deactivation of the catalysts and their acid sites has been studied by performing both NH_3-TPD and pyridine DRIFTS on the coked catalyst. A detailed analysis is shown in paper II (figures 2 and S17, and table S8 [83]) and the main findings are described below:

1. Benzene is the main product at the start of the reaction, produced over sBAS. After deactivation by coke, 2,4-dmf becomes the main product which is produced over wBAS.
2. An increase in gallium content corresponds to an increase in the production of benzene, until a threshold is reached (>8.6 or ≥10.6 wt.%) , after which excessive coking dominates and results in premature deactivation. G6.7 produces the most benzene in 1 h TOS and G8.6 in 3 h, likely owing to their high acid site densities, the small crystal size of G6.7, and the promoting effect of extra-framework gallium in G8.6.

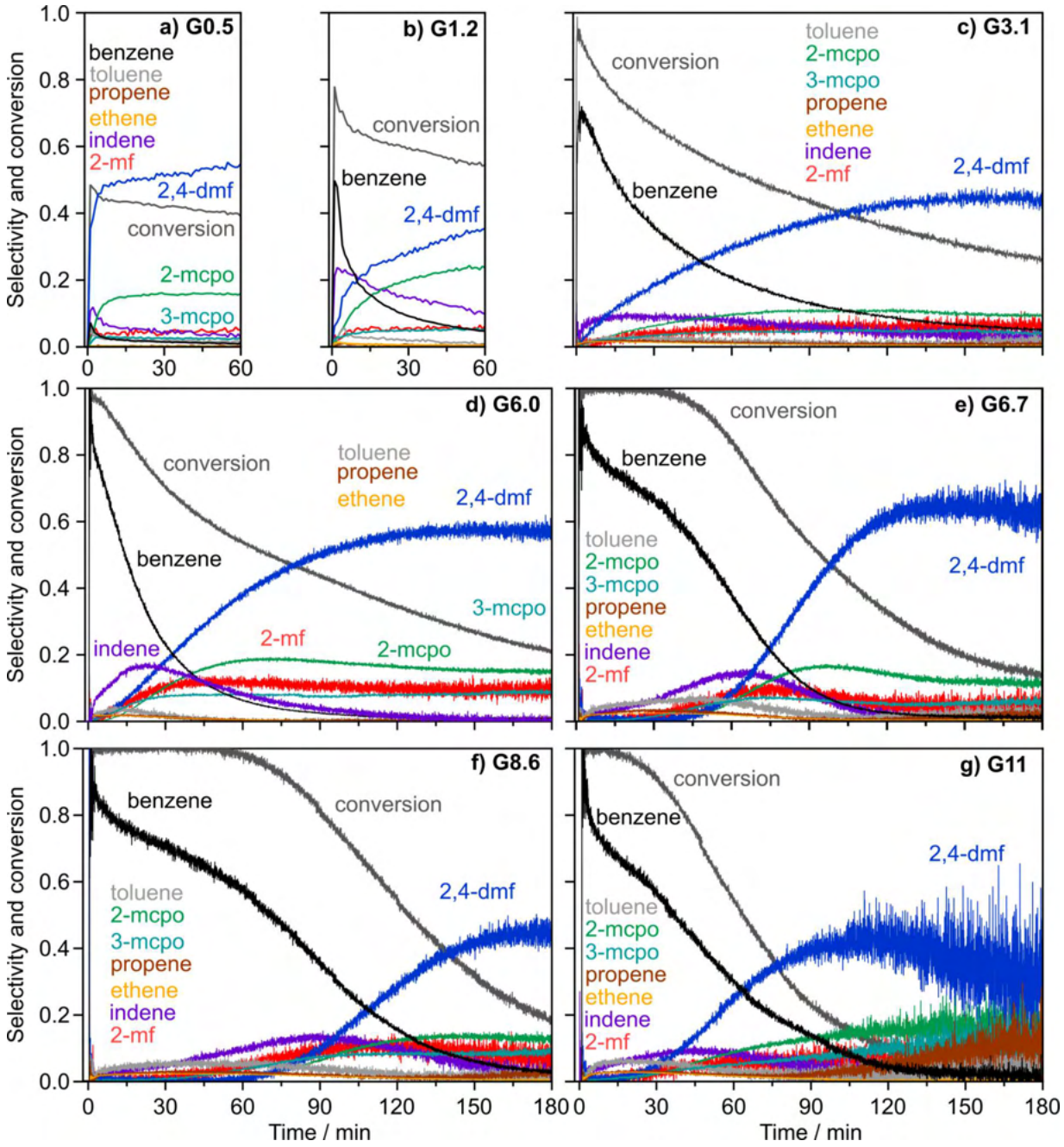

Figure 4.23: Conversion of dmf and selectivities of the main products over Ga-MFI. Concentrations were determined every 2 s, (G6.0, G6.7, G8.6, and G11), 4 s (G3.1) or 60 s (G0.5, G1.2). TOS is 1 h (G0.5, G1.2) or 3 h at 500 °C.

3. Strong BAS are vital for cracking, decarbonylation, and dehydration of protonated dmf, producing constituents for the hydrocarbon pool. Subsequent aromatisation is promoted by both sBAS and sLAS, demonstrated by the increased performance of G6.0 (22 % sLAS) compared to G3.1 (9 % sLAS).[35] The optimal catalyst possesses a balance between BAS and LAS, roughly in the range of BAS/LAS=1.5–2.5.

35: while they have a comparable acid site density of 0.268 and 0.256 mmol g^{-1} for G3.1 and G6.0, respectively

Table 4.8: Catalytic performance of Ga-MFI zeotypes.

Sample	Tol. 3 h[a] mmol g^{-1}	Benz. 3 h[a] mmol g^{-1}	Benz.[b] per acid	Benz. [c] per Ga	S_{coke} %
G0	0.04	0.00	1.8	N.A.	0.0
G0.5[d]	0.05	0.05	1.3	1.7	4.2
G1.2[d]	0.06	0.39	3.2	2.1	7.7
G3.1	0.06	0.89	3.3	1.7	8.0
G6.0	0.03	0.73	2.8	0.9	10.6
G6.7	0.16	1.65	3.9	1.2	12.7
G8.6	0.12	1.89	4.4	1.0	14.3
G11	0.10	1.14	1.9	1.1	16.4

[a] Toluene and benzene produced in 3 h dmf conversion at 500°C
[b] Molecules benzene produced per acid site in 3 h
[c] Molecules benzene produced per Ga atom in 3 h

Take-home message

An increase in gallium content generally corresponds to an increase in acid site density and improved catalytic performance, reaching an optimum at 6.7 and 8.6 wt.% Ga for 1 and 3 h TOS, respectively. A further increase results in a reduced activity and accessibility of each acid site. Aromatisation of dmf occurs primarily via the strong Brønsted acid sites, promoted by strong Lewis acid sites.

4.4 The effect of mesoporosity

The previous chapters have demonstrated the importance of selecting an appropriate microporous structure, active metal, and metal content. However, all tested catalysts suffer from rapid deactivation due to coking, reducing the accessibility of the acid sites and lowering the activity per acid site. Therefore, this subchapter investigates the effect of introducing a secondary porous network, consisting of meso- and macropores, [36] with the goal to aid mass transfer of reactants and products, ultimately reducing coking and increasing the lifetime of the catalysts.

Four classes of materials have been investigated, as described in more detail in paper III and section 3.1 [92], including mesoporous Ga-MFI$_{meso}$, Ga-MCM-41, Ga-MFI/MCM-41, and Ga-SPP.

36: reminder: micropores are < 2 nm, mesopores are between 2 and 50 nm, and macropores are > 50 nm [60, 61]

4.4.1 Ga-MFI$_{meso}$

After exposing Ga-MFI catalysts to the base TPAOH to introduce mesopores, their microporous MFI structure was preserved, as confirmed by XRD (figure 4.24). The XRD diffractograms of Ga-MFI$_{meso}$ (blue) are nearly identical to the diffractograms of their parent material (black), even displaying an increase in crystallinity.[37]

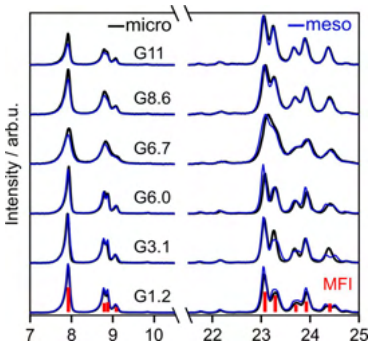

Figure 4.24: Close-up of the XRD diffractograms of Ga-MFI$_{meso}$ (blue) and their parent material Ga-MFI$_{micro}$ (black), with reference Si-MFI [143].

Due to the preferential dissolution of Si-OH, Si-O$^-$, and Si-O-Si bonds in basic medium, compared to Si-O-Ga bonds, the relative gallium content of G1.2$_{meso}$ and G3.1$_{meso}$ has been increased (table 4.9). Remarkably, the basic treatment resulted in a decrease in gallium content for catalysts with a gallium content of ≥6.0 wt.%, signifying a preferential loss of gallium instead of silicon. This is likely caused by the loss of gallium-based nanoparticles, which were prevalent in the parent Ga-MFI$_{micro}$ material (figure 4.19). When framework silicon is dissolved, gallium nanoparticles or extra-framework species lose their anchoring sites and microporous confinement.

37: Peak at 24.4 ° in G3.1$_{micro}$ and G6.0$_{micro}$ is resolved into two peaks at 24.3° and 24.5 °, caused by the recrystallisation of dissolved nutrients in the presence of TPA$^+$ [159].

The effect of the base treatment on the pore topology of the catalysts has been analysed with nitrogen physisorption, as shown in figure 4.25. The isotherms resemble those of Ga-MFI$_{micro}$, displaying micropore filling at low pressures and hysteresis from mesopores at high pressures. Dissolution of microporous material in G1.2$_{meso}$ and G3.1$_{meso}$ has lowered their SA and V_{mic}, as shown in table 4.10, compared to Ga-MFI$_{micro}$ (table 4.7). Notably, high-gallium-content Ga-MFI$_{meso}$ catalysts demonstrate an increase in SA and V_{mic}, which is also traced back to their loss of gallium-based nanoparticles. Specifically, nitrogen can now access micropores and surface area that had been blocked previously, suggesting that the SA and V_{mic} of Ga-MFI$_{micro}$ had been underestimated before.

Sample	Ga wt.%	Si/Ga
G1.2$_{meso}$	1.4	81
G3.1$_{meso}$	3.9	27
G6.0$_{meso}$	4.8	22
G6.7$_{meso}$	5.3	19
G8.6$_{meso}$	5.3	15
G11$_{meso}$	8.5	11

Table 4.9: Elemental compositions of Ga-MFI$_{meso}$ determined with XRF.

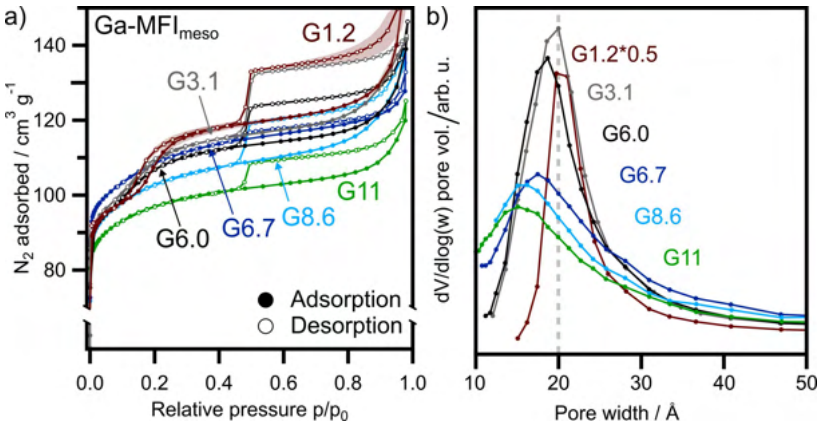

Figure 4.25: N_2-physisorption isotherms of Ga-MFI$_{meso}$ (a). G1.2$_{meso}$ was measured twice and the average value is shown, as well as the variance indicated by the shaded area. The mesopore size distribution (b) is derived with the BJH-model on the adsorption curve. The derivative of the pore volume of G1.2 is multiplied by a factor of 0.5.

Additionally, Si-O-Ga bonds limit the dissolution of the framework and dissolved nutrients may recrystallise in the presence of TPAOH, all plausibly increasing the SA and V_{mic}.

Notably, the shape of G1.2$_{meso}$ is different than G1.2$_{micro}$ and includes a secondary adsorption and hysteresis between p/p_0=0.12–0.30, similar to what has been seen for Si-MFI/G0$_{micro}$ and G0.5$_{micro}$ (figure 4.15). As this is caused by nitrogen that has adsorbed indiscriminately, G1.2$_{meso}$ must have lost coordinating sites, such as gallium-species or acid sites.[38]

The mesoporous volume of the hysteresis loop, located between p/p_0=0.435–0.975, can be approached by subtracting the adsorption curve from the desorption curve. This has been done for Ga-MFI$_{micro}$ (figure 4.15) and Ga-MFI$_{meso}$ (figure 4.25), resulting in A_{meso} and A_{micro}, each signifying the size or area of the hysteresis loop. To determine the extent of mesopore formation, the ratio A_{meso}/A_{micro} has been calculated (table 4.10).[39] G1.2 and G3.1 have the highest ratios of 3.5 and 5.2, respectively, further proving that the extent of the mesopore introduction is the highest in the low-gallium-content zeotypes. Additionally, the similarities between the ratios of G6.0, G6.7, and G8.6, all amounting to 2.8, suggest a robustness of the used methodology and the absence of an effect of the gallium content.[40] Further analysis of the PSD reveals that the mesopore introduction has not resulted in an increase in average pore diameter of G1.2$_{meso}$ and G3.1$_{meso}$ (both 20 Å), compared to their microporous counterparts. For the other zeotypes, mesopore introduction decreased the average pore diameter by roughly 2 to 3 Å. This may be caused by the recrystallisation step, which is promoted by TPA^+. However, TPA^+ is too large to enter the micropores and instead resides on the external surface of the mesopores, aiding crystallisation of additional layers of material which lowers the average diameter [93].[41]

38: as gallium content only increased, it must have lost acid sites, which will be investigated with NH_3-TPD

39: These numbers must be interpreted qualitatively since the sharp dip in the desorption curve at p/p_0=0.42 is an artifact caused by the tensile strength effect.

40: Heavy elements and multilayered crystals appear as bright spots, while the absence of material, or thinner sheets, appear as darker spots as they do not reflect as many electrons.

41: S_{ext} can typically also be used to evaluate the mesopores area but due to the inconsistent shape of the adsorption isotherm of G0, G0.5, and G1.2$_{meso}$, a range of the thickness curve was selected after which mesopore filling was complete. Consequently, the determined microporous area also includes the mesoporous area, and S_{ext} only refers to the remaining external (outer) surface of zeotype crystals.

Sample	SA[a] $m^2\,g^{-1}$	S_{ext}[b] $m^2\,g^{-1}$	V_{mic}[b] $cm^3\,g^{-1}$	A_{meso}/A_{micro}[c]
$G1.2_{meso}$	398 ± 2	28 ± 5	0.166 ± 0.004	3.5
$G3.1_{meso}$	401	25	0.164	5.2
$G6.0_{meso}$	395	22	0.161	2.8
$G6.7_{meso}$	416	26	0.161	2.8
$G8.6_{meso}$	393	28	0.150	2.8
$G11_{meso}$	374	21	0.144	2.3

[a] Surface areas by BET, p/p_0 = 0.002–0.03 following consistency criteria [112]
[b] By t-plot method[116] (Harkins and Jura equation, t= 5.0–8.0 Å)
[c] Ratio between the area of hysteresis loops of Ga-MFI_{meso} and Ga-MFI_{micro}, calculated from p/p_0= 0.435–0.975.

Table 4.10: Textural properties of Ga-MFI_{meso}, derived from nitrogen physisorption.

The morphology of the crystals was studied with SEM (figure S2, paper III) [92] and HAADF-STEM (figure 4.26). Darker spots illustrate the absence of material and thus the presence of voids within crystals and crystal aggregates, like meso- and macropores. These voids vary in shape and size, ranging from 100 to 10000 nm^2, and are mostly empty for $G1.2_{meso}$ and $G3.1_{meso}$, while gallium nanoparticles are observed inside the pores of higher-gallium-content zeotypes, illustrated by bright spots. While the nanoparticles of Ga-MFI_{micro} are in the range of 1 to 5 nm, those of Ga-MFI range up to several tens of nanometers in Ga-MFI_{meso}, due to Ostwald ripening and agglomeration of the smaller nanoparticles that were released upon partial framework dissolution. HAADF-STEM/EDX (figure 4.27) was used to confirm that the nanoparticles are gallium-based.[42]

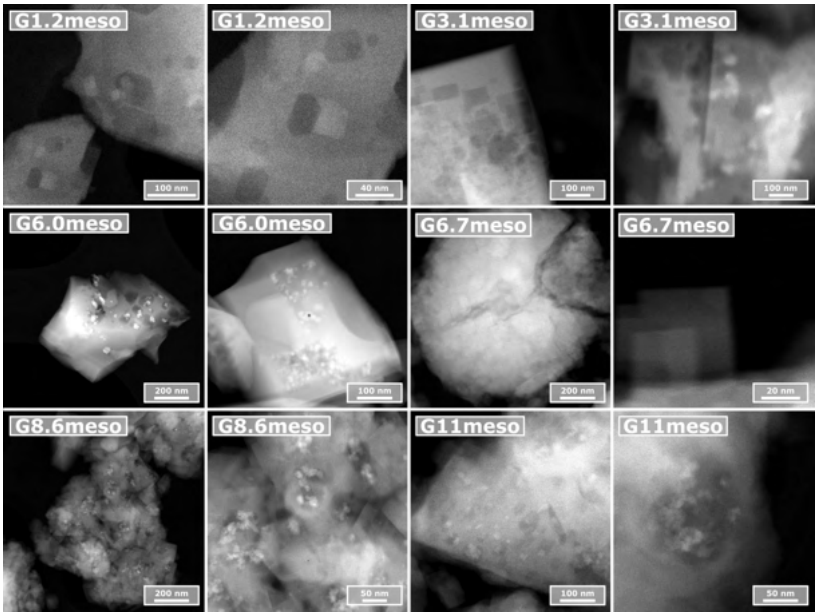

Figure 4.26: HAADF-STEM images of Ga-MFI_{meso} recorded at 300 kV. Black dot in the centre of $G6.0_{meso}$ is beam damage.

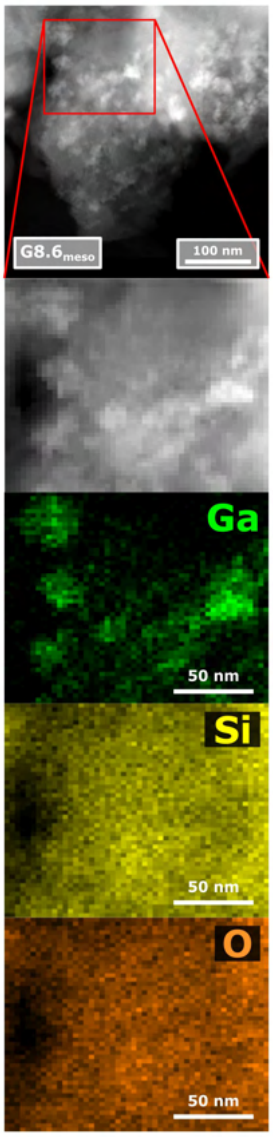

Figure 4.27: HAADF-STEM image of $G8.6_{meso}$ and EDX maps. Pixel size is 3 nm.

42: The homogeneous oxygen dispersion across the material and nanoparticles suggests that they are of gallium oxides in nature.

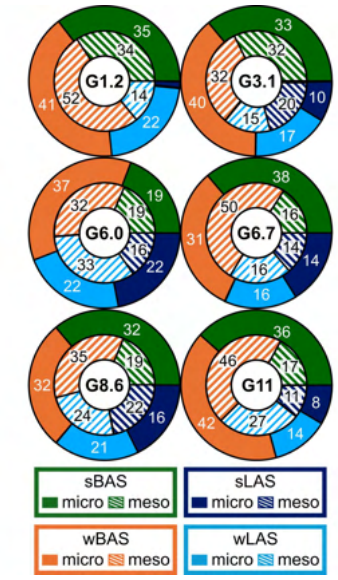

Figure 4.28: Acid site distributions of fresh Ga-MFI$_{micro}$ (filled) and fresh Ga-MFI$_{meso}$ (patterned) with strong BAS (green), weak BAS (orange), strong LAS (dark blue), and weak LAS (light blue), as derived from pyridine DRIFTS. The numbers display their fractional abundance in percentages.

The acidity of Ga-MFI$_{meso}$ was evaluated with pyridine DRIFTS and NH_3-TPD, shown in figures 4.28, 4.29, and figure 6 (paper III). The acid site densities (table 4.11) demonstrate that all mesoporous zeotypes have lost roughly half of their acid sites compared to Ga-MFI$_{micro}$. In particular, strong and extra strong sites were lost due to the dissolution and loss of acidic framework and extra-framework gallium.[43] Pyridine DRIFTS reveals that strong Brønsted (sBAS, dark green) were disproportionately lost for all zeotypes, while strong Lewis acid sites (sLAS, dark blue) were mainly lost for G1.2$_{meso}$ and G6.0$_{meso}$. The dissolution of framework Si-Ga-OH species has resulted in a relative increase in LAS for all zeotypes except G1.2$_{meso}$, illustrated by a decrease in BAS/LAS.

Remarkably, acid sites are also generated by the mesopore introduction in G6.0$_{meso}$, indicated by the increase in the peak desorbing at 175 °C (b, black). This indicates that migration of gallium and recrystallisation not only results in non-acidic nanoparticles but also produces acid sites. To be more precise, pyridine DRIFTS allows these sites to be classified as weak Lewis acid sites since their fraction (light blue) increases. The quantification and complete distribution of the acid sites can be found in paper III, figures 6 and S7 [92].

43: demonstrating that the TPAOH treatment was too harsh.

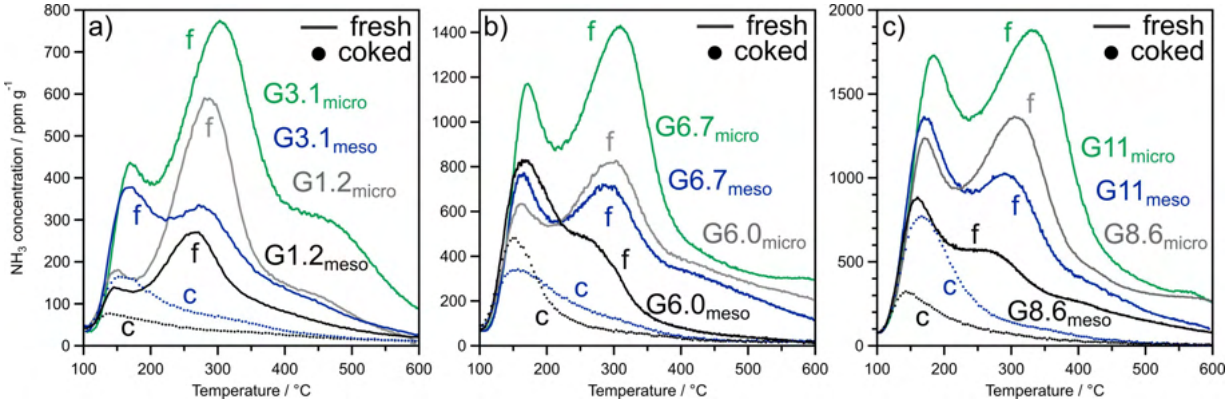

Figure 4.29: NH_3-TPD profiles of fresh Ga-MFI$_{micro}$ (green/grey), fresh Ga-MFI$_{meso}$ (black/blue), and coked Ga-MFI$_{meso}$ (black/blue dots), including G1.2 (a), G3.1 (a), G6.0 (b), G6.7 (b), G8.6 (c), and G11 (c). Please note the differences in the scaling of the y-axis.

The catalytic activity of Ga-MFI$_{meso}$ (figure 9, paper III [92]) resembles that of Ga-MFI$_{micro}$, yielding benzene as the main product at the start of the reaction and 2,4-dmf at the end. For direct comparison, the benzene productions over Ga-MFI$_{micro}$ and Ga-MFI$_{meso}$ are shown in figure 4.30, displaying two clear trends across all gallium contents.

1. The initial production of benzene over Ga-MFI$_{meso}$ is equal to or higher than over Ga-MFI$_{micro}$. As their acid site density has halved, each acid site produces significantly more benzene, confirming their increased accessibility due to the introduction or expansion of the number of meso- and macropores, which aiding the transport of reactants and products.
2. Ga-MFI$_{meso}$ catalysts are deactivated more rapidly regarding the production of aromatics, which is caused by two reasons. Firstly, fewer acid sites are present which require fewer coke molecules to be covered and deactivated. Secondly, the increased production of benzene at the start of the reaction likely corresponds to an increased production of coke as well.[44] In fact, normalising to the acid sites again, each acid site now produces or deals with at least twice as many coke molecules, logically resulting in a faster deactivation.

44: although an inverse relationship between the formation of benzene and coke is also plausible.

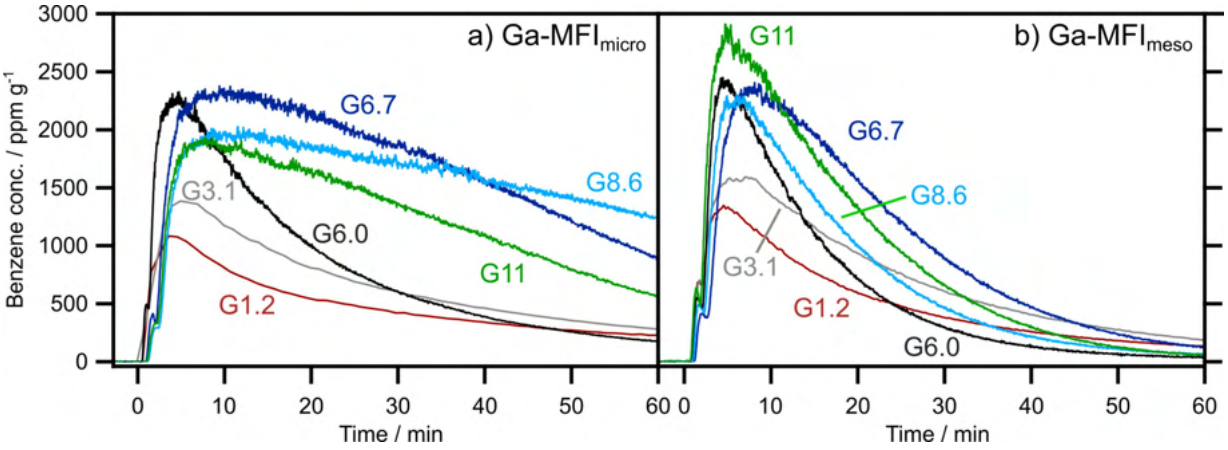

Figure 4.30: Benzene production during the first hour TOS of Ga-MFI$_{micro}$ (a) and Ga-MFI$_{meso}$ (b).

Generally, Ga-MFI$_{meso}$ catalysts produce similar amounts of benzene as their Ga-MFI$_{micro}$ counterparts, effectively increasing the production of benzene per site (table 4.11). Exceptions are G6.7-MFI$_{meso}$ and G8.6-MFI$_{meso}$, which demonstrate both a decreased total production of benzene and benzene per site, indicating that the downside of the loss of acid sites outweighs the benefits of the enhanced mass transport. Previously, the aromatisation reaction was shown to occur on strong and extra-strong acid sites, mainly of Brønsted character, which are exactly the sites that were lost during mesopore introduction.[45] NH_3-TPD of the coked mesoporous catalysts (figure 4.29, black/grey dots) reveals that the strong and extra-strong acid sites are primarily coked, indicating that

45: so the loss in relevant acid sites is even higher than the loss in total acid site density, and thus the beneficial effect of the meso- and macropores even greater.

Table 4.11: Overview of the acid site densities and catalytic performance of Ga-MFI$_{meso}$.

Sample	Acidity[a] mmol g^{-1}	Acid lost[b] %	BAS/ LAS[c]	Tol. 3 h mmol g^{-1}	Benz. 1 h mmol g^{-1}	Benz. 3 h mmol g^{-1}	Benz/ site[d]	S_{coke} %
G1.2$_{meso}$	0.052	56	6.2	0.02	0.39	0.46	8.8	4.2
G3.1$_{meso}$	0.124	54	1.8	0.14	0.62	0.72	5.8	7.6
G6.0$_{meso}$	0.140	45	1.0	0.06	0.48	0.50	3.6	11.9
G6.7$_{meso}$	0.249	41	2.0	0.06	0.74	0.78	3.1	16.3
G8.6$_{meso}$	0.212	51	1.2	0.04	0.57	0.58	2.7	14.3
G11$_{meso}$	0.354	42	1.7	0.07	0.74	0.75	2.1	15.8

[a] Acid site density, determined with NH_3-TPD
[b] Acid site density lost compared to fresh Ga-MFI$_{micro}$
[c] Ratio between BAS and LAS, determined with pyrdine DRIFTS
[d] Total benzene production in 3 h per acid site, dimensionless

the reaction on Ga-MFI$_{meso}$ likely occurs according to the same mechanism as it does on Ga-MFI$_{micro}$.

Take-home message

Meso- and macropore introduction Ga-MFI$_{meso}$ resulted in the agglomeration of gallium-based nanoparticles inside the pores for G6.0$_{meso}$, G8.6$_{meso}$, and G11$_{meso}$, while halving the acid site densities of all zeotypes. Primarily the strong Brønsted and Lewis acid sites are affected, lowering the total benzene production while simultaneously increasing the activity per acid site. This demonstrates the beneficial effect of the meso- and macropores on the mass transport of reactants and products.

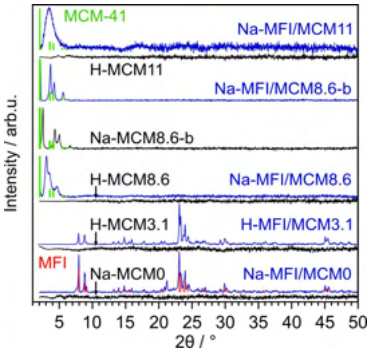

Figure 4.31: XRD diffractograms (a) of Ga-MCM-41 (black) and Ga-MFI/MCM-41 (blue). Peaks associated with the crystal lattice planes of the MFI framework structure [143] and MCM-41 structure [160] are denoted by red and green bars, respectively.

4.4.2 Ga-MFI/MCM-41

The study of the Ga-MFI$_{meso}$ series reveals the drawbacks of introducing a secondary pore network through post-synthesis modification of existing microporous catalysts, such as a significant loss of acid site density. Therefore, Ga-MFI/MCM-41 and Ga-MCM-41 micro- and mesoporous catalysts were developed through a 1-pot hydrothermal synthesis.

The selected gallium contents are 0, 3.1, 8.6, and 11 wt.%. The synthesis of 8.6 and 11 wt.% Ga catalysts proved difficult due to the effect of the acidic precursor on the ageing and crystallisation steps. Therefore, a series of over 24 samples was prepared (table S3 and figure S1, paper III [92]) in which the gallium content, base concentration, alkali source, and ageing conditions were systematically varied. Five Ga-MCM-41 and five Ga-MFI/MCM-41 samples have been selected for further analysis, including MCM8.6-b and MFI/MCM8.6-b, which were synthesised with a higher NaOH concentration.

Their XRD diffractograms are shown in figure 4.31 and figure 3 (paper III), and no peaks were observed for the MCM series, with the exception of Na-MCM8.6-b.[46] This may indicate the absence of a well-ordered mesoporous structure, although the low quantity of material synthesised and analysed may play a role too, resulting in fewer diffracted X-rays and a lower signal-to-noise ratio (SNR).[47] After 9 days of crystallisation, MFI/MCM0 and MFI/MCM3.1 display peaks associated with the MFI structure (red bars [143]) confirming the successful transformation into MFI, either partial or complete. For catalysts with a gallium content >3.1 wt.%, the diffractograms display several peaks in the low 2θ region, associated with a mesoporous structure, e.g., MCM-41 (green bars [160]).[48] The peaks of Na-MFI/MCM8.6-b have shifted to lower angles compared to Na-MCM8.6-b, indicating an increase in d-spacing and possibly an increase in mesopore size. This indicates that even though no MFI was formed, the second crystallisation step has resulted in the partial dissolution of the framework, enlarging the mesopores.

46: synthesised with a longer ageing step and a higher pH of the precursor mixture.

47: This may be resolved by measuring small-angle X-ray scattering [161] or reproducing the synthesis on a larger scale.

48: It is undetermined if the second crystallisation step introduced mesopores or that they were simply not measured for Ga-MCM-41 due to a low sample amount.

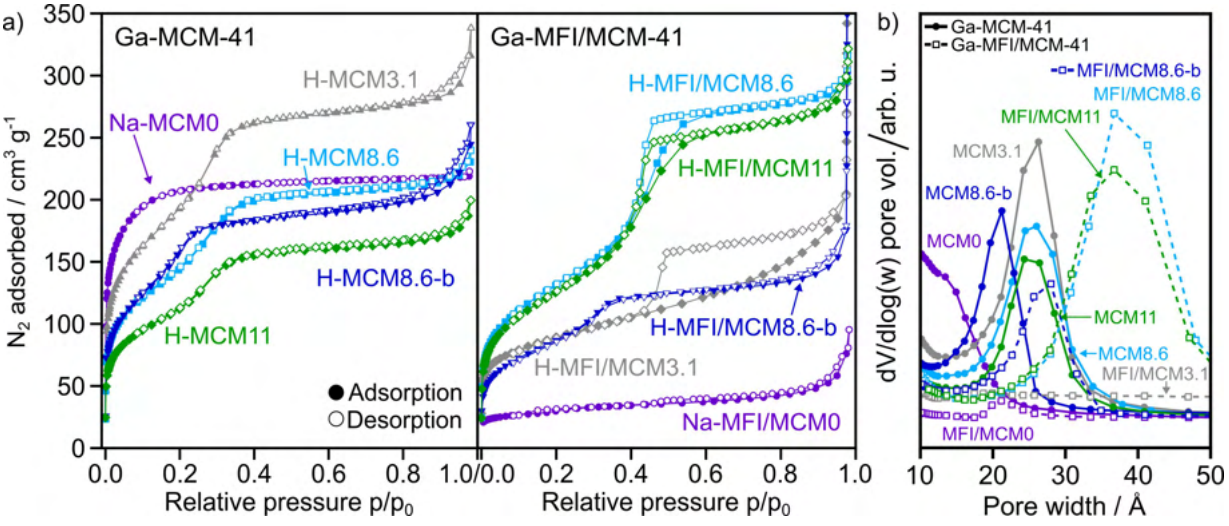

Figure 4.32: Nitrogen physisorption isotherms (a) of Ga-MCM-41 and Ga-MFI/MCM-41. Mesopore size distribution (b) of Ga-MCM-41 (full, dots) and Ga-MFI/MCM-41 (dashed, squares), derived with the BJH-model applied to the adsorption curve.

Nitrogen physisorption (figure 4.32, a) reveals that the Ga-MCM-41 samples are mesoporous, as the isotherms are of reversible type IV, associated with mesoporous adsorbents [104]. The adsorption step between p/p_0=0.1–0.3 is caused by capillary condensation and its position is related to the pore width; an inflection point at lower pressure, observed for H-MCM8.6-b, corresponds to a smaller pore diameter [107, 162]. Additionally, the lack of hysteresis shows that the mesopores are smaller than the critical diameter of approximately 40 Å for nitrogen at 77 K , applicable to cylindrical pores in type IV isotherms [104, 163]. These results are confirmed by the mesopore size distribution (b) in which Ga-MCM-41 is represented by the filled lines and dots. The isotherm of Na-MCM0

is of type I(b), associated with materials containing wider micropores or narrow mesopores with a diameter < 25 Å [104]. Its PSD (purple, filled) does not contain a sharp peak but a gradual increase of pores with a diameter below 20 Å, reaching the microporous regime. As sharp peaks were observed for sample with gallium in the framework, it appears that gallium aids the formation of mesoporous structures.

After the second crystallisation step, MFI/MCM0 resembles type I and MFI/MCM3.1, a composite of type I and type IV, representative of micro- and mesopores, respectively. This confirms the successful partial transformation of MCM-41 into MFI in MFI/MCM3.1. Remarkably, MFI/MCM0 displays a second adsorption step and hysteresis loop between p/p_0=0.1–0.3, identical to what was observed before for G0, G0.5, and G1.2$_{meso}$. As a consequence of the desilication procedure, its SA has reduced significantly from 778 to 105 m^2/g, as well as its V_{mic} from 0.325 to 0.038 $cm^3\ g^{-1}$ (table 4.12).[49] This is an indication of the presence of a large fraction of amorphous material, suggesting that while most of the MCM0 framework dissolves and amorphizes during the high-temperature synthesis step, not all nutrients recrystallise into MFI. This effect was also observed to a lower degree in MFI/MCM3.1, which exhibits a loss in SA from 718 to 316 m^2/g and in V_{mic} from 0.388 to 0.089 $cm^3\ g^{-1}$. The adsorption of nitrogen gradually increases when increasing the pressure, indicating a wide range of meso- and macropores instead of purely MFI micropores. Additionally, a hysteresis loop has formed that is associated intercrystalline mesopores, similar to what was seen for Ga-MFI$_{micro}$ and Ga-MFI$_{meso}$ zeotypes, associated with

On the other hand, MFI/MCM8.6 and MFI/MCM11 display an increase in V_{mic} and SA (MFI/MCM11), indicating that the 2nd high-temperature step has promoted the crystallisation of new mesoporous material instead of favouring the dissolution of existing material. The SA and V_{mic} of MFI/MCM8.6-b both go down, in accordance with the results from XRD that the mesopore size has increased due to dissolution of material. Moreover, the average pore diameter increases for all Ga-MCM-41 samples after their transformation to Ga-MFI/MCM-41, indicating that even though formation of MFI was not always successful, initial dissolution of the material has occurred.

The morphology was analysed with SEM (figures 4.33 S4, paper III) and the transformation from MCM-41 into MFI can also be observed on a larger scale. MCM0 comprises agglomerates of smooth crystals of inconsistent sizes and shapes, whereas after the transformation, well-defined crystals have formed that are lamellar-, petal-, needle-, and coffin-shaped, similar to Ga-MFI (figure 4.17). Likewise, MCM3.1 experienced a partial transformation from random intergrowths into cylindrical rods, likely MFI, with a

49: V_{mic} not only describes the microporous volume of these samples but rather the sum of the micro- and mesoporous volume. Due to capillary condensation and the mesopore inflection point, a usable thickness range can only be selected after mesopore filling (except for MFI/MCM3.1), demonstrating the limitations of the t-plot method.

Sample	Ga-MCM-41			Ga-MFI/MCM-41		
Ga wt.%	SA[a] $m^2\,g^{-1}$	S_{ext} $m^2\,g^{-1}$	V_{mic}[b] $cm^3\,g^{-1}$	SA[a] $m^2\,g^{-1}$	S_{ext} $m^2\,g^{-1}$	V_{mic}[b] $cm^3\,g^{-1}$
0	778	11	0.325	106	26	0.038
3.1	718	39	0.388	316	140	0.089
8.6	542	26	0.298	499	51	0.378
8.6-b	558	44	0.261	326	37	0.169
11	422	27	0.228	474	66	0.342

[a] Apparent surface areas by BET method, $p/p_0 = 0.005$–0.5 following consistency criteria [112]
[b] By t-plot method [116] (Harkins and Jura equation, t= 6.0–9.0 Å)

Table 4.12: Textural properties of Ga-MCM-41 and Ga-MFI/MCM-41, derived from nitrogen physisorption.

diameter of 5 to 10 µm. The other materials remained intergrowths of no specific size or shape. No clear voids or gallium-based nanoparticles were observed with TEM and HAADF-STEM (figure S5, paper III).

The acid sites have been analysed with NH_3-TPD (figure 4.34) and their acid site densities are quantified (table 4.13). Ga-MCM-41 catalysts possess multiple acid sites, including a medium (desorbing at 210 °C) and extra-strong site (440 °C). Desorption of ammonia was incomplete at 600 °C for all catalysts, indicating that the catalysts possess even stronger sites. After the second crystallisation step, additional acid sites have formed in MFI/MCM8.6 (weak) and MFI/MCM11 (weak and strong). Transformation of MCM3.1 into MFI/MCM3.1 has introduced an additional strong acid site, of which ammonia desorbs at 290 °C. Since this site was also observed for Al-MFI and Ga-MFI, it is recognized as an MFI framework Brønsted acid site. A further distinction using pyridine DRIFTS (not shown) results in a distribution of 23 % sBAS, 35 % wBAS, 18 % sLAS and 24 % wLAS, amounting to a BAS to LAS ratio of 1.4. Compared to $G3.1_{micro}$ (figure 4.21), it possesses more LAS, likely due to its lower fraction of microporous MFI framework and concomitant BAS.

As was done for $G8.6_{micro}$ in section 4.3.3, the sodium-containing precursors of the catalysts are also investigated. For Na-MFI/MCM8.6 (0.190 mmol g^{-1}), all types of acid sites were increased after conversion to H-MFI/MCM8.6 (0.285 mmol g^{-1}), resulting in an increased production of benzene (0.05 vs. 0.07 mmol g^{-1}). In contrast, the acid site densities of Na-MCM8.6-b and H-MCM8.6-b are relatively similar (0.372 vs. 0.382 mmol g^{-1}), as well as their benzene production (0.05 vs.0.06 mmol g^{-1}), implying that the ion exchange was ineffective or that Na-MCM8.6-b already contains BAS. Furthermore, the acid site density of Na-MFI/MCM8.6-b (0.456 mmol g^{-1}) decreased when converting it to to H-MFI/MCM8.6-b (0.327 mmol g^{-1}), although its benzene production increased from 0.01 vs. 0.06 mmol g^{-1}. In short, the relationship between the

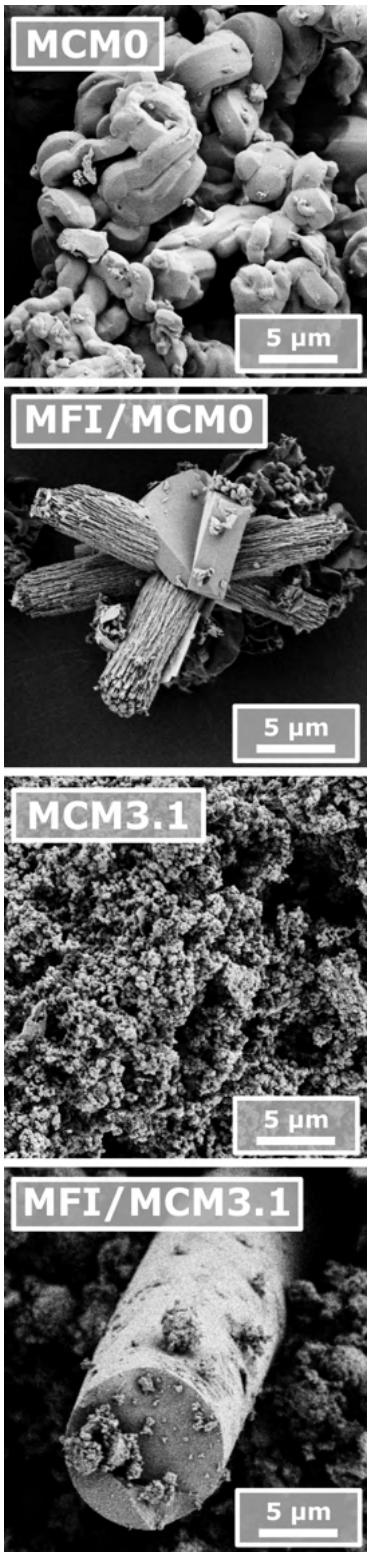

Figure 4.33: SEM images of MCM0, MFI/MCM0, MCM3.1, and MFI/MCM3.1, recorded at 1.5 kV

acidity of Ga-MCM-41, the benefits of ion exchange, and its catalytic performance, is complex and further investigation is necessary.[50]

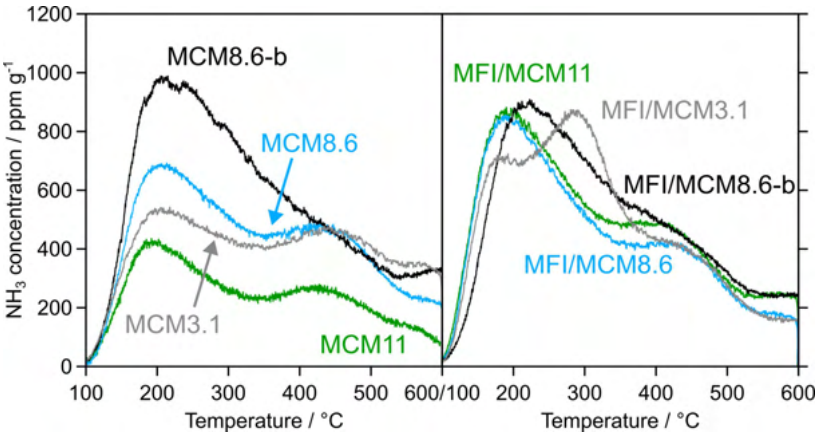

Figure 4.34: NH_3-TPD profiles of Ga-MCM-41 and Ga-MFI/MCM-41.

The catalytic performance has been tested (figure S10, paper III) and the main products are benzene, indene, 2-mcpo, 3-mcpo, and 2-methylfuran. Even though the catalysts possess moderately high acid site densities ($\geq 0.161\,mmol\,g^{-1}$), benzene and toluene production is relatively low, averaging $0.05\,mmol\,g^{-1}$ in 3 h TOS (table 4.13). This shows that some catalytic descriptors, such as the gallium content, acid site density, and presence of a mesoporous framework, are of secondary importance compared to the presence of a microporous framework. This statement is supported by the near five-fold increase in the production of benzene of MFI/MCM3.1, from 0.06 to $0.28\,mmol\,g^{-1}$, compared to MCM3.1.[51] Moreover, when comparing MFI/MCM3.1 to $G3.1_{micro}$, a catalyst comprising primarily the MFI framework, it only exhibits a third of its benzene production (0.28 vs. $0.89\,mmol\,g^{-1}$), further stressing the crucial role that the microporous MFI structure plays on steering the selectivity towards BTX.[52] Instead of benzene, the Ga-MCM-41 and other Ga-MFI/MCM-41 catalysts favour the production of the polycyclic aromatic indene, likely promoted by the additional space available compared to microporous Ga-MFI. Indene was subsequently aromatised into other polyaromatic hydrocarbons like coke, illustrated by the high selectivities to coke of 36 % for MFI/MCM8.6 and MFI/MCM11.

50: Na-MFI/MCM3.1 was not studied due to a limited quantity of the material available. Because the production of BTX is relatively low for this class of materials, its signal-to-noise ratio is low too, further complicating data interpretation and reducing the reliability of the data.

51: owing exclusively to the MFI framework as its acid site density is similar and its SA and V_{mic} both decreased.

52: $G3.1_{micro}$ possesses a similar acid site density and distribution, allowing its increased performance to be ascribed to its higher fraction of microporous MFI framework.

Sample	Ga-MCM-41			Ga-MFI/MCM-41		
Ga wt.%	Acid[a]	Benz. 3 h	S_{coke}	Acid[a]	Benz. 3 h	S_{coke}
	mmol g^{-1}		%	mmol g^{-1}		%
0	0.000	0	N.A.	N.A.	N.A.	
3.1	0.265	0.06	31	0.309	0.28	15
8.6	0.280	0.04	26	0.285	0.07	36
8.6-b	0.382	0.05	32	0.327	0.06	26
11	0.161	0.03	24	0.313	0.08	36

[a] Acid site density determined by NH_3-TPD

Table 4.13: Acid site densities and catalytic performance of Ga-MCM-41 and Ga-MFI/MCM-41.

Take-home message

Mesoporous Ga-MCM-41 catalysts were synthesised with varying gallium contents, exhibiting high acid site densities. However, they demonstrate a low selectivity to BTX and high selectivity to coke, owing to the lack of pore confinement in the larger mesopores. Through partial transformation, a hierarchical micro- and mesoporous composite Ga-MFI/MCM-41(Ga=3.1 wt.%) was prepared, which also possesses a high acid site density. Its catalytic performance is improved fivefold compared to Ga-MCM-41, highlighting the importance of the microporous MFI framework.

4.4.3 Ga-SPP

Another class of catalysts that investigate the relationship between micro- and mesopores comprises gallium-containing self-pillared pentasil units (Ga-SPP), with a varying gallium content of 1.2, 2.4, and 3.6 wt.%.

The XRD diffractograms (figure 4.35, a), demonstrate broad diffraction peaks associated with the MFI framework (red sticks [143]). The broadening and overlap of the peaks is caused by the random ordering of the pentasil units. The SNR of SPP2.4 is higher than both SPP3.6 and SPP1.2, suggesting that a moderate amount of acidic gallium precursors resulted in the optimal pH for hydrolysis, condensation, and crystallisation, as the amount of added basic template TBAOH was kept constant.

Nitrogen physisorption isotherms (b) are composites of reversible type II and type IV, associated with macroporous and mesoporous materials, respectively [104]. PSD shows a broad distribution of pore widths of ≥50 Å, confirming the disordered random pore structure of the Ga-SPP catalysts. The textural properties are shown in table 4.14 and the surface area and microporous volume are the largest for SPP2.4, amounting to 532 m^2/g and 0.093 $cm^3\ g^{-1}$.

Table 4.14: Physicochemical properties and catalytic performance of Ga-SPP.

Sample	SA[a] $m^2\,g^{-1}$	S_{ext}[b] $m^2\,g^{-1}$	V_{mic}[b] $cm^3\,g^{-1}$	Acidity $mmol\,g^{-1}$	Benz. 3 h $mmol\,g^{-1}$
SPP1.2	369	241	0.050	0.001	0.003
SPP2.4	532	309	0.083	0.003	0.002
SPP3.6	508	331	0.085	0.007	0.033

[a] Apparent surface area by BET method, p/p_0 = 0.01–0.13 following consistency criteria [112]
[b] By t-plot method [116] (Harkins and Jura equation, t= 3.5–5.0 Å)

53: Due to the shape of the isotherm, an appropriate thickness range could be selected (3.5–5.0 Å), hence, the mesoporous area equals the S_{ext}.

The large external surface area of more than 300 $m^2\,g^{-1}$ determined for each Ga-SPP, demonstrates the presence of meso- and macropores between the MFI regimes.[53]

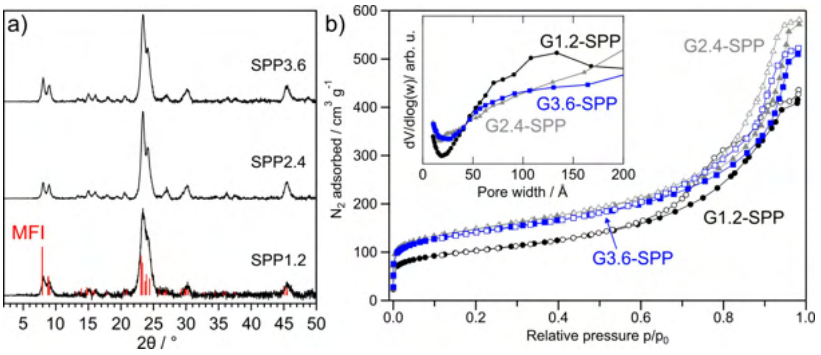

Figure 4.35: XRD diffractograms of Ga-SPP (a) with MFI as reference [143]. Nitrogen physisorption isotherms (b) and pore size distribution shown in the inset.

The acid site densities, as determined by NH_3-TPD (not shown), are remarkably low and range from 0.001 $mmol\,g^{-1}$ for SPP1.2 to 0.007 $mmol\,g^{-1}$ for SPP3.6, despite the latter's moderately high gallium content. This indicates that the gallium is likely located on the external surface in the meso- and macropores, present as non-acidic extra-framework species. TEM and HAADF-STEM did not detect any nanoparticles but due to the combination of a relatively low gallium content, limited number of imaged particles, and a limited image resolution and focus, the presence of gallium-based nanoparticles is not excluded.

As a result of the low acid site density, Ga-SPP were nearly inactive for the conversion of dmf at 500 °C, with up to 0.03 $mmol\,g^{-1}$ benzene produced over SPP3.6. This demonstrates that besides microporous MFI regions and a secondary pore network, dmf is not converted without the presence of acid sites, confirming earlier results from Si-MFI/G0.

Take-home message

Microporous Ga-containing catalysts with a secondary pore network comprising meso- and macropores have been synthesised through three different methods. The importance of the microporous structure and the acid site density has been highlighted. Meso- and macropores promote the formation of aromatics only when both these properties are preserved, illustrating the delicate balance among catalytic descriptors required to design the ideal catalyst.

4.5 The impact of reaction parameters

This section describes the influence of the reaction parameters, such as the temperature or the influence of NH_3 on the catalyst during NH_3-TPD. Additionally, it describes the effect of cofeeding other reagents besides dmf and of agitating the agitating the reaction mixture during crystallisation of Ga-MFI.

4.5.1 Effect of the temperature

The effect of the temperature has been investigated by exposing selected Ga-MFI_{micro} zeotypes to 400, 500, and 600 °C, and the conversion and selectivities towards benzene and 2,4-dmf are shown in figure 4.36.[54] *Para*-xylene was not detected and toluene only in small quantities with selectivities up to 10 %.[55]

For all three catalysts, the conversion (grey) increases when increasing the temperature from 400 °C (dots), to 500 °C (squares), and 600 °C (triangles).The main product is 2,4-dmf over G0.5 and over G1.2 at 400 °C or benzene over G1.2 at 600 °C and over G3.1. An increase in temperature, as well as an increase in gallium content, shift the selectivity from 2,4-dmf to benzene, supporting previous findings (section 4.3.3).

The increased production of benzene can be explained twofold:

1. Benzene is thermodynamically stable and often emerges as one of the main products during thermal pyrolysis without the use of a catalyst [164].
2. Coke is less stable at high temperatures in the presence of H_2O and oxygen,[56] supported by the lower quantity of coke detected during regeneration (not shown).

54: to minimize structural damage, the lowest temperature is investigated first. Ideally, a fresh catalyst would have been used for each temperature.

55: Potential thermal expansion of the pores at 600 °C did not result in additional production of toluene, although this may be expected as larger pore size frameworks, such as FAU and MOR, do favour toluene over benzene.

56: formed in the reaction by dehydration reactions while oxygen originates from the reactant dmf.

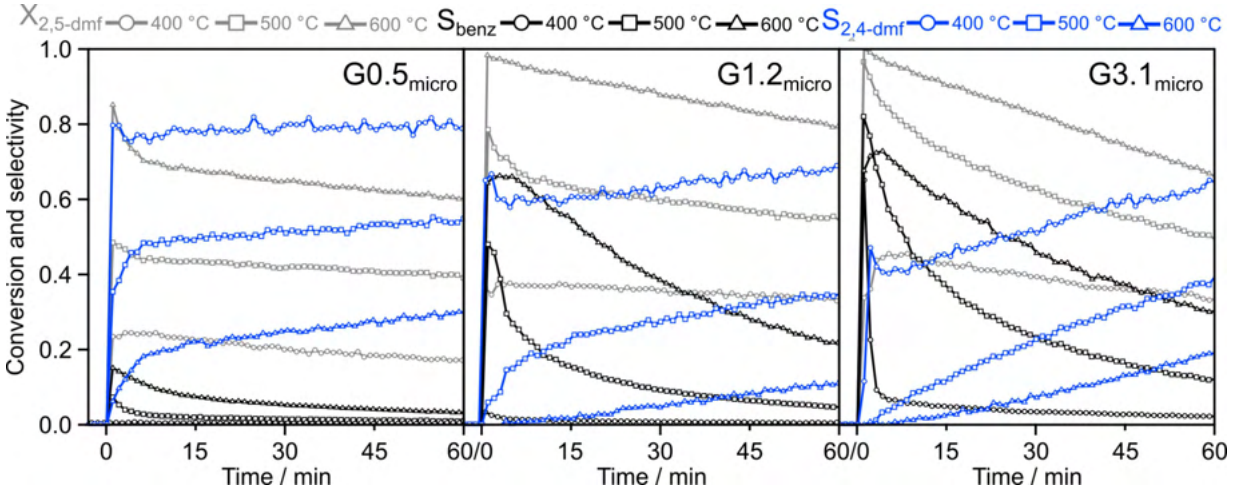

Figure 4.36: Conversion of dmf (grey) and selectivities to benzene (black) and 2,4-dmf (blue) over G0.5, G1.2, and G3.1. Reaction was run for 1 h at 400 °C (dots), 500 °C (squares), and 600 °C (triangles), separated by regeneration in 20 % O_2 at 625 °C for 1 h.

Even though the production of aromatics can be increased by increasing the temperature, the goal of this work is to design the ideal catalyst, with the inherent connected goal to lower the required energetic costs. As biomass can also be converted into aromatics thermally, catalysts are employed to maximise the conversion at lower temperatures, like 500 °C. Operating at lower temperatures also limits the structural damage to the catalyst, such as the migration of active gallium species, which may be promoted in a reactive wet environment at 600 °C.

Valorisation of dmf is not only limited to monocyclic aromatics, but may be extended to other compounds like 2,4-dmf, a valuable compound due to its rare disubstitution pattern and applications in the synthesis of stereoselective organics [165, 166]. Therefore, the synthesis of 2,4-dmf via the isomerisation of dmf has been investigated further using Ga-MFI catalysts, described in detail in paper IV [167].

To further optimise and explore the production of 2,4-dmf, Ga-MFI(33) (section 4.2.1) has been tested at different temperatures (figures 4.37, 1 and S4, paper IV). Similar to the behaviour of the other Ga-MFI catalysts, at temperatures ≥ 450 °C, aromatics and olefins are the main products at the start of the reaction which shifts to 2,4-dmf after coking of the strong acid sites. In contrast, when operating at ≤ 375 °C, 2,4-dmf is the main product from the start of the reaction, being formed at stable selectivities of 60 and 70 % at 375 and 350 °C, respectively. At 300 °C, the conversion reaches 0 % after 1 h TOS, resulting in a low SNR and hence, the product selectivities have been omitted after 1 h TOS. The catalyst was stable for 3 more cycles at 350 °C, separated by regeneration in oxygen at elevated temperatures (figure 2, paper IV).

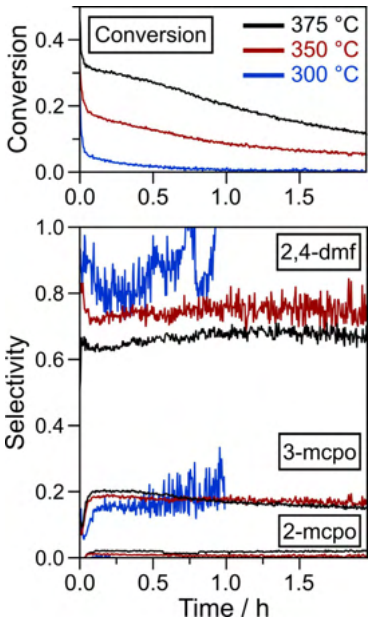

Figure 4.37: Conversion of dmf and selectivities towards 2,4-dmf, 3-mcpo, and 2-mcpo over Ga-MFI(33) at 375 °C (black), 350 °C (red), and 300 °C (blue). Curves for 300 °C are smoothed (binomial, bounce, factor 20) and data is omitted after 1 h TOS due to low SNR.

To understand the mechanism of the isomerisation of dmf into 2,4-dmf, below is a summary of the findings that have been observed throughout this thesis:

- Non-acidic G0 (Si-MFI) does not catalyse the isomerisation, indicating that acid sites are required.
- Acidic Ga_2O_3 and Ga-MCM-41 do not catalyse the isomerisation, indicating that a microporous framework is required.
- Acidic Al-MFI (Si/Al=11 and 41) also produces 2,4-dmf after an initial deactivation of the strong acid sites for the production of aromatics, indicating that gallium-based acid sites are not required.
- LTA, FER, BEA, FAU, and MOR framework zeolites produce less 2,4-dmf than MFI framework zeolites, favouring the production of 2-mcpo and 3-mcpo instead, indicating that specifically the MFI framework promotes the reaction.

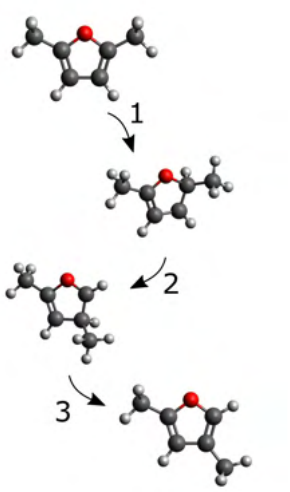

Figure 4.38: Mechanism for the isomerisation of dmf to 2,4-dmf in Ga-MFI zeolite, including proton transfer (step 1), methyl migration (step 2), and a final proton back transfer (step 3). Determined with DFT and transition states are shown in figure 3, paper IV.

Based on these points, it is suggested that the isomerisation of dmf into 2,4-dmf occurs through an acid-catalysed methyl-migration, which is promoted by steric confinement in the MFI structure [84]. The reaction landscape has been calculated with density functional theory (DFT) calculations and an overview of the elementary reaction steps is shown in figure 4.38. First, after adsorption of dmf on Ga- or Al-MFI, proton transfer of the zeolite BAS to one of the carbons next to oxygen occurs, changing the carbon's sp^2 hybridisation to sp^3. Subsequent transfer of the methyl group happens after which the proton is transferred back to the zeolite BAS, forming 2,4-dmf.

Take-home message
The catalytic conversion of dmf into aromatics occurs over a broad temperature range, peaking at 600 °C while at the the risk of structural damage. Selective isomerisation to 2,4-dmf occurs at low temperatures via a proton transfer followed by a methyl migration, catalysed by acidic Al-MFI or Ga-MFI.

4.5.2 Effect of NH_3-TPD on the catalyst

By measuring NH_3-TPD in the catalytic reactor, the evaluation of the coked and regenerated catalyst is facilitated and the acidity of the catalysts can easily be monitored between and after different cycles to test the stability. However, exposure to non-inert gases like NH_3 may affect the structure of the catalyst.[57]

To investigate the effect of the NH_3-TPD itself on the catalyst, Al-BEA(19) has been studied with and without an NH_3-TPD treatment before the reaction, as shown in figure 4.39 (a).[58] The conversion and selectivity to BTX appear rather similar, although quantification (table 4.39) reveals the positive promoting effect of the NH_3-TPD pretreatment, resulting in an increase in the production of benzene from 0.19 to 0.24 mmol g^{-1} and in the production of toluene from 0.14 to 0.20 mmol g^{-1}.

The NH_3-TPD profiles (figure 4.39, b) reveal that both the fresh catalyst (exp.1, black) and the regenerated catalyst (exp.1, purple), contain more extra-strong acid sites around 500 °C than the regenerated catalyst without an initial NH_3-TPD (blue and green). These acid sites are likely generated during the initial NH_3-TPD, after which they participate in the reaction, become coked (black, dots), and are regenerated again. Possibly, the commercially obtained Al-BEA(19) possesses extra-framework aluminium-oxides that can be reduced by ammonia, resulting in highly mobile Al^+ and AlH_2^+

57: e.g., liquid ammonia solutions have been used to create silanol defect-sites in MFI zeolites to improve metal dispersion [168, 169] and to form mobile metal complexes, like $Cu(NH_3)_4$ in zeolite FAU [170].

58: a new fraction of catalyst has been used for each experiment of the same mass (73.8 vs. 74.0 mg).

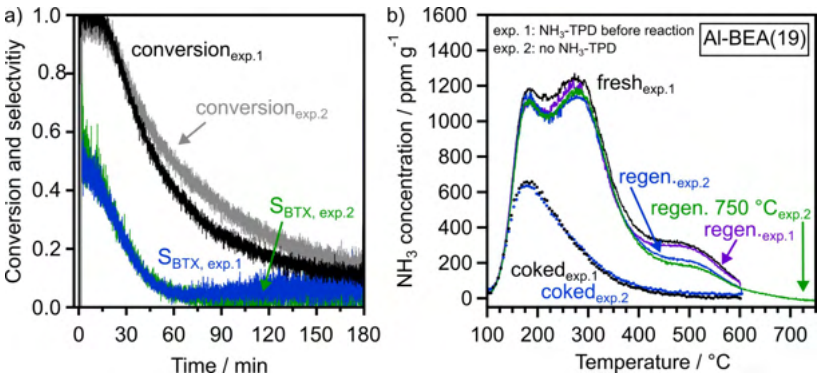

Figure 4.39: Conversion of dmf and selectivity to BTX (a) over Al-BEA(19) with an NH_3-TPD before the reaction (exp.1, black, blue) and without (exp.2, grey, green). The NH_3-TPD profiles (b) of Al-BEA(19) in its fresh state (black), coked state (black, dots), regenerated after the reaction (purple). The catalyst without an initial NH_3-TPD is measured in the coked state (blue, dots), regenerated (blue), and regenerated till 750 °C (green).

Table 4.15: Acid site densities and catalytic performance of Al-BEA(19) with and without an NH_3-TPD before the reaction.

Al-BEA(19)	$Acid_f$[a]	$Acid_c$[a]	$Acid_r$[a]	Benz.[b]	Tol.[b]	Ind.[b]	S_{coke}
	mmol g^{-1}						%
w/o NH_3-TPD[c]	N.A.	0.106	0.342	0.19	0.14	0.11	35
with NH_3-TPD	0.388	0.112	0.361	0.24	0.20	0.11	32

[a] Acid site density of the fresh (f), coked (c), and regenerated (r) catalyst, determined by NH_3-TPD
[b] Total production of benzene, toluene, indene in 3 h TOS at 500 °C
[c] without NH_3-TPD before the reaction

species. These species can migrate through the sample, bind to defect sites or become framework-associated acid sites. In another work, this improvement in metal dispersion was observed when exposing gallium-impregnated Al-MFI to H_2 at elevated temperatures, which will be explored in the next subchapter 4.5.3 [44, 171–173].

Simultaneously, the extra-strong sites of the catalyst that was not exposed to an initial NH_3-TPD (w/o NH_3-TPD), also become coked during reaction (exp.2, blue, dots) and are subsequently regenerated to a state with fewer acid sites (exp.2, blue, 0.342 vs.0.361 mmol g^{-1}). This indicates that performing the NH_3-TPD after the reaction or after regeneration did not have the same effect as it had on the fresh catalyst. Perhaps dmf itself or oxygen from the regeneration step results in the protection of the acid sites or aluminium, either due to shielding, coking, or immobilization of extra-framework species. Although the effect of the NH_3-TPD enhances the catalytic performance for Al-BEA(19), it is unknown if it affects each catalyst to the same extent. Additionally, when performing multiple cycles of reaction, NH_3-TPD is typically only performed before cycle 1 and cycle 2, introducing an error in the other cycles. An analogy can be drawn to Schrödinger's cat, with some conceptual liberty: by actively measuring the acid sites in our catalysts, they are inevitably altered, making it impossible to observe their unmodified state.

To exclude the presence of even stronger acid sites, ammonia TPD was performed a second time after regeneration of experiment 2, up to 750 °C instead of 600 °C (green). The determined acid

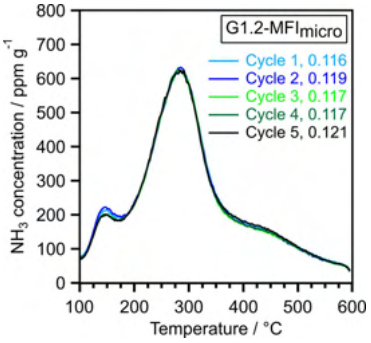

Figure 4.40: NH_3-TPD profiles of 5 consecutive cycles on $G1.2_{micro}$, with the numbers denoting the determined acid site density for each cycle (in mmol g^{-1}).

site density of 0.336 mmol g^{-1} is slightly less than 0.342 mmol g^{-1}, which means that all NH_3 had already desorbed at 600 °C by allowing the catalyst to dwell for 10 minutes. The reduction in acid site density may also indicate a degrading effect of the high temperature of the NH_3-TPD, next to the effect that NH_3 may have. This was further examined by exposing G1.2 to 5 NH_3-TPD cycles in a row, shown in figure 4.40. Quantifying the acid site densities resulted in an average of 0.118 ± 0.003 mmol g^{-1}, with a slight decrease visible after cycle 2 of the weak acid site desorbing at 150 °C. However, the narrow spread in acid site density indicates a minimal effect of the NH_3-TPD cycle on G1.2, although the effect on conversion of dmf was not evaluated.The heating ramp was investigated by testing 5 °C/min, 10 °C/min, and 20 °C/min on G0.5, after which 10 °C/min was selected.[59]

59: At 5 °C/min, broad peaks were formed and readsorption of desorbed ammonia to other sites seemed to occur. At 20 °C/min, sharp peaks were formed and peak identification was more challenging and less consistent.

Take-home message
Performing an NH_3-TPD before the reaction induces structural changes in the catalyst, increasing the number of extra-strong acid sites, which results in an increase in the production of aromatics over Al-BEA(19).

4.5.3 Effect of cofeeding of reactants

In line with the discovered effect of NH_3, the effect of intentionally reducing and reoxidising the catalyst by exposing it to a hydrogen atmosphere followed by an oxygen atmosphere, is investigated in this section. Here, G8.6-b (MFI), a new catalyst, is prepared according to the same procedure as G8.6, with some alterations.[60]

As a baseline measurement, NH_3-TPD was measured on the fresh catalyst (figure 4.41, a, black), after which dmf was converted into primarily benzene (b, grey, ca. 720 ppm dmf in Ar, 500 °C, 3 h). The coked catalysts was regenerated and NH_3-TPD reveals that some strong and extra-strong acid sites were lost around 300 °C and 550 °C (purple, 0.408 vs. 0.387 mmol g^{-1}). This is followed by a hydrogen/oxidation cycle consisting of 5 h pretreatment (PT) in 3.5 % hydrogen at 550 °C followed by re-oxidation in 30 % O_2 for 1 h at 150 °C [44]. As a result, some strong acid sites (grey, 300 °C) were transformed into extra-strong acid sites (> 500 °C), likely present as framework-associated species. After another reduction-oxidation cycle,[61] the conversion to benzene (grey) was slightly improved from 1.51 to 1.77 mmol g^{-1}. This demonstrates that the reduction-oxidation cycle improves the catalytic performance of a catalyst, especially since a diminished performance is typically observed in consecutive reaction cycles.[62]

60: the H_2O and EtOH that evaporated during hydrolysis and condensation of the silica source were refilled with H_2O and the potassium contamination of the Teflon vessel had been removed.

62: as was observed when exposing Ga-MFI_{micro} (figure S12, paper II) and Ga-MFI_{meso} (figure S9, paper III) to multiple cycles.

61: to assure that any observed effects are caused by the hydrogen PT instead of the NH_3-TPD.

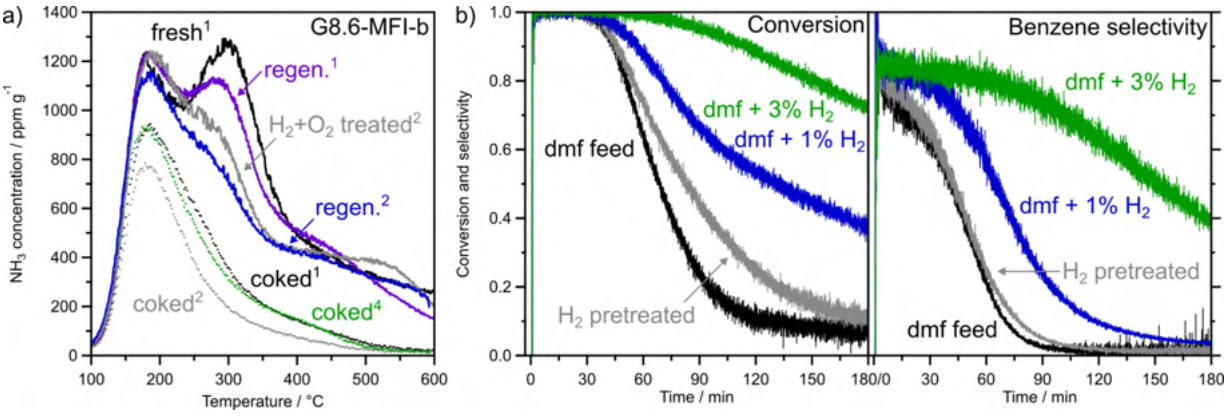

Figure 4.41: NH_3-TPD profiles (a) of G8.6-b in its fresh state (black), after reaction cycle 1 (black, dots), after regeneration (purple), after reduction-oxidation cycle (grey), after reaction cycle 2 in coked state (grey, dots), after regeneration (blue). This is followed by reaction with cofeeding 1 % H_2, another regeneration, then a reaction while cofeeding 3 % H_2, then NH_3-TPD in coked state (green, dots). Conversion and selectivity to benzene (b) are shown for dmf feed (cycle 1, black), dmf feed after H_2 pretreatment (cycle 2, grey), dmf feed while cofeeding 1 % H_2 (cycle 3, blue), and dmf feed while cofeeding 3 % H_2 (cycle 4). Reactions were performed at 500 °C with a constant total flow of 300 ml/min. Cycles were run in series on the same catalyst with regeneration cycles 20 % O_2 in between.

Besides changing the catalyst in the flow-reactor, the catalytic reaction can also be influenced by changing the feed. Here, the effect of cofeeding hydrogen, ethene, and propene was explored for Ga-MFI catalysts. After the 2nd cycle of reaction, NH_3-TPD (a, blue) reveals that most of the extra-strong acid sites at 525 °C, induced by the hydrogen/oxygen pretreatment, were lost again. Cofeeding 1 % hydrogen (b, blue) significantly improves the conversion and selectivity to benzene, producing 3.04 mmol g^{-1} benzene after 3 h TOS, compared to 1.51 mmol g^{-1} on the fresh catalyst. The selectivity to coke is reduced by cofeeding hydrogen, likely due to the hydrogenation of pre-coke species, reducing the amount of hydrogen-deficient polycyclic aromatics. which is likely related to its improved production of benzene. Cofeeding with 3% hydrogen increases the total benzene production even further to 6.38 mmol g^{-1}. Further ex-situ analysis of the coked catalyst with pyridine DRIFTS and TGA/DSC [83], or by extraction with HF [174], can help identify the remaining coke species and investigate the exact role of hydrogen.

In other works, the conversion of furanics into aromatics is proposed to occur through a Diels-Alder cycloaddition dehydration reaction by cofeeding a diene such as ethene [27, 44, 100, 175–177]. An increase in the formation of xylene was observed as the introduction of ethene offered additional carbon needed to convert dmf, with 6 carbon atoms, to xylenes with 8. To test this protocol and drive the selectivity towards xylene, ethene has been co-fed over Ga-MFI(33) at 300, 400, and 500 °C, partially described in paper I [84]. At 300 and 400 °C, no apparent effect of the cofeeding of ethene was observed, while at 500 °C, the formation of benzene and toluene production is increased. Cofeeding propene instead

Table 4.16: Acid site densities and catalytic performance of G8.6-b while cofeeding reactants.

Feed	$Acid_f$[a]	$Acid_c$[a]	Benz.[b]	Tol.[b]	Ind.[b]	Nap.[b]	2,4-dmf[b]	S_{coke}
	mmol g^{-1}							%
dmf	0.408	0.158	1.51	0.13	0.15	0.05	0.61	15.5
dmf H_2 PT[c]	0.351	0.110	1.77	0.12	0.19	0.04	0.61	13.1
dmf+1% H_2	0.333	N.A.[d]	3.04	0.11	0.30	0.04	1.01	8.9
dmf+3% H_2	N.A.[d]	0.161	6.38	0.17	0.48	0.06	0.13	4.9

[a] Acid site density of the fresh (f) and coked (c) catalyst, determined by NH_3-TPD
[b] Total production of benzene, toluene, indene, naphthalene, and 2,4-dmf in 3 h TOS at 500 °C
[c] Pretreated: After two reduction-oxidation pretreatments
[d] N.A.=Not available since this was not measured

of ethene, at 500 °C, results in a similar increase in the production of ethene, 1,3-butadiene, and toluene, illustrating both its fragmentation and the build-up of hydrocarbons in the hydrocarbon pool.

Take-home message
By cofeeding hydrogen to the reaction, the formation of coke is significantly reduced, resulting in an increase in the lifetime of the catalyst and associated production of benzene. Cofeeding of ethene or propene resulted in an increase in the production of benzene and toluene but not *para*-xylene, indicating that the reaction occurs through a hydrocarbon-pool-based mechanism instead of a Diels-Alder-reduction-dehydration mechanism.

4.5.4 Effect of the synthesis conditions: agitated crystallisation

As shown in section 4.3, Ga-MFI based catalysts comprise many different crystals that are heterogeneous in size, shape, and composition. A possible explanation may be the presence of local concentration differences during the synthesis of the material, in particular during the crystallisation step in a static oven. Therefore, G8.6-c has been synthesised both in a static oven (SO) and a rotating oven (RO) (5 days at 170 °C, 45 rpm).[63]

The morphology of the catalysts is studied with SEM (figure 4.42). The crystallites of G8.6-c-RO are spheres of 1 µm in diameter, each comprising long coffin-shaped needles.[64] On the other hand, crystals of G8.6-c-SO comprise different shapes and sizes, including spheres made up of needles and larger intergrowths of the coffin-shaped crystals, each spanning roughly 2 microns. This confirms that the crystal size and shape homogeneities can be improved by

63: The difference with G8.6-b is in the order of addition: G8.6-b is hydrolysed for 24 h under acidic conditions, after which TPAOH and NaOH were added, similar to G8.6. By contrast, TPAOH was added to G8.6-MFI-c before hydrolysis and NaOH after 24 h of hydrolysis.

64: similar to what was seen for G6.7, G8.6, and G11

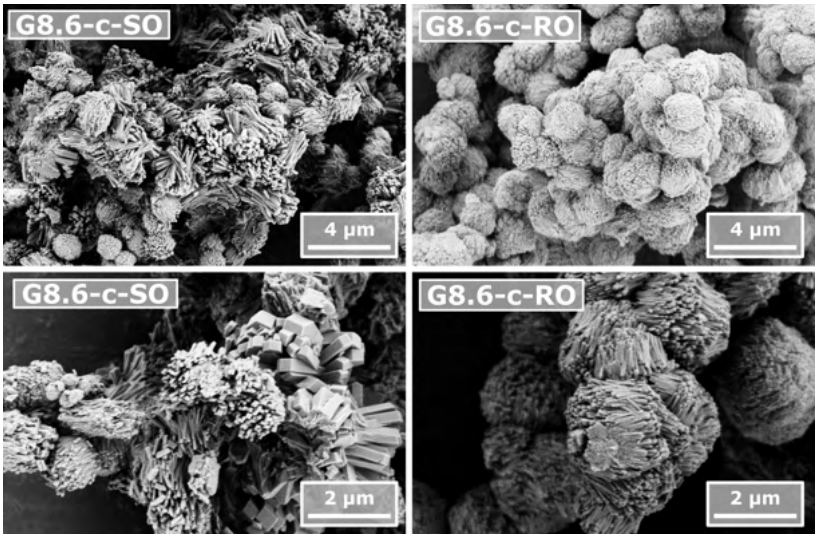

Figure 4.42: SEM images of G8.6-c prepared in a static (SO) and rotating oven (RO).

agitating the reaction mixture during crystallisation, e.g., through using a rotating oven.

The porosity is investigated by nitrogen physisorption, shown in figure 4.43 and quantified in table 4.17. The isotherms differ in the size of the hysteresis loop, which is slightly larger for G8.6-c-RO (blue), indicating a larger mesoporous volume between crystal aggregates. This is confirmed by the lower SA, lower V_{mic}, and higher S_{ext}. The mesopores are likely located between the small needle-shaped crystallites that make up the larger, spherical particles or intergrowths which were seen with SEM. These crystallites are observed in both catalysts, which is why PSD shows that the diameter of the mesopores is equal. However, G8.6-c-SO contains fewer of the smaller crystallites and instead larger crystals, which have fewer boundaries with other crystallites and thus logically, fewer intercrystalline mesopores.

The NH_3-TPD profiles (not shown) and acid site densities of the two catalysts are relatively similar, with 0.485 and 0.478 mmol g^{-1} for fresh G8.6-c-SO and G8.6-c-RO, respectively. The conversion of dmf was tested (figure 4.44) and G8.6-c-RO produces more benzene than G8.6-c-SO (1.73 vs. 1.56 mmol g^{-1}, table 4.17), even though its acid site density is slightly lower. This indicates that the homogeneous crystals are beneficial for the reaction, possibly caused by the smaller average size of the spherical crystals, reducing the diffusion pathways of reagents and products.[65] To verify that the homogeneity of the crystals also corresponds to a homogeneity of their compositions, further EDX analysis must be performed.

Comparing G8.6-c-SO to G8.6-b (also synthesised in a static oven), shows that the former possesses more acid sites 80.485 vs. 0.408 mmol g^{-1}) and produces slightly more benzene (1.56 vs. 1.51 mmol g^{-1}). Although more systematic studies are required to determine the optimal synthesis conditions, it may be noted

65: as was observed for G6.7

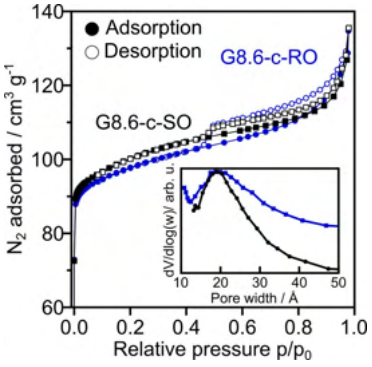

Figure 4.43: physisorption isotherms of G8.6-c-SO (black, squares) and G8.6-c-RO (blue, dots). Pore size distribution of the mesopores is shown in the inset, as derived by applying the BJH-model to the adsorption curve.

that pre-zeolitic silica/gallium network of G8.6-c-SO is formed under basic conditions (pH 10–11), vs. acidic conditions used to synthesise G8.6-b (pH 0–1). The high gallium content of 8.6wt.% results in a high concentration of acidic gallium precursor, which may be compensated by TPAOH (G8.6-c), resulting in a pH in which both hydrolysis and condensation occurs gradually, forming a cross-linked silica network that is more uniform, homogeneous, and free of defects. If instead hydrolysis occurs in acidic conditions, the rate of condensation is much lower, resulting in a sudden rapid condensation once TPAOH and NaOH are both added. Consequently, the pre-zeolitic network of G8.6-b may be more clustered, heterogeneous, and more defective.

Table 4.17: Overview of the physicochemical properties and catalytic performance of G8.6-c synthesised in a static oven (SO) or rotating oven (RO).

Sample	SA[a]	S_{ext}[b]	V_{mic}[b]	$Acid_f$[c]	$Acid_c$[c]	$Acid_r$[c]
	$m^2\,g^{-1}$		$cm^3\,g^{-1}$	$mmol\,g^{-1}$		
SO	395	29	0.145	0.485	0.178	0.458
RO	388	34	0.138	0.478	0.177	0.464
	Benz.[d]	Tol.[d]	Ind.[d]	Nap.[d]	2,4-dmf[d]	S_{coke}
	$mmol\,g^{-1}$					wt.%
SO	1.56	0.12	0.16	0.02	0.52	20.7
RO	1.73	0.12	0.14	0.03	0.41	21.5

[a] Apparent surface areas by BET method, p/p_0 = 0.005–0.025 following consistency criteria [112]
[b] By t-plot method [116] (Harkins and Jura equation, t= 5.0–8.0 Å)
[c] Acid site density of the fresh (f), coked (c), and regenerated (r) catalysts, determined by NH_3-TPD
[d] Total production of benzene, toluene, indene, naphthalene, and 2,4-dmf in 3 h TOS at 500 °C

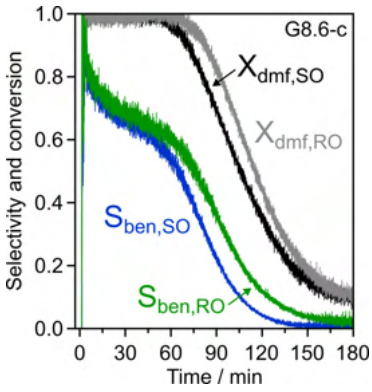

Figure 4.44: Conversion of dmf of G8.6-c-SO (black) and G8.6-c-RO (grey), as well as the selectivity to benzene of G8.6-c-SO (blue) and G8.6-c-RO (green).

4.6 Mechanistic insights

Based on the findings obtained throughout this thesis, the following mechanistic insights have been derived, summarised in figure 4.45. While most of the products have been detected experimentally, the carbocations are postulated to be intermediary products. Promoting factors are indicated along the reaction arrows, such as a particular framework, strong and weak Brønsted acid sites (sBAS/wBAS), and strong and weak Lewis acid sites (sLAS/wLAS).[66] The findings are based on the observed product distributions, the relationships between the descriptors of the catalysts and their catalytic performance, and largely on acid site analyses performed with pyridine DRIFTS. As pyridine DRIFTS has only been conducted on Ga-MFI$_{micro}$ and Ga-MFI$_{meso}$ catalysts, the mechanistic insights may be slightly different for Al-containing catalysts.

66: if there is only limited evidence, the term is greyed out

First, 2,5-dimethylfuran either binds to a BAS or a LAS. As the exact identities of the different LAS species is unknown, this pathway is not explored or interpreted further. When binding to either a strong or weak BAS, dmf is protonated and one of the double bonds is saturated. The shown intermediate is more likely to form than *O*-H$^+$-dmf [167], and through a subsequent rotation, methyl shift, and deprotonation, isomerisation to 2,4-dmf occurs. This reaction is promoted by wBAS, pore confinement by the MFI framework, a low metal content, and low temperatures of $< 400\,^{\circ}C$. A low metal content is often associated with a high fraction of weak sites so these factors are connected; sBAS may potentially promote this reaction but it highly favours aromatisation reactions instead.

The protonated dmf (carbocation) can undergo ring-opening and subsequent cracking, decarbonylation, and dehydration to form the constituents of the hydrocarbon pool, processes that are all promoted by sBAS. Through demethylation, 2-methylfuran is formed which is generally detected after the sBAS of the catalyst have deactivated, suggesting that 2-mf is broken down into hydrocarbons in the presence of sBAS. The hydrocarbons, such as methane, ethene, propene, and 1,3-butadiene, are aromatised by both sBAS and sLAS into the monocyclic aromatics benzene and toluene; xylenes are hardly formed (greyed out). While benzene is the favoured product over medium-pore MFI and disordered large-pore BEA, toluene is the favoured product over large-pore frameworks MOR and FAU, as well as over external surface acid sites when the access to micropores is blocked. The production of aromatics can be enhanced by cofeeding ethene or propene at temperatures $> 500\,^{\circ}C$, at which they constitute to the hydrocarbon pool.[67] No increase of *para*-xylene was observed when cofeeding

67: cofeeding ethene was found to have a negligible effect at $400\,^{\circ}C$ [84].

ethene, suggesting that the Diels-Alder cycloaddition dehydration reaction does not occur on the tested Ga-MFI [45].

Additionally, further aromatisation of hydrocarbon pool constituents and BTX into polycyclic aromatics results in the formation of coke precursors indene and naphthalene and ultimately, coke in the form of e.g., PAHs. This reaction is catalysed by sBAS and potentially also by the other types of acid sites, as evidenced by their reduction in abundance due to the formation of coke.

When this preferred mechanistic route is impeded by coke, isomerisation reactions dominate including the formation of 2,4-dmf as well as the formation of 2-mcpo and 3-mcpo. If the intermediary product is not broken down by sBAS, it can undergo ring-closure, followed by a methyl shift and deprotonation to form 2-mcpo and 3-mcpo. The production of 3-mcpo was favoured by Al-BEA and Al-MFI over 2-mcpo, while the latter was favoured over Ga-BEA and Ga-MFI (by wLAS), suggesting a metal-specific effect. The methyl shift and deprotonation may also result in the formation of 4-mcpo, which is not part of the reference library and cannot be detected. Moreover, 3-mcpo was formed at an earlier stage than 2-mcpo for both Al- and Ga-catalysts, hinting that it may be an intermediate for 2-mcpo. Further mechanistic insights can be obtained by cofeeding different reactants, like water and methanol, or by using different feedstocks, such as 2-mf, 2,4-dmf, 2-mcpo, and 3-mcpo.

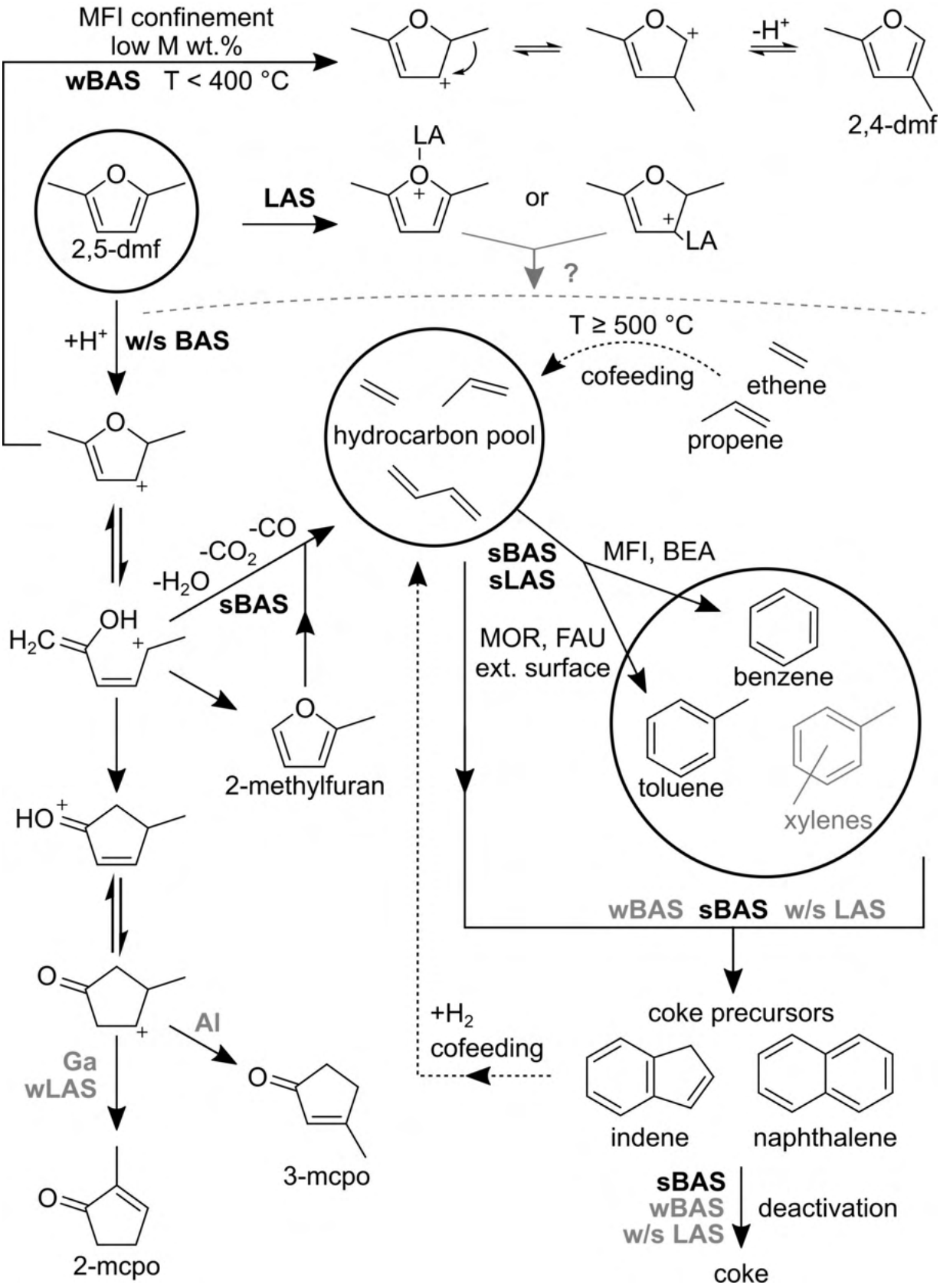

Figure 4.45: Proposed mechanism for the catalytic valorisation of 2,5-dimethylfuran into aromatics, based on the findings from this thesis. Full arrows indicate proposed reaction pathways, dashed arrows the cofeeding of reactants, notations indicate promoting factors such as specific acid sites or structures, which are marked grey if there is limited evidence.

Conclusions and future work 5

5.1 Conclusions

This thesis set out to understand the relationship between the properties of the catalyst and its catalytic performance in the conversion of 2,5-dimethylfuran (dmf) into aromatics. Guided by five research questions, this aim was explored by systematically investigating the role of the framework, acidity, and porosity, on the activity and selectivity of the catalyst.

Firstly, the selection of the microporous framework was investigated by studying a series of Al-containing zeolite frameworks. It was demonstrated that dmf is converted over a variety of frameworks, with MFI exhibiting the highest conversion and selectivity, followed by BEA and FAU. This section highlights the positive effect of a framework with micropores slightly larger than the reactants and desired products, steering the selectivity towards monocyclic aromatics instead of coke.

Secondly, the influence of the substituted heteroatom was investigated by comparing Al- and Ga-substituted MFI and BEA catalysts. Ga-containing catalysts demonstrate/exhibit a higher conversion and selectivity to aromatics, primarily benzene, owing to their higher quantity of extra-strong Lewis acid sites. Bifunctional extra-framework gallium, both reducing the pore size and interacting synergistically with framework Ga, is considered to be the origin of the promoting effect.

Thirdly, the effect of varying the amount of aluminium and gallium in MFI, BEA, and FAU framework catalysts was investigated. It is demonstrated that an increase in content corresponds to an increase in acid site density, improving the activity towards the formation of monocyclic aromatics. However, an excessive content of $\geq$3.5 wt.% Al in MFI, $\geq$12 wt.% Al in FAU, or $\geq$11 wt.% Ga in MFI, resulted in rapid coke-related deactivation, partially caused by the formation of Ga-nanoparticles in Ga-MFI. This highlights the importance of balancing the heteroatom content and acidity with the stability and activity of the catalyst.

Fourthly, the role of a secondary pore network consisting of meso- and macropores was investigated by studying Ga-containing MFI_{meso}, MCM-41, MFI/MCM-41, and SPP. Introducing meso- and macropores in Ga-MFI_{meso} improved mass transport while halving the acid site density, ultimately improving the activity per acid site. A further increase in pore size resulted in the promotion of coke

over monocyclic aromatics, as observed in mesoporous Ga-MCM-41 and to a lower degree in micro-/mesoporous Ga-MFI/MCM-41 composites. These findings reveal the potential of introducing a secondary pore network, provided that both the microporosity and high acid site density of the catalyst is preserved.

By combining the answers to the guiding research questions, mechanistic insights into the conversion of dmf into aromatics have been obtained. Initially, an acid-catalysed ring-opening is followed by decomposition into olefins and other constituents of the hydrocarbon pool, promoted by strong Brønsted acid sites. Strong BAS and LAS then catalyse aromatisation into BTX, which is also promoted by cofeeding olefins and through pore confinement by extra-framework Ga. Subsequent acid-catalysed aromatisation results in the formation of coke, eventually leading to deactivation of the catalyst, which can be significantly delayed by cofeeding hydrogen.

In conclusion, this thesis has identified the relevant design principles of catalysts for the conversion of dmf into aromatics. An ideal catalyst possesses a balance between a microporous framework to steer selectivity towards BTX, a high and controlled metal content and acid site density to maximise activity, and a hierarchical porosity to improve mass transport. In a broader context, these findings answer the question that was presented in the introduction: *can BTX chemicals be synthesized from renewable feedstocks?* By identifying and evaluating the key descriptors that dominate the activity, selectivity, and stability of the catalyst, this work aids future catalyst design for the production of commodity chemicals from biomass-derived furans. Ultimately, this thesis contributes to the broader goal of transitioning into a renewable, circular, fossil-free chemical industry.

5.2 Future directions

The future directions of this work can be separated into three different areas:

Firstly, the synthesized materials can be analysed to a greater extent, strengthening suggested explanations, improving upon the employed techniques, and possibly revealing new catalytic descriptors and trends. For example, the reliability of the determined textural properties may be improved by using argon physisorption at 87 K and the mesoporous structures can be explored with small-angle X-ray scattering (SAXS) [161]. Gallium-induced unit cell expansion may be detected with single-crystal XRD[1] or Rietveld refinement of powder XRD. Moreover, the distribution of framework and extra-framework gallium may be resolved with solid-state nuclear magnetic resonance spectroscopy (ssNMR) of silicon and gallium.[2] X-ray absorption spectroscopy (XAS) could elucidate the identity of the gallium species by examining their local structural environment and coordination geometry.[3] Similarly, X-ray photoelectron spectroscopy (XPS) can provide insights into the oxidation state and identity of surface gallium.[4]

Secondly, the design and synthesis of suitable catalysts for the conversion of dmf into aromatics can be continued, applying all the insights obtained throughout this work. For example, the synthesis Ga-MFI/MCM-41 catalysts with a high gallium content may be realised by adding a base after the initial formation of Ga-MCM-41, aiding its partial transformation into MFI. Additionally, the introduction of meso- and macropores into Ga-MFI_{micro} may be performed in milder conditions, such as shorter reaction times, to prevent the loss of half of its acid sites.

Thirdly, different reactions may be investigated that employ different feedstocks, like the model compounds furan and 2-methylfuran. Due to the increased pore confinement by extra-framework gallium, the smaller reagents may experience increased mass transport, conversion, and selectivity towards BTX. The mechanism may be elucidated by using side-products such as 2,4-dmf, 2-mcpo, or 3-mcpo, as feedstock. Additionally, the implications of this study may be tested by using raw biomass as feedstock, directly exploring the production of BTX from biomass while removing the need for additional synthesis steps to manufacture model compounds.

To summarise, after investigating numerous catalysts, covering a wide variety of properties and catalytic descriptors, there is always another interesting material waiting on the nanoscopic horizon. This work paves the way for additional research into the *Catalyst Design for the Valorisation of 2,5-Dimethylfuran into Aromatics.*

1: Initial selection of single crystals of Ga-MFI_{micro} and Ga-MFI_{meso} proved difficult due to their heterogeneous agglomerations of small crystals. The MFI structure (SiO_2) was detected for G6.7, albeit without gallium)

2: Initial ^{1}H NMR of G6.0 detected water and silanol (Si-OH), while ^{71}Ga NMR MAS detected only very weak signals (low quadrupolar coupling) due to the symmetric environment of gallium-based nanoparticles and through coordination to water (ack. Aleksander Jaworski, Stockholm University).

3: Initial lab-scale ex-situ XAS (ack. Simo Huotari, University of Helsinki) did not detect differences between G3.1 and G6.0 (Ga-MFI_{meso}).

4: Initial lab-scale testing detected Ga^{3+} in both G6.7 and G11, although further speciation into GaO^{+}, Ga_2O_3, or framework Ga^{3+} remained challenging.

Bibliography

(1) M. Kampa and E. Castanas, *Environmental Pollution*, 2008, **151**, 362–367 (cit. on p. 1).

(2) W. Fulkerson, R. R. Judkins and M. K. Sanghvi, *Scientific American*, 1990, **263**, 128–135 (cit. on p. 1).

(3) C. Bauer, K. Treyer, T. Heck and S. Hirschberg, in *Encyclopedia of the Anthropocene*, 2017, vol. 1-5, pp. 473–484 (cit. on p. 1).

(4) Y. Hirabayashi et al., *Nature Climate Change*, 2013, **3**, 816–821 (cit. on p. 1).

(5) P. Stott, *Science*, 2016, **352**, 1517–1518 (cit. on p. 1).

(6) J. Spinoni, J. V. Vogt, G. Naumann, P. Barbosa and A. Dosio, *International Journal of Climatology*, 2018, **38**, 1718–1736 (cit. on p. 1).

(7) International Energy Agency (IEA), *World Energy Balances 2022 Edition - Database Documentation*, tech. rep., 2022 (cit. on p. 1).

(8) I. Dincer, *Renewable & Sustainable Energy Reviews*, 2000, **4**, 157–175 (cit. on p. 1).

(9) O. Ellabban, H. Abu-Rub and F. Blaabjerg, *Renewable and Sustainable Energy Reviews*, 2014, **39**, 748–764 (cit. on p. 1).

(10) World Economic Forum, *The Speed of the Energy Transition Gradual or Rapid Change? [White paper]*, 2019 (cit. on p. 1).

(11) J. G. Speight, in *Environmental Organic Chemistry for Engineers*, Butterworth-Heinemann, 2017, pp. 43–86 (cit. on p. 1).

(12) C. M. Lok, J. Van Doorn and G. Aranda Almansa, *Renewable and Sustainable Energy Reviews*, 2019, **113**, 109248 (cit. on pp. 1, 5).

(13) J. Tickner, K. Geiser and S. Baima, *Environment*, 2021, **63**, 4–15 (cit. on p. 1).

(14) G. C. Unruh, *Energy Policy*, 2000, **28**, 817–830 (cit. on p. 1).

(15) F. Bauer and G. Fontenit, *Energy Policy*, 2021, **156**, 112418 (cit. on p. 1).

(16) International Energy Agency, *Oil 2024*, tech. rep., 2024, p. 151 (cit. on p. 1).

(17) British Petroleum, *bp Energy Outlook 2023*, tech. rep. July, 2023, pp. 1–53 (cit. on p. 1).

(18) J. Skovgaard, G. Finkill, F. Bauer, M. Åhman and T. D. Nielsen, *Global Environmental Change*, 2023, **80**, 102657 (cit. on p. 1).

(19) J. P. Tilsted, F. Bauer, C. Deere Birkbeck, J. Skovgaard and J. Rootzén, *One Earth*, 2023, **6**, 607–619 (cit. on p. 1).

(20) J. P. Tilsted and P. Newell, *Review of International Political Economy*, 2025, **32**, 1214–1238 (cit. on p. 1).

(21) M. Zanon-Zotin et al., *Nature Communications*, 2024, **15**, DOI: 10.1038/s41467-024-52434-y (cit. on p. 2).

(22) J. L. Pellegrino, *Energy and Environmental Profile of the U.S. Chemical industry*, tech. rep., 2000 (cit. on p. 5).

(23) S. Matar and L. F. Hatch, in *Chemistry of Petrochemical Processes*, 2001, pp. 262–300 (cit. on p. 5).

(24) M. Bender, New Technologies and Alternative Feedstocks in Petrochemistry and Refining, Ludwigshafen, 2013, pp. 59–65 (cit. on p. 5).

(25) T. R. Carlson, J. Jae, Y. C. Lin, G. A. Tompsett and G. W. Huber, *Journal of Catalysis*, 2010, **270**, 110–124 (cit. on p. 5).

(26) T. R. Carlson, Y. T. Cheng, J. Jae and G. W. Huber, *Energy and Environmental Science*, 2011, **4**, 145–161 (cit. on p. 5).

(27) Y. T. Cheng and G. W. Huber, *Green Chemistry*, 2012, **14**, 3114–3125 (cit. on pp. 5, 6, 69).

(28) G. W. Huber and A. Corma, *Angewandte Chemie International Edition*, 2007, **46**, 7184–7201 (cit. on p. 5).

(29) A. Corma, G. W. Huber, L. Sauvanaud and P. O'Connor, *Journal of Catalysis*, 2007, **247**, 307–327 (cit. on p. 5).

(30) G. W. Huber, P. O'Connor and A. Corma, *Applied Catalysis A: General*, 2007, **329**, 120–129 (cit. on p. 5).

(31) J. Zakzeski, P. C. Bruijnincx, A. L. Jongerius and B. M. Weckhuysen, *Chemical Reviews*, 2010, **110**, 3552–3599 (cit. on p. 5).

(32) P. N. Vennestrøm, C. M. Osmundsen, C. H. Christensen and E. Taarning, *Angewandte Chemie - International Edition*, 2011, **50**, 10502–10509 (cit. on p. 5).

(33) T. A. Werpy, J. E. Holladay and J. F. White, *Top Value Added Chemicals From Biomass: I. Results of Screening for Potential Candidates from Sugars and Synthesis Gas*, tech. rep., 2004, p. 76 (cit. on p. 5).

(34) M. Besson, P. Gallezot and C. Pinel, *Chemical Reviews*, 2013, **114**, 1827–1870 (cit. on p. 5).

(35) M. J. Climent, A. Corma and S. Iborra, *Green Chemistry*, 2013, **16**, 516–547 (cit. on p. 5).

(36) X. Zhou, W. Li, R. Mabon and L. J. Broadbelt, *Energy Technology*, 2017, **5**, 52–79 (cit. on p. 5).

(37) B. D. Solomon, J. R. Barnes and K. E. Halvorsen, *Biomass and Bioenergy*, 2007, **31**, 416–425 (cit. on p. 5).

(38) M. A. Abdel-Rahman, Y. Tashiro and K. Sonomoto, *Biotechnology Advances*, 2013, **31**, 877–902 (cit. on p. 5).

(39) A. V. Bridgwater, *Applied Catalysis A: General*, 1994, **116**, 5–47 (cit. on p. 5).

(40) D. A. Bulushev and J. R. Ross, *Catalysis Today*, 2011, **171**, 1–13 (cit. on p. 5).

(41) R. W. Thring, S. P. Katikaneni and N. N. Bakhshi, *Fuel processing technology*, 2000, **62**, 17–30 (cit. on pp. 5, 8).

(42) Y. T. Cheng and G. W. Huber, *ACS Catalysis*, 2011, **1**, 611–628 (cit. on pp. 5, 6, 18).

(43) T. Ennaert et al., *Chemical Society Reviews*, 2016, **45**, 584–611 (cit. on p. 5).

(44) E. A. Uslamin et al., *Chemical Engineering Science*, 2019, **198**, 305–316 (cit. on pp. 5, 67–69).

(45) S. Dutta and N. S. Bhat, *Biomass Conversion and Biorefinery*, 2023, **13**, 541–554 (cit. on pp. 5, 18, 74).

(46) E. A. Uslamin et al., *ACS Catalysis*, 2019, **9**, 8547–8554 (cit. on p. 6).

(47) E. T. Vogt and B. M. Weckhuysen, *Nature*, 2024, **629**, 295–306 (cit. on p. 6).